2017

Experimental Investigation Of Polymer Adhesion Mechanics Using A Blister Contact Test

Nathan Ip
University of Pennsylvania, ipnathan@seas.upenn.edu

Experimental Investigation Of Polymer Adhesion Mechanics Using A Blister Contact Test

Abstract
The adhesion of thin layers of soft polymers is important in many applications, such as tapes, microtransfer printing, and bioinspired adhesives. Traditional adhesion tests based on probe contacts are not suitable for characterizing thin layers and common separation-based specimens, such as the peel test, have well-known limitations. The blister contact test (BCT) was developed in this dissertation to overcome the limitations of current methods and was used to investigate the adhesion and separation of several technologically relevant adhesive systems. In the BCT, a thin sheet was elastically deformed into adhesive contact with a reference substrate and the contact area was optically imaged. Modulated pressure was applied to generate both advancing and receding adhesive contact. Digital image correlation was used to measure the displacements of the specimen. The strain energy release rate at the interface was determined from the measured contact radius, applied pressure, system geometry, and elastic properties of the specimen using a mechanics model. An analytical mechanics model based on von K□rm□n plate theory was developed and used for analysis of the BCT data. Finite element analysis was used to validate and identify the range of applicability of the analytical model.

The BCT was used to investigate the adhesion and separation behaviors of three different polymer adhesive systems. First, experiments between a silicone elastomer (polydimethylsiloxane – PDMS) and a stiff substrate were performed to investigate rate effects in adhesion and separation. For the first time, the rate dependence during advancing contact was characterized. Second, the effect of acid-base interactions on performance of pressure sensitive adhesives (PSAs) was examined via a series of BCTs in which adhesion between different formulations of adhesives and multiple substrates was investigated. Viscoelastic contributions to PSA adhesion were also studied. Finally, the effect of layer thickness on rate dependence was investigated through experiments between polyethylene terephthalate (PET) sheets and PDMS films of different thicknesses. The work in this dissertation demonstrates the flexibility and capability of the BCT as a method to characterize adhesion of flat polymer sheets and provides new understanding of several types of polymer adhesive contacts.

Degree Type
Dissertation

Degree Name
Doctor of Philosophy (PhD)

Graduate Group
Mechanical Engineering & Applied Mechanics

First Advisor
Kevin T. Turner

Keywords
Adhesion mechanics, Blister contact test, Mechanics of materials, Polymer adhesion, Pressure sensitive adhesives

Subject Categories
Engineering Mechanics | Mechanical Engineering

EXPERIMENTAL INVESTIGATION OF POLYMER ADHESION MECHANICS USING A BLISTER CONTACT TEST

Nathan Ip

A DISSERTATION

in

Mechanical Engineering and Applied Mechanics

Presented to the Faculties of the University of Pennsylvania

in

Partial Fulfillment of the Requirements for the

Degree of Doctor of Philosophy

2017

Supervisor of Dissertation

_____

Kevin T. Turner, Professor of Mechanical Engineering and Applied Mechanics

Graduate Group Chairperson

_____

Kevin T. Turner, Professor of Mechanical Engineering and Applied Mechanics

Dissertation Committee

John L. Bassani
Richard H. and S.L. Gabel Professor, Mechanical Engineering and Applied Mechanics

Russell J. Composto
Professor, Materials Science and Engineering

EXPERIMENTAL INVESTIGATION OF POLYMER ADHESION MECHANICS USING A BLISTER CONTACT TEST

ACKNOWLEDGMENTS

I would like to express my sincerest gratitude to Prof. Kevin Turner for his guidance throughout my PhD. In addition to teaching me mechanics of materials, he has been an excellent mentor in teaching me how to become a better researcher and provided me with the best opportunities to succeed.

There are many colleagues and friends who assisted with my work throughout my PhD. I would like to especially thank Mike, Helen, Yijie (Steven), Lisa among others who have been influential in my research. Dave Yarusso and the MEAM machine shop have also helped me tremendously in various parts of my research.

I would also like to thank my family for the support over the years – my parents who unconditionally supported my education and advised me on choosing the right path; my brother whom we shared many happy moments even though we reside on opposite sides of the world; my pets who supplied me unlimited doses of joy (and fur); and most importantly my wife who is always by my side, encourages me when I am frustrated and cheers me up when I am sad. I am forever in debt with my family and I look forward to share the next phase of my life with them.

ABSTRACT

EXPERIMENTAL INVESTIGATION OF POLYMER ADHESION MECHANICS USING A BLISTER CONTACT TEST

Nathan Ip

Kevin T. Turner

The adhesion of thin layers of soft polymers is important in many applications, such as tapes, microtransfer printing, and bioinspired adhesives. Traditional adhesion tests based on probe contacts are not suitable for characterizing thin layers and common separation-based specimens, such as the peel test, have well-known limitations. The blister contact test (BCT) was developed in this dissertation to overcome the limitations of current methods and was used to investigate the adhesion and separation of several technologically relevant adhesive systems. In the BCT, a thin sheet was elastically deformed into adhesive contact with a reference substrate and the contact area was optically imaged. Modulated pressure was applied to generate both advancing and receding adhesive contact. Digital image correlation was used to measure the displacements of the specimen. The strain energy release rate at the interface was determined from the measured contact radius, applied pressure, system geometry, and elastic properties of the specimen using a mechanics model. An analytical mechanics model based on von Kármán plate theory was

developed and used for analysis of the BCT data. Finite element analysis was used to validate and identify the range of applicability of the analytical model.

The BCT was used to investigate the adhesion and separation behaviors of three different polymer adhesive systems. First, experiments between a silicone elastomer (polydimethylsiloxane – PDMS) and a stiff substrate were performed to investigate rate effects in adhesion and separation. For the first time, the rate dependence during advancing contact was characterized. Second, the effect of acid-base interactions on performance of pressure sensitive adhesives (PSAs) was examined via a series of BCTs in which adhesion between different formulations of adhesives and multiple substrates was investigated. Viscoelastic contributions to PSA adhesion were also studied. Finally, the effect of layer thickness on rate dependence was investigated through experiments between polyethylene terephthalate (PET) sheets and PDMS films of different thicknesses. The work in this dissertation demonstrates the flexibility and capability of the BCT as a method to characterize adhesion of flat polymer sheets and provides new understanding of several types of polymer adhesive contacts.

TABLE OF CONTENTS

ACKNOWLEDGMENTS ..... **iii**

ABSTRACT ..... **iv**

TABLE OF CONTENTS ..... **vi**

LIST OF TABLES ..... **viii**

LIST OF ILLUSTRATIONS ..... **ix**

CHAPTER 1: Introduction **1**

1.1 Motivation 1

1.2 Challenges in traditional adhesion testing instruments 2

1.3 Objective 2

1.4 Scope of dissertation 3

CHAPTER 2: Literature review **7**

2.1 Fundamentals of adhesion 7

2.2 Adhesion mechanics 11

2.3 Rate-dependent adhesion 15

2.4 Adhesion testing methods 17

2.5 Bulge test and blister contact test 21

2.6 Optical measurement techniques 22

CHAPTER 3: Design and mechanics of the BCT **25**

3.1 Introduction 25

3.2 Specimen mechanics 25

3.3 Bulge test 29

3.4 Blister contact test 40

3.5 Results and discussion 43

3.6 Summary 47

CHAPTER 4: Characterization of rate-dependent adhesion of PDMS using the BCT 49

4.1 Background 49

4.2 Specimen mechanics 50

4.3 Experimental approach 56

4.4 Results and discussions 62

4.5 Summary 68

CHAPTER 5: Role of bulk viscoelasticity, friction, and repeated contact in an adhesive contact between an elastomer and stiff surface 70

5.1 Introduction 70

5.2 Experiments and methods 71

5.3 Results and discussion 77

5.4 Summary 93

CHAPTER 6: Characterization of pressure sensitive adhesives using the BCT 95

6.1 Introduction 95

6.2 Materials and methods 95

6.3 BCT mechanics 102

6.4 Results and discussion 110

6.5 Summary 117

CHAPTER 7: Summary and contributions 119

7.1 Summary 119

7.2 Contributions 123

7.3 Future work 125

CHAPTER 8: APPENDIX 128

8.1 MATLAB code for solving the vKPT BCT 128

8.2 MATLAB code for solving the ABAQUS FE model 141

BIBLIOGRAPHY 165

LIST OF TABLES

Table 4-1: Properties of specimens determined using the bulge test. The gap δ is calculated using the pressure just before the specimen makes contact with the glass substrate. Poisson's ratio is assumed to be 0.49. 61

Table 4-2: Summary of experimental results. Advancing contact data is fitted with equation (4.1) and the receding contact data is fitted with equation (2.6). The numbers inside the brackets are the 95% confidence bounds..... 67

Table 6-1: Three PSA formulations used in this study. 2-ethyl hexyl acrylate (2EHA) is a filler material that does not contribute to acid-base interactions. 96

Table 6-2: Summary of surface energy characterization of the substrates. The advancing contact angles were measured using a goniometer and were based on six measurements. The surface energy components were calculated using the van Oss, Chaudhury and Good method as described in the text..... 97

LIST OF ILLUSTRATIONS

Figure 2-1: Schematic of a contact test between two spheres of equal radii. 12

Figure 2-2: Contact radius as a function of applied force for a spherical indentation test. 15

Figure 2-3: Schematic of a peel test 19

Figure 2-4: Schematic of a DCB test 20

Figure 3-1: Schematic of BCT with key dimensions and quantities labeled 26

Figure 3-2: Center deflection as a function of applied pressure for CPT, vKPT and FE with a (a) clamped edge and (b) pinned edge. Dimensional parameters are used in the FE model. 33

Figure 3-3: Center deflection as a function of applied pressure for CPT, vKPT and FE (black, red and blue colors respectively) with a clamped edge. 34

Figure 3-4: Critical applied pressure as a function of pre-stress for three different thicknesses. CPT is applicable for of the combinations of pre-stress and applied pressures below the lines. 35

Figure 3-5: Center deflection as a function of torsion spring constant for three different pressures. 37

Figure 3-6: Radial displacement as a function of radial position for different values of (a) thickness and (b) torsion spring constant. The color on the lines show the differences between the vKPT solution and FE solution. 38

Figure 3-7: Transverse displacement as a function of radial position for different values of (a) thickness and (b) torsion spring constant. The color on the lines show the differences between the vKPT solution and FE solution. 39

Figure 3-8: Map of the difference between the JKR-type adhesion FE solution and (a) the CPT solution, (b) the vKPT solution. 44

Figure 3-9: Map of pre-stress value that deviates from the classical plate theory solution without pre-stress by 5%. Numbers on line represent the constant gap δ for each line. 45

Figure 3-10: Typical contact radius response as a function of applied pressure calculated using vKPT. The dashed lines represent unstable contact. 46

Figure 3-11: Contact radius as a function of applied pressure for different adhesion ranges calculated using the vKPT model. The Hertz-type contact case is also shown in the plot. 47

Figure 4-1: (a) Center deflection as a function of spring stiffness for a bulge test, results shown for a constant pressure of 100 Pa; (b) Center deflection as a function of applied pressure for a bulge test with a clamped edge. 52

Figure 4-2: Percent difference between analytical solution, $G_{c,ana}$, and FE calculation, $G_{c,FE}$, of strain energy release rate as a function of deflection and thickness for the clamped edge blister contact test in the absence of applied pressure. 55

Figure 4-3: Critical strain energy release rate as a function of contact radius and applied pressure calculated using the FE model. Values are shown for specimen dimensions and elastic properties similar to those used in experiments. 56

Figure 4-4: Schematic of experimental apparatus. 58

Figure 4-5: Vector map of measured displacements on the bottom surface of specimen 2 during a bulge test. The arrows show the direction of displacement and their lengths are the relative magnitudes of the displacements. The outer radius of the specimen is also shown in the figure. 60

Figure 4-6: Radial displacements measured on a bulge test of specimen 2 at different pressures. The markers represent the DIC results fitted with a fourth order polynomial ($R^2 > 0.95$) and the error bars indicate the 95% prediction bounds of the fit. The solid lines are the FE results with E and k_T fit to the DIC results. The dashed lines are the FE results using the fit k_T and ±5% of the fit E. 61

Figure 4-7: Experimental results for specimen 2 showing the effect of pressure rate on contact behavior. The dashed line is a visual aid to distinguish between loading and unloading parts of the data. 63

Figure 4-8: Measured critical strain energy release rate during bonding for (a) specimen 2; (b) specimens 1-3. The data is fitted with equation (4.1) ($R^2 = 0.90$) and the dashed lines are the 95% prediction bounds for the fit. 64

Figure 4-9: Measured critical strain energy release rate during separation for (a) specimen 2; (b) specimens 1-3. The data is fitted with equation (2.6) ($R^2 = 0.83$) and the dashed lines are the 95% prediction bounds for the fit. 65

Figure 4-10: Strain energy release rate during (a) loading ($R^2 = 0.98$) and (b) unloading ($R^2 = 0.99$) for specimen 4 in contact with PDMS coated glass substrate. 68

Figure 5-1: Image of a specimen during the preparation process. The 200 g weight was placed on top of the washer while the cyanoacrylate was curing. The PET film was mounted on a two-inch ring in this image. 72

Figure 5-2:PDMS thickness as a function of (a) spin rates at different Hexane-to-PDMS weight ratios; and (b) Hexane-to-PDMS weight ratios at 4000 rpm. 74

Figure 5-3:Experiment set up of the blister contact test with single camera 3D-DIC implemented. Figure is not drawn to scale. 76

Figure 5-4:Example pressure-time profile and measured contact radius as a function of time for a repeated contact BCT. The data is taken from a 3.5 μm PDMS coating experiment. 77

Figure 5-5: Typical contact-pressure response for a rate-dependent test. The solid lines represent the loading segment and the dashed lines represent the unloading segment. 78

Figure 5-6: (a) Radial and (b) transverse displacements solved with 3D-DIC. The subset size used in 3D-DIC is varied between 5 pixels and 35 pixels. The lines represent the median values of the DIC results; the deviations for each dataset are approximately equivalent for all lines. The red dashed line is the vKPT solution. 5 pixels is equal to 0.14 mm. 80

Figure 5-7: (a) Radial and (b) transverse displacement fields during the bulge test. Solid lines represent the 3D DIC results and dashed liens represent the vKPT model with optimized E, k_T and σ_0. The colored region highlights the 25th and 75th quantiles of the DIC results. 81

Figure 5-8: Images of the contact area during the blister contact test for three different PDMS coating thicknesses. There are spray paint markers present on the bottom surface inside the contact area. The area in contact is brighter in contrast than the area that is not in contact. Conformal contact is seen in the test against 3.45 μm thick PDMS coating. As the thickness drops below 2 μm the quality of the contact degrades quickly. 82

Figure 5-9: Example surface profile of the PET film collected using a white light interferometer. The average surface roughness parameters R_a and R_{rms} are 3.7 and 6.2 nm respectively. 82

Figure 5-10: Contact radius at 12 kPa during loading and unloading as a function of repeated contact cycles. 84

Figure 5-11: (a) Strain energy release rate as a function of contact speed during loading when the contact radius is at 2.5 mm. The dash lines are fits of the data using the equation shown in the figure. (b) Exponent α as a function of the PDMS coating thickness during loading. 87

Figure 5-12: (a) Strain energy release rate as a function of contact speed during unloading when the contact radius is at 2.5 mm. The dash lines are fits of the data using the equation shown in the figure. (b) Exponent α as a function of the PDMS coating thickness during unloading. 88

Figure 5-13: (a) Radial and (b) transverse displacements data as a function of radial position compared against Hertz-type contact BCT simulations for the PET specimen. The solid lines represent the data, long dashed lines represent FE frictionless contact and short dashed lines represent FE no-slip contact. The only distinguishable difference between the two FE solutions is u_r at around 2mm. The data shown is during the loading period. 89

Figure 5-14: (a) Radial and (b) transverse displacements data as a function of radial position compared against Hertz-type contact BCT simulations for the thinner PDMS specimen. The solid lines represent the data, long dashed lines represent frictionless contact and short dashed lines represent no-slip contact. The data shown is during the loading period. 90

Figure 5-15: (a) Radial and (b) transverse displacements data as a function of radial position compared against Hertz-type contact BCT simulations for the thicker PDMS specimen. The solid lines represent the data, long dashed lines represent frictionless contact and short dashed lines represent no-slip contact. The data shown is during the loading period. 91

Figure 5-16: Contact radius as a function of applied pressure for the BCT. The data is for the PET-PDMS contact. The vKPT models assume $G_{load} = 0.17 J/m^2$ and JKR-type adhesion for loading, $G_{unload} = 0.48 J/m^2$, $\delta_{adh} = 10 \mu m$ MD-type adhesion for unloading. 93

Figure 6-1: Surface roughness of the substrates used in the experiments. Each marker represents the result of a line scan using a stylus profilometer. The

boxes and whiskers show the medians and quantiles of the data as described in the text..... 98

Figure 6-2: Schematic of the BCT experiment set up..... 100

Figure 6-3: Typical applied pressure profile and measured contact radius during a BCT experiment. The specimen makes contact with the substrate as the pressure is increased to 16 kPa in the load segment. The pressure is then held at 16 kPa for 6 hours in the load-dwell segment. Afterwards, the pressure is reduced to 12 kPa and held at 12 kPa for 1 hour, before being reduced to 0 kPa in the unload-dwell segment. The pressure rates are at ±40 Pa/s for all ramp periods. 101

Figure 6-4: Mechanical diagram of the blister contact test..... 103

Figure 6-5: Strain energy release rate comparison between FE and vKPT model. The FE simulation includes an adhesive coating with varying Young's modulus and coating thickness. The mechanical properties are taken from the long dwell time experiment (Figure 6-12) during (a) the beginning of load-dwell segment, (b) the end of load-dwell segment, and (c) the end of the unload-dwell segment. 107

Figure 6-6: Correlation between the strain energy release rates calculated using the vKPT model and that calculated using the FE model. The FE model assumes an adhesive layer of 10 kPa in Young's modulus and 15 μm in thickness..... 108

Figure 6-7: (a) Dynamic storage shear modulus and (b) dynamic loss shear modulus master curves of the three types of PSAs measured using a dynamic mechanical tester. The markers represent the data and the lines are the Prony series fits to the data..... 109

Figure 6-8: Comparison of radial displacements between experiment data (markers) and the vKPT (line) calculated using the fitted Young's modulus E and pre-stress σ_0. Two specimens (circle markers, solid lines vs. triangle markers, dashed lines) at three different pressures (6, 12, 16 kPa with black, red, blue colors respectively) are shown..... 111

Figure 6-9: Measured strain energy release rates between the acidic PSA specimen and two different substrates. The box-and-whiskers plots follow the same conventions defined in Figure 6-1. Load data is taken at the end of the 6-hour load-dwell period and unload data is taken at the end of the 1-hour unload-dwell period. 112

Figure 6-10: Measured strain energy release rates for the three different PSAs (10 MRad dosage) in contact with several different substrates. In the analysis to calculate the strain energy release rate, the adhesive layer is assumed to be 15 μm thick and have a Young's modulus of 10 kPa. 114

Figure 6-11: Images of contact area during (a) load, (b) load-dwell and (c) unload-dwell segments for the acidic PSA specimen. The red and green markers are the abest fits of the inner and outer contact edges respectively. Most of the instabilities are observed between the inner and outer contact edges. The data is taken from the acidic PSA in contact with a PMMA substrate. 115

Figure 6-12: Contact radius during the load-dwell period at 16 kPa over 10 days. The corresponding strain energy release rate is approximated by the equation in the figure. The measured G_{FE} increases from 0.09 to 0.24 J/m^2 during the load-dwell period. The data is taken from the acidic PSA specimen in contact with a PDMS surface. 116

Figure 6-13: FE simulations of the BCT with a viscoelastic PSA layer of three different thicknesses included. The mechanical properties for the PSA were taken from the acidic PSA's dynamic mechanical test results, assuming the Poisson's ratio is 0.5. 117

CHAPTER 1: Introduction

1.1 Motivation

Understanding adhesive contact between soft bodies is important in a broad range of applications, including pressure sensitive adhesives [1]–[3], microtransfer printing of semiconductor elements [4], [5], and adhesion in natural and bioinspired systems [6], [7]. Synthetic gecko-inspired tapes [8] rely on the adhesion of many hierarchical shaped setae to adhere on walls and tune the effective separation energy to detach from the surface efficiently. Tapes based on pressure sensitive adhesives (PSAs) are typically engineered to maximize conformal contact and achieve high separation energy to target surfaces through various energy dissipation mechanisms. Microtransfer printing, which is important in the fabrication of emerging devices, exploits changes in separation energy via geometry [9]–[11] or rate-dependence [4], [12], [13] to achieve pick-and-place of small structures from donor to target substrates. These applications require precise characterization of both the adhesion and separation behaviors of interfaces. Quantitative measurements of the adhesion between two bodies is critically important for understanding and optimizing engineered systems that rely on adhesive contact. There are many established test methods to characterize adhesion, however there are numerous challenges for characterizing the adhesion of flat specimens with adhesive surfaces or thin coatings.

1.2 Challenges in traditional adhesion testing instruments

Many common adhesion testing techniques, such as the JKR test or peel test, are well established and documented in the literature [14]–[23]. However, there are a lack of techniques that can characterize both the adhesion and separation behaviors of adhesion on flat sheets (either due to surface forces or a soft adhesive coating). The peel test is an industrial standard [1], [24] for measuring the separation energy of tapes coated with pressure sensitive adhesives and other adhesives on flexible backings. The peel test, however, can only characterize separation properties and the measured peel strength depends on factors, such as the adhesive thickness and modulus, which can be difficult to measure [25], [26]. The JKR test can measure both adhesion and separation properties, but thickness effects can make the use of the JKR test on thin coatings difficult. Accounting for the substrate effects can be challenging in the JKR test and this limits its use on PSAs [27]. Therefore, there is a critical need to develop a new adhesion testing.

1.3 Objective

The main objective of this dissertation is to develop an alternative adhesion testing method, the blister contact test (BCT), to characterize adhesion and separation properties of flat and thin specimens. There are five sub-objectives in this work:

- Investigate the design and mechanics of the BCT.
- Implement the BCT experimentally.

- Experimentally investigate rate-dependent adhesion of an elastomer (poly(dimethylsiloxane) – PDMS) using the BCT.
- Investigate the thickness and viscoelasticity effects of a polymer coating on specimen to rate-dependent adhesion and separation behaviors using the BCT.
- Experimentally characterize pressure sensitive adhesives using the BCT.

1.4 Scope of dissertation

The BCT has only been studied in a few papers [28]–[32]. In the previous work, key assumptions were made to simplify the analysis. For example, [28] uses a membrane analysis model which assumes that membrane stress is the dominant deformation mechanism. However, for specimens that deviate from the geometric parameters used in this previous report, other deformation mechanisms, such as bending or shear deformation, may be important in the analysis. Chapter 3 presents mechanics models for the design and analysis of a BCT. The chapter begins with a derivation of equations to describe the BCT using both classical plate theory and von Kármán plate theory. Finite element modeling is used to assess the validity of these analytical models. The effects of bending, membrane, and shear stresses are investigated analytically and numerically. Ranges over which each of these deformation mechanisms are significant are established. Other effects commonly found in experiments, such as pre-stress and compliant edge clamping, are also examined. In addition, analyses were also presented for the calibration stage of the BCT. This chapter

provides a comprehensive guide of the mechanics theory needed to design and implement the BCT.

The experimental implementation of the BCT is first discussed in Chapter 4. In the experiments in this chapter, rate-dependent adhesion and separation behaviors of polymers in contact with a stiff substrate were studied. PDMS was used as the specimen because of its well characterized elastic and rate-dependent adhesion properties. Glass and PDMS-coated glass substrates were chosen as the contact surface as they are common substrates that PDMS is often in adhesive contact with. 2D digital image correlation (2D-DIC) was implemented in the BCT to monitor the in-plane displacements of the specimens in order to measure the elastic properties of the specimen and assess the compliance of the clamped boundary. The separation behavior measured in the PDMS-glass BCT experiments were in agreement with literature. For the loading data, a modified empirical model was proposed to describe the rate-dependent behavior during advancing contact.

In Chapter 4, the rate-dependent adhesion and separation behavior that was observed was attributed to the bulk viscoelasticity of the PDMS specimen. However, the effects of the bulk viscoelasticity of the PDMS was not studied in detail in Chapter 4. Chapter 5 examines the effect of the bulk viscoelasticity on rate-dependence. Polyethylene terephthalate (PET) films are used as specimens and silica disks with PDMS coatings of different thicknesses are used as substrates. By systematically changing the PDMS coating thickness (i.e. the volume of viscoelastic material), the rate-dependent adhesion and separation behaviors were measured. Correlations between the rate-dependence and the

PDMS thickness were established. It was found that the exponent in the empirical models (equations (2.6) and (4.1)), commonly assumed to be 0.6, depends on the PDMS thickness. Thinner PDMS coating resulted in less rate-dependence in adhesion.

In the experiments in Chapters 4 and 5, markers for 2D-DIC were applied strictly outside of the view of the contact area. This limited the ability of the BCT to determine the friction condition inside the contact area with the lack of resolved displacement data. As such, 3D-DIC was implemented on the entire specimen in Chapter 5 to improve the quality of the measurement technique. The in-plane and transverse displacements were tracked everywhere inside the specimen, including the area that makes contact. The improvement in the system allowed for a close examination of the effects of friction on the BCT. Friction was observed in both PET-PDMS and PDMS-silica contact tests and the effects of friction were modeled using a modified vKPT model of the BCT.

One of the most common applications in adhesion characterization for flat flexible specimen geometries is tape. The study of adhesion and separation behavior of PSAs coated on thin backings is important for understanding performance in applications. Chapter 5 investigates the nature of adhesion with PSA specimens against different substrates using the BCT. These PSA specimens have different chemical compositions designed to adhere onto specific surfaces more strongly than others. The analyses from Chapter 3 also showed that the deformation mechanisms for these tape specimens (i.e., PSA on a flexible backing) are vastly different from the PDMS specimens in Chapter 4 – the tape specimens deform by membrane and bending stresses whereas the PDMS

specimens deform by bending and shear stresses. A series of BCT experiments between the different specimen-substrate pairs were done to investigate the effects of acid-base interactions on PSA adhesion. The experimental results qualitatively agreed with the standard methods for characterizing acid-base interactions of surfaces.

Chapter 7 summarizes the work and contributions in this dissertation. The BCT was studied theoretically and experimentally. Adhesion experiments involving elastomers and pressure sensitive adhesives were done to study rate effects and acid-base interactions among others. Finally, recommendations for future work are made in the final section of Chapter 7.

CHAPTER 2: Literature review

2.1 Fundamentals of adhesion

When two bodies are brought to contact, the energy in the system changes as a result of the loss of two surfaces and the formation of an interface. The work of adhesion is the energy difference in this process, i.e. $W_a = \gamma_1 + \gamma_2 - \gamma_{12}$. The first two terms are the surface energies and the last term is the interfacial energy. For each surface, the surface energy may be composed of multiple components, $\gamma = \gamma^d + \gamma^p + \cdots$, including a dispersive component, γ^d, and a polar component, γ^p [33]. The dispersive component is due to intermolecular attractions, such as van der Waals' attraction. The polar component is related to the chemical bonding between two molecules. Other components, such as covalent and ionic bonds, are typically stronger than these two components and sometimes irreversible. The adhesion studied in this work is generally reversible and thus the attention is focused on the investigation of dispersive and polar components of adhesion.

In addition to intermolecular forces, there are other factors that can affect the work of adhesion between surfaces. For example, moisture in the air can condense between surfaces and increases the effective interaction range between surfaces [34]. Uncured polymer chains may bridge across the contact opening to increase the work of adhesion and acts over very large ranges [35]. This may also lead to differences in measured adhesion for contact formation versus separation [28].

2.1.1 Dispersive interaction

van der Waals forces are dispersive forces that act between all molecules. When two molecules are far apart, the van der Waals interactions are small. As the separation decreases, the attraction from van der Waals forces increases, but the forces become repulsive if the two molecules are too close to each other. The van der Waals forces are balanced when the two molecules are at an equilibrium separation.

The 6-12 Lennard-Jones potential is typically used as an approximate model to describe the van der Waals forces between the two molecules [36]. For the equivalent surface interaction between the two molecules, the 6-12 Lennard-Jones potential is integrated over the surface area to obtain the 3-9 Lennard-Jones model, which represents the surface interaction in a 2-term polynomial form: $\sigma_{\mathrm{LJ}}(z) = C\left[(A/z)^9 - (A/z)^3\right]$, where A and C are constants and z is the distance between the two surfaces. The shape of the Lennard-Jones potential is analogous to the van der Waals forces that it is repulsive when the spacing between the two molecules are very small, becomes attractive when the spacing increases but then decays quickly as the spacing increases further. Typically, the interaction range is very small (typically less than 10 nm) compared to the size of contact area and even surface roughness in many cases. Furthermore, van der Waals forces are much weaker than permanent bonds such as covalent bonds or ionic bonds.

2.1.2 Adhesion of pressure sensitive adhesives

Pressure sensitive adhesives (PSAs) are important in many industrial and commercial applications. They have a wide variety of uses ranging from the bonding of automotive body panels to medical tapes [1], [37], [38]. In some cases, PSAs are used to bond two surfaces together permanently while in other cases, such as for medical tapes, PSAs are designed to adhere strongly, but must also be able to be easily detached from the surface when needed. In selecting a PSA, it is important to understand both the adhesion and separation behaviors. Over-aggressive PSAs can cause damage when removed from surfaces (e.g., skin in the case of medical tapes, or paint in a masking application), but PSAs that are not tacky enough may not adhere to the surface well enough during initial contact. Therefore, it is crucial to characterize both the adhesion and separation behaviors of PSAs.

PSAs are very soft polymers that are often coated on a thin backing layer when used as tapes. To have good adhesion strength in practical applications, the Dahlquist criterion which suggests an upper limit of around 0.1 MPa for the storage modulus must be met [39]. PSAs that satisfy the Dahlquist criterion are able to "wet" the contacting surface spontaneously and provide good adhesion. Thus, PSAs tend to have very low elastic modulus and are coated in thin layers of 100 μm or less. In the case of tapes, the PSA is coated on a backing layer that is flexible due its thinness, but has a much higher elastic modulus than the PSA, for example polyethylene terephthalate (PET) has a modulus greater than 1 GPa. The fact that the PSA is coated in a thin layer on a high modulus, but

flexible substrate, makes adhesion testing of the PSAs challenging as many test techniques result in adhesion measurement that is affected by the properties of both the PSA and the backing.

Adhesion is governed by the interactions between two surfaces coming into contact. Generally, PSAs adhere onto the substrate via dispersive forces that are typically weak and the PSA can be detached from the substrate reversibly. If the active chemical composition of the PSA has the opposite polarity of the target substrate, stronger bonds due to acid-base interactions may form and enhance adhesion [40]. The chemical interaction between the two surfaces increases the adhesion strength beyond what is achieved via dispersive forces alone. This polar interaction can be due to the Lewis acid-base interactions of the two surface [40]–[42]. In this case, one surface acts as an electron donor (or base, or proton acceptor) and the other surface acts as an electron acceptor (or acid, or proton donor). This polar component can also be due to dipole-induced dipole attraction, but its contribution is miniscule for solid-solid contact pairs [38]. Unlike the dispersive component, the polar component does not exist for a contact pair that has same polarity (acid-acid, base-base) or if one of the surfaces is neutral. PSAs with different chemical compositions can be designed to adhere more favorably to specific target substrates via acid-base interactions. A table of the polar surface energy components for various surfaces can be found in [38] and can be used to design effective PSAs.

2.2 Adhesion mechanics

The foundational contact mechanics theory of Hertz was first proposed in the 19th century [43]. Hertz derived the relationship for the mechanical response of two elastic spheres being pushed together (Figure 2-1). The spheres deform elastically under the contact force into conformal contact. The relationship between the contact radius, b, and applied force, F, for two elastic spheres of equal radii R is:

$$b = \left(\frac{3FR}{4E^*}\right)^{1/3}, \tag{2.1}$$

where E^* is the reduced modulus of the sphere. The Hertz theory assumes the interface is frictionless and adhesionless. In addition, the deformations must be in small strain regime, and the contact size must be smaller than 10% of the radius of the sphere. Under the assumptions of Hertz theory, the contact is completely reversible for loading and unloading.

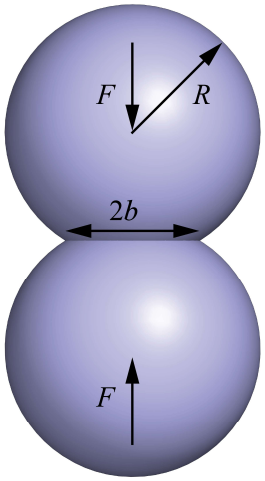

Figure 2-1: Schematic of a contact test between two spheres of equal radii.

While the Hertz theory provides a satisfactory result for describing the contact between two elastic spheres, the model does not account for adhesive forces which can affect the deformation of soft materials. Johnson et al. [44] included the effect of adhesion between solids by introducing an adhesive energy into the total energy of the system, this analysis is now known as the JKR theory. In static equilibrium, the total energy is minimized, resulting in an equation that relates the contact radius with the applied force and the interfacial energy per unit area of each surface, W_a:

$$16\pi W_a E^* b^3 = \left(F - \frac{4E^* b^3}{3R} \right)^2 \tag{2.2}$$

The same assumptions used in the Hertz theory are also valid for the JKR theory. Moreover, the adhesion forces must be small compared to the opening gap so that all of the contribution of the adhesion energy is inside the contact area. A significant distinction

between the Hertz and JKR theory is that in the JKR theory there is a finite contact area even when the applied force reduces to zero. A negative force $F = -\frac{3}{2}\pi W_a R$ is required to detach the spheres and the contact area shrinks from $b = \left(9W_a R^2/4E^*\right)^{1/3}$ to zero spontaneously. This negative force is commonly used to report the adhesive force.

For stiffer and/or smaller spheres, the JKR theory cannot sufficiently describe the adhesive response. As suggested in the van der Waals interaction, the adhesion force is due to the attraction (and repulsion) between two molecules in each body. When the range of interaction is large compared to the size of the spheres, or the adhesion force is small compared to the modulus of the spheres, then the spheres are expected to retain the shape of the deformation found in Hertz theory. In such cases, the DMT theory [45] is used in place of the JKR theory to describe adhesion. The relationship between contact radius and adhesion is:

$$\frac{4E^* b^3}{3R} = F + 2\pi W_a R \tag{2.3}$$

In this case, a negative force $F = -2\pi W_a R$ is needed to detach the spheres, but the contact area decreases gradually to zero in this process. Note, both the JKR theory and DMT theory reduce to Hertz theory in the absence of adhesion, $W_a \to 0$.

The connection between JKR theory and DMT theory can be established by assuming an adhesive traction that acts over a finite range. In this theory, also known as the Maugis-Dugdale (MD) theory, a constant adhesion stress σ_{adh} acts over an adhesion

range δ_{adh}, and the work of adhesion is defined as $W_a = \delta_{\text{adh}}\sigma_{\text{adh}}$. An adhesion range parameter, λ, is introduced and the result of the mechanics problem is a system of equations [46], [47]:

$$\frac{\lambda\tilde{b}^2}{2}\left[\sqrt{m^2-1}+\left(m^2-2\right)\operatorname{atan}\sqrt{m^2-1}\right] + \frac{4\lambda^2\tilde{b}}{3}\left[\sqrt{m^2-1}\operatorname{atan}\sqrt{m^2-1}-m+1\right]=1 \tag{2.4}$$

$$\tilde{F} = \tilde{b}^3 - \lambda\tilde{b}^2\left[\sqrt{m^2-1}+m^2\operatorname{atan}\sqrt{m^2-1}\right]$$

The dimensionless parameters are:

$$\tilde{b} = \frac{b}{\left[\frac{3\pi W_a R^2}{4E^*}\right]^{1/3}}, \tilde{F} = \frac{F}{\pi W_a R}, \quad \lambda = \frac{2W_a}{\delta_{\text{adh}}\left[\frac{16\pi W_a E^{*2}}{9R}\right]^{1/3}}, m = \frac{b+b_{\text{adh}}}{b} \tag{2.5}$$

where the opening between the two surfaces at $r = b + b_{\text{adh}}$ is equal to δ_{adh}. The two equations in equation (2.4) must be solved numerically to yield a relationship between the contact radius and adhesion. The range of λ represents the transition between JKR and DMT theories. When the adhesion range λ is very small, the equations reduce to that for the DMT theory. When the adhesion range is very large, the JKR theory is retrieved from these equations. Figure 2-2 shows the typical contact response using the four different

contact theories. The MD theory curve falls between the JKR and DMT theory curves that serve as the limits at the same adhesion.

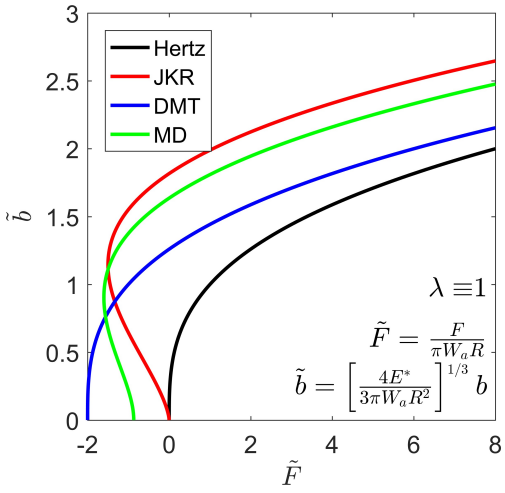

Figure 2-2: Contact radius as a function of applied force for a spherical indentation test.

2.3 Rate-dependent adhesion

Critical strain energy release rate, G_c, is often used to describe interface adhesion. The critical strain energy release rate of an interface is also sometimes referred to as an interface toughness, Γ. Critical strain energy release rates measured in experiments are often larger than the thermodynamic work of adhesion W_a. This is primarily due to effects other than adhesion that cause significant energy dissipation during separation of an interface. Separation rate can have a significant effect on critical strain energy release rate. Material response (e.g. viscoelasticity) and chemical response (e.g. rearrangement of elastomer chains) can both contribute to this rate-dependence [48]. The rate-dependence can be

leveraged in processes such as micro-transfer printing to control adhesion through peeling rate [4], [13]. There are numerous studies of rate dependent adhesion for a range of systems (e.g., [49]–[51]).

The origin of rate-dependence may be from chemistry or mechanics. Chemically, uncured polymer chains may migrate to the contacting surface can lead to adhesion hysteresis that is dependent on contact time [52], [53]. Mechanically, viscoelastic materials demonstrate strong rate-dependent adhesion [51]. Theoretical models for viscoelastic cracks have been proposed to distinguish the rate dependence in adhesion and separation contact behaviors [54], [55]. Greenwood illustrated the connection between viscoelasticity of a material and the measured rate-dependent adhesion and separation [49], [50], [55]. Generally, the viscoelastic behavior of the material enhances the measured adhesion by $G_c = G_0\left[1 + \phi(a_T v)\right]$, where $\phi(a_T v)$ is a temperature and rate-dependent viscoelastic term [50], and G_0 is a steady state strain energy release rate that may be higher than W_a due to other unaccounted dissipation mechanisms.

When the contact size is increasing, $G_{c,\text{adv}}$, G_c during advancing contact, decreases as the contact area growth rate increases. Conversely, when the contact size is decreasing, $G_{c,\text{rec}}$, G_c during receding contact, increases as the separation rate increases. In the theoretical models in [49], [50], the adhesion and separation energies decrease and increase as functions of contact speed in a similar fashion. There is a diminishing change in adhesion at high contact velocities, limited by the instantaneous modulus of the viscoelastic material. Experimentally, rate-dependent interface properties have been characterized by peel-tests,

dynamic JKR tests [14], and rolling ball/cylinder tests [56]. The rate-dependent behavior during separation is usually described by an empirical form proposed by Gent and Schultz [57]. The model characterizes rate-dependent adhesion as a function of the steady state adhesion $G_{c,\mathrm{rec}}$, a characteristic velocity v^*_{rec} and a scaling exponent n,

$$G_{c,\mathrm{rec}} = G_{0,\mathrm{rec}}\left[1 + \left(-\frac{db}{dt}\Big/ v^*_{\mathrm{rec}}\right)^n\right] \tag{2.6}$$

This form has been widely adopted for describing work of separation values measured as a function of separation rate. The exponent n is empirically determined and usually found to be around 0.6 for many polymer materials [51]. Unlike some proposed theoretical models [54], [55], there is no upper bound of $G_{c,\mathrm{rec}}$ in this empirical form.

To the best of the author's knowledge, there is not an established empirical form for describing the effect of rate on the work of adhesion that is measured when the contact area is increasing in size.

2.4 Adhesion testing methods

Accurate characterization of the adhesion of soft materials is critical for many industrial applications. Adhesion testing instruments, for example the indentation test, peel test and DCB test, are widely used in commercial and academic applications. These testing instruments are specialized in testing certain types of specimens. The indentation test works well for specimens that are large compared to the size of indentation probe [27], [58]. For tape-like specimen geometries, the peel test is the industrial standard [16], [25], [37]. The

DCB test is recommended for structural adhesives that have high adhesive strength [35], [59], [60].

2.4.1 Indentation test

An indentation test with a spherical probe is a direct application of the JKR theory. In an indentation test, a rigid indenter is pushed into contact with the specimen. Depending on the size of the indenter and the modulus of the specimen, equation (2.2) or (2.3) can be used to extract the strain energy release rate, $G = W_a$. In many cases where the specimen modulus is also not known, the displacement of the indenter can also be monitored and E^* and G can be obtained through fitting the data.

The indentation test analysis only applies to specimens that can be assumed to be an elastic half-space. When the specimen is a thin adhesive coating (relative to the contact radius) on a much stiffer substrate, for example a tape geometry, equation (2.2) over-estimates the G value (the measured force is larger at the same contact radius). This substrate effect has been studied extensively in literature for mechanical characterization via flat punch indentation of thin films [27], [61]. Similar approaches can be pursued for a spherical indenter to derive an empirical correction for the measured G values to account for substrate effect.

2.4.2 Peel test

A key challenge in using the indentation test is the need to account for substrate effect when the specimen or adhesive thickness is comparable to or smaller than the contact radius. For a flexible specimen with a thin adhesive coating, the peel test is a more suitable test geometry to use (Figure 2-3). During a peel test, a thin rectangular strip with an adhesive coated on one side is adhered onto a flat substrate. The strip is pulled from the substrate at a fixed angle and fixed displacement rate. The strain energy release rate is calculated from the measured force as

$$G = \frac{F}{B}(1 - \cos\theta), \tag{2.7}$$

where θ is the peel angle, F is the measured force and B is the width of the specimen. The peel front is often monitored to extract additional information about the PSA failure, e.g. fibrillation or cavitation of soft polymers, and improve the accuracy of the model [25].

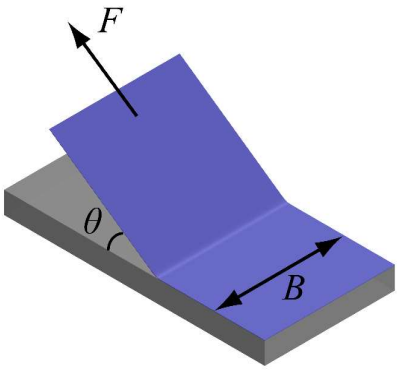

Figure 2-3: Schematic of a peel test

2.4.3 DCB test

In the double cantilever beam (DCB) test (Figure 2-4), an adhesive layer is sandwiched between two rectangular beams which are then separated using a tensile machine [59], [62]. The strain energy release rate is determined from the measured load, F, and crack length, a, as

$$G = \frac{12F^2a^2}{B^2h^3E^*}, \tag{2.8}$$

where h, B and L are the thickness, width, and length of the beam, and a is the unbonded length of the DCB specimen. The DCB test is more commonly used for structural adhesives where the fracture toughness of the adhesives tends to be much larger [35] but has also been applied to PSAs [63].

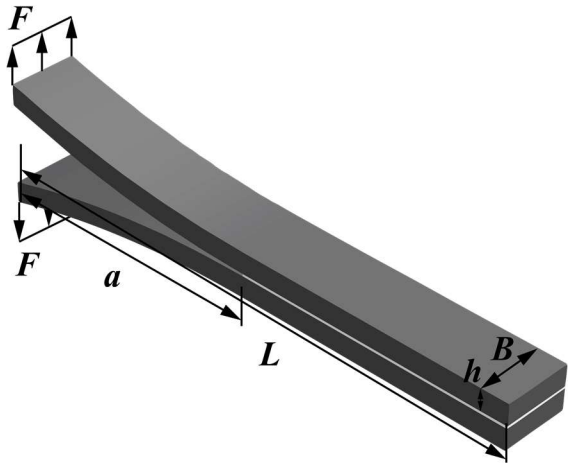

Figure 2-4: Schematic of a DCB test

2.5 Bulge test and blister contact test

Several experimental configurations based on circular pressurized flat sheets have been investigated over the past several decades for the characterization of the adhesion and separation properties of interfaces. One of the alternative geometries is the blister test [64]–[71]. A flat sheet is adhered to a rigid substrate containing a circular hole, pressure is applied through the hole and the sheet delaminates from the substrate axisymmetrically. By tracking the applied pressure and the blister radius, the adhesion can be characterized. In a pressure controlled blister test, the blister radius grows unstably once the critical strain energy release rate is reached [64]. A way to prevent unstable blister propagation is to control the volume of the blister [72]–[74]. A fixed amount of fluid is trapped within the blister and the change in external pressure deforms the blister. Directly controlling the volume via injecting an incompressible fluid is also possible [65]. This configuration is stable at all stages of the test.

The blister test is not capable of characterizing adhesion during crack closure (contact formation). A modified blister test, referred to as the blister contact test (BCT), can be used to characterize both advancing and receding contact [75]. The flat sheet is clamped around the circular hole and the adhesive side is pressurized into contact with a rigid substrate. By tracking the contact area and applied pressure, the strain energy release rate may be extracted during advancing or receding contact (adhesion and separation) as the applied pressure increases or decreases. Furthermore, by controlling the rate of applied pressure, the contact propagation rate can be controlled and rate dependent adhesion can

be characterized. The BCT was used in [28], [30] to measure the adhesion between glass and various films. An adhesion mechanics model was developed using membrane theory, with the MD-type adhesion, and showed good agreement with the experimental results.

An attractive feature for the BCT is its two stage testing configuration – the BCT is preceded by a bulge test (BT) [29], [76], [77]. In the BT, the specimen has yet to make adhesive contact with the substrate. The BT mechanics is identical to the blister test except the edge is clamped so the specimen radius is fixed and there is no delamination at the edge. During the BT, the displacement data is collected as a function of applied pressure. Using a mechanics model, the specimen can be calibrated without the influence of adhesion.

2.6 Optical measurement techniques

Traditional test methods such as the JKR test uses the load-displacement data to extract adhesion properties between two bodies. However, to extract more information such as the characteristics of the adhesion range, measurements of the contact area as well as the deformation outside of the contact area are needed. Destructive measurement techniques are not ideal for these types of measurements as the contact responses may be disrupted by the techniques. Typically, optical measurement techniques are preferred as they can be non-intrusive and non-destructive. A simple method for monitoring the contact area in JKR or blister tests is by axially imaging the contrast changes of the contact area made between the two bodies if one of the two bodies is transparent [78]. Alternatively, a side-view of the

contacting bodies is commonly used in peel tests to observe the deformation near the crack tip [25].

Several techniques are available to measure the deformation outside the contact area during an experiment. Interferometry is a group of optical techniques that makes use of interference fringes of lights to extract spatial information. Moiré interferometry has been used to extract the surface profiles of deformed objects [29], [79]–[81]. White light interferometry leverages the coherence length of light to achieve nanometer spatial resolution of surface profile [82]. Monochromatic light interferograms have been used in experiments to observe microscale crack front propagation [71], [83].

2D digital image correlation (2D-DIC) is a method to measure the full field displacement profile non-destructively [84]–[86]. Using a telecentric camera and lens system that captures a sequence of images during the experiment, any unique feature that deforms within the focal plane during the experiment can be identified uniquely in the sequence. The correlation between the images is the in-plane displacement of the body. This method can only measure in-plane deformations and is also limited to unique features only. A common way to artificially create unique features on the test specimen is to spray paint speckles onto the test surface during specimen preparation.

3D-DIC is an extension of 2D-DIC that enables 3D displacement data to be recorded. In 3D-DIC, typically two cameras are placed at different incident angles to the specimen and used to record two images of the experiment simultaneously [87], [88]. The

two images at different angles can be combined to form 3D displacement data using a calibrated correlation function. However, due to the need to have two identical camera systems and the complexity of the calibration process, 3D-DIC is not as widely used as 2D-DIC. Recently, 3D-DIC was successfully implemented using a single camera system [89]–[91]. In this modified technique, a transmission diffraction grating is placed between the specimen and the camera system. A monochromatic light source is used in place of white light. The diffraction grating produces virtual images that are effectively at an angle normal to the specimen. Using the diffraction grating equation, the angle can be calculated and the displacement relationship between two diffraction images can be computed. This technique is more cost effective and requires less control on camera calibration and synchronization. Other similar methods that are conceptually equivalent, but with different optical elements, can be used to implement 3D-DIC with a single-camera system [92].

CHAPTER 3: Design and mechanics of the BCT

3.1 Introduction

The blister contact test (BCT) is a two-stage test that is preceded by a bulge test (BT). The only difference between the BT and BCT is that the applied pressure during the BT is not sufficient to push the specimen into contact. It is easy to view the BCT as a deformed plate in contact with a rigid substrate. However, this chapter shows that even for a thin plate geometry where the radius-to-thickness ratio is less than 10, the BCT mechanical response can be complicated by other deformation modes such as shear and membrane stresses. Accounting for the deformation from membrane or shear stresses can be challenging in analytical models. This chapter covers the details of the mechanics analyses of the BT and the BCT using a nonlinear plate theory and a finite element model. Effects that are often neglected in theoretical analyses but important in experiments, such as compliant clamping, are also included in this study.

3.2 Specimen mechanics

Figure 3-1 shows a schematic of the BCT. A circular specimen of radius R and thickness h is nominally clamped along the edge and loaded by a uniform pressure, q. A rigid flat surface is placed at a fixed distance, δ, above the top surface of the specimen. The specimen is assumed to be axisymmetric, linear elastic, homogeneous, and isotropic with Young's modulus E and Poisson's ratio ν. A pre-stress, σ_0, may be present in the specimen as a

result of mounting. Furthermore, it is difficult to achieve perfectly clamped boundary conditions in experiments. This can lead to compliance at the boundary, which is represented here as a torsion spring of stiffness k_T that restricts the rotation and a linear spring of stiffness k_R that restricts radial displacement at the edge.

Adhesion between the specimen and the rigid surface is characterized by the strain energy release rate, G, the interfacial energy per unit area needed to bring the specimen and rigid surface into adhesive contact. The adhesion may also be described by an adhesive traction σ_{adh} that acts near the contact edge when $r \leq b + b_{\text{adh}}$ or when $\delta - w(r) \leq \delta_{\text{adh}}$, where r is the radial position. Section 3.4.2 discusses three common types of contact models in detail – the Hertz-type contact, the JKR-type adhesion and the Dugdale-type adhesion models.

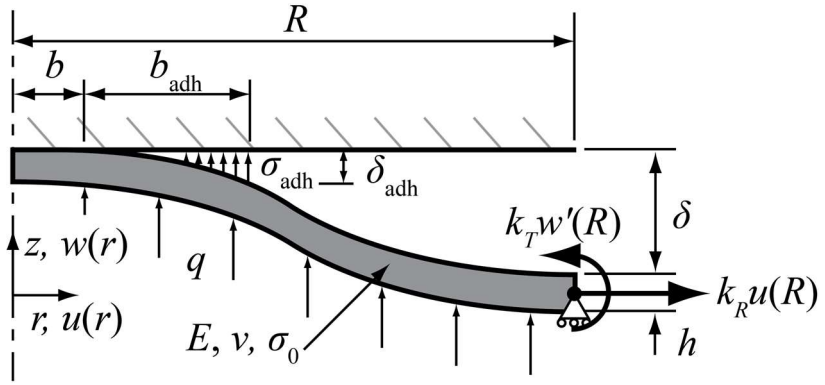

Figure 3-1: Schematic of BCT with key dimensions and quantities labeled

BCT models based on classical plate theory (CPT) and von Kármán plate theory (vKPT) are developed in this work. These models have different assumptions that lead to

the analysis of either only bending deformation (CPT) or coupled bending and stretching deformation (vKPT). In both models, the system is assumed to be axisymmetric and the mid-plane displacements are functions of the radial position r. The radial displacement through the thickness of the plate is given as $u(r,z) = u(r) - zw'(r)$, where w is the transverse displacement in the z-direction and the derivatives of displacements are written as $(\,)' = \mathrm{d}(\,)/\mathrm{d}r$. Dimensionless parameters in the models are denoted by a tilde $\left(\tilde{\ }\right)$ and are defined as follows:

$$\tilde{q} = \frac{qR^3}{D}; \tilde{\sigma}_{\mathrm{adh}} = \frac{\sigma_{\mathrm{adh}}R^3}{D}; \tilde{\sigma}_0 = \frac{\sigma_0 hR^2}{D};$$

$$\tilde{\delta} = \frac{\delta}{R}; \tilde{b} = \frac{b}{R}; \tilde{h} = \frac{h}{R}; \tilde{r} = \frac{r}{R}; \tilde{u}(\tilde{r}) = \frac{u(r)}{R}; \tilde{w}(\tilde{r}) = \frac{w(r)}{R}; \tag{3.1}$$

$$\tilde{b}_{\mathrm{adh}} = \frac{\tilde{b}_{\mathrm{adh}}}{R}; \tilde{\delta}_{\mathrm{adh}} = \frac{\delta_{\mathrm{adh}}}{R}; \tilde{k}_R = \frac{k_R Rh^2}{12D}; \tilde{k}_T = \frac{k_T R}{D}; \tilde{G} = \frac{GR^2}{D}$$

where $D = Eh^3/12\left(1-\nu^2\right)$ is the flexural rigidity of the specimen. Only pre-stresses that lead to tension in the specimen are considered in this work, $\sigma_0 \geq 0$. Only elastic deformation is considered.

3.2.1 von Kármán plate theory

The vKPT assumes the material undergoes small deformations and moderate rotations. This theory permits stretching along the mid-plane of the specimen, in addition to bending rotations about the mid-plane. However, the surface normal to the plane of the specimen

remains perpendicular to the specimen after deformation. The governing equations are [32]:

$$\tilde{u}'' + \frac{\tilde{u}'}{\tilde{r}} - \frac{\tilde{u}}{\tilde{r}^2} = -\frac{1-\nu}{2\tilde{r}}\widetilde{w}'^2 - \widetilde{w}'\widetilde{w}'' \tag{3.2}$$

$$\frac{\widetilde{w}'}{\tilde{r}^3} - \frac{\widetilde{w}''}{\tilde{r}^2} + \frac{2\widetilde{w}'''}{\tilde{r}} + \widetilde{w}'''' = \frac{12}{\tilde{h}^2}\left[\begin{array}{l}(1-\nu)\left(\dfrac{\tilde{u}\widetilde{w}'}{\tilde{r}^2} - \dfrac{\tilde{u}'\widetilde{w}'}{\tilde{r}} - \dfrac{\widetilde{w}'^2}{2\tilde{r}}\right) \\ +\nu\dfrac{\tilde{u}\widetilde{w}''}{\tilde{r}} + \tilde{u}'\widetilde{w}'' + \dfrac{\widetilde{w}'^2\widetilde{w}''}{2}\end{array}\right] + \tilde{\sigma}_0\left(\frac{\widetilde{w}'}{\tilde{r}} + \widetilde{w}''\right) + \tilde{q} + \tilde{\sigma}_{\mathrm{adh}}(\tilde{r}) \tag{3.3}$$

The radial and transverse displacements are coupled in this theory so the governing equations must be solved simultaneously. In this work, the equations are recast into a system of first order equations and solved using the `bvp4c` function numerically in MATLAB [93]. When the thickness is small, the terms on the right-hand side of equation (3.3) are large compared to the left-hand side and the governing equations reduce to that for a membrane theory. However, the equations are still coupled so a numerical method like the one described here is still required.

3.2.2 Classical plate theory

The CPT assumes the specimen undergoes small deformations and rotations. As a result, only bending deformation is considered. If the transverse displacement is small compared to the specimen thickness, the square-bracketed term in equation (3.3) can be omitted and the governing equation for the CPT becomes [94], [95]:

$$\frac{\widetilde{w}'}{\tilde{r}^3} - \frac{\widetilde{w}''}{\tilde{r}^2} + \frac{2\widetilde{w}'''}{\tilde{r}} + \widetilde{w}'''' = \tilde{\sigma}_0 \left(\frac{\widetilde{w}'}{\tilde{r}} + \widetilde{w}'' \right) + \tilde{q} + \tilde{\sigma}_{\text{adh}}(\tilde{r}) \tag{3.4}$$

The transverse displacement is only a function of the radial position in this equation. In the absence of adhesion stress, $\tilde{\sigma}_{\text{adh}}(\tilde{r}) \to 0$, the equation can be re-written into the form of an inhomogeneous modified Bessel's equation, which possesses the following general solution [95]:

$$\widetilde{w}(\tilde{r}) = -\frac{\tilde{q}}{4\tilde{\sigma}_0}\tilde{r}^2 - C_1 \log \tilde{r} + C_2 \left[I_0\left(\sqrt{\tilde{\sigma}_0}\tilde{r}\right) - 1 \right] - C_3 K_0\left(\sqrt{\tilde{\sigma}_0}\tilde{r}\right) + C_4 \tag{3.5}$$

where $I_i(\xi)$ and $K_i(\xi)$ are the i$^{\text{th}}$ order modified Bessel's functions of the first kind and second kind for ξ respectively. The constants of integration C_1, C_2, C_3, C_4 can be obtained by solving the respective boundary conditions for the problems listed in the following sections. Once the transverse displacement is solved, $w(r)$ can be inserted into the other governing equation (3.2) and with the appropriate boundary conditions the radial displacement $u(r)$ can be obtained.

3.3 Bulge test

Before the applied pressure is sufficient to cause the specimen to contact with the reference surface (i.e., $\widetilde{w}(0) \leq \tilde{\delta}$), the experiment is known as a bulge test (BT). The mechanics of the BT have been extensively discussed [29], [76], [95]–[98]. As there is no contact between the specimen and the substrate, the mechanical properties of the specimen can be extracted at this stage. In particular, the modulus of the specimen E, pre-stress induced by the specimen preparation process σ_0, and the compliant boundary conditions, k_T and k_R,

can be extracted at this stage if the test setup allows for measurement of radial and/or out-of-plane displacements of the specimens.

3.3.1 Boundary conditions

The boundary conditions are given in terms of displacements $\widetilde{w}$ and $\tilde{u}$. As the specimen is axisymmetric, the slope, and radial displacement must be zero at the center, $\tilde{r} = 0$. In addition, the transverse shear force is zero at the center due to symmetry. Since the governing equations are singular at the center [97], the boundary conditions are evaluated numerically at a small distance from the center, $\tilde{r} = \Delta\tilde{r}$. The corresponding boundary conditions are:

$$\widetilde{w}' = 0 \tag{3.6}$$

$$\widetilde{w}''' + \frac{\widetilde{w}''}{\tilde{r}} = 0 \tag{3.7}$$

$$\tilde{u} = 0 \tag{3.8}$$

At the outer edge, $\tilde{r} = 1$, there is a compliant support defined in term of two spring stiffnesses, yielding the following boundary conditions:

$$\widetilde{w} = 0 \tag{3.9}$$

$$\widetilde{w}'' + \left(\nu + \tilde{k}_T\right)\widetilde{w}' = 0 \tag{3.10}$$

$$\tilde{u}' + \frac{\tilde{h}}{2}\widetilde{w}'^2 + \left(\nu + \tilde{k}_R\right)\tilde{u} = 0 \tag{3.11}$$

For a perfectly clamped edge, $\tilde{k}_T, \tilde{k}_R \to \infty$ and $\tilde{w}$, $\tilde{w}'$, $\tilde{u}$ are zero. For a pinned edge, $\tilde{k}_T \to 0, \tilde{k}_R \to \infty$, the boundary condition in equation (3.10) represents a zero moment. The constants in CPT are solved using boundary conditions in equations (3.6), (3.7), (3.9) and (3.10). The solution for vKPT requires all six boundary conditions. Once the equations are solved, the limit of $\Delta\tilde{r}$ is taken to zero to obtain the BT solution.

3.3.2 Finite element simulation

A finite element (FE) model is developed to understand the applicable ranges of CPT and vKPT. The FE model is implemented in ABAQUS using 2D axisymmetric continuum elements (CAX4) [99]. Uniform pressure q is applied on the bottom surface of the specimen. The compliant boundary conditions of equations (3.10) and (3.11) are implemented by tying the edge nodes together as a rigid body with a reference node at the mid-plane, and attaching this node to torsion and linear springs with stiffness k_T and k_R, respectively. The model consists of more than 10,000 elements (at least 1000 elements along the radial direction and the element aspect ratios are close to 1). A convergence study was performed to ensure the results were independent of mesh density. A nonlinear solver was used.

In the FE simulations, Young's modulus of 5 GPa and a specimen radius of 10 mm were assumed. Shear effects, which are not included in the CPT and vKPT models, may scale with these parameters in forms other than the listed dimensionless parameters in equation (3.1). Since shear effects are included in the FE simulations, it is important to note

these assumed parameters. All other dimensions used in the FE simulations can be calculated from the listed dimensionless parameters as they appear.

3.3.3 Discussion

3.3.3.1 Range of applicability of the models

Figure 3-2(a) shows the center deflection as a function of applied pressure for the three different models assuming a perfectly clamped edge. The CPT begins to deviate from the nonlinear models at transverse displacements of less than a quarter of the specimen thickness, $\widetilde{w}(0) \geq 0.25\tilde{h}$. At large applied pressure, the stretching resistance in the nonlinear models causes the transverse displacements to be smaller than that in the classical plate theory. The vKPT agrees well with the FE model for thin specimens $\tilde{h} < 0.01$. As the specimen thickness increases, shear deformations become more important and the transverse displacement in the FE model is larger than vKPT. For specimen thicknesses $\tilde{h} > 0.1$, the FE model (or a shear corrected plate theory such as [100]) should be used for the experiment analysis.

For the pinned edge case (Figure 3-2(b)), the deviation of CPT begins at $\widetilde{w}(0) \geq 0.05\tilde{h}$. The difference between the three different thicknesses are smaller for the FE model, indicating the effect of shear deformations are smaller in the case of a pinned edge. The effect of compliant boundary condition will be discussed in detail below.

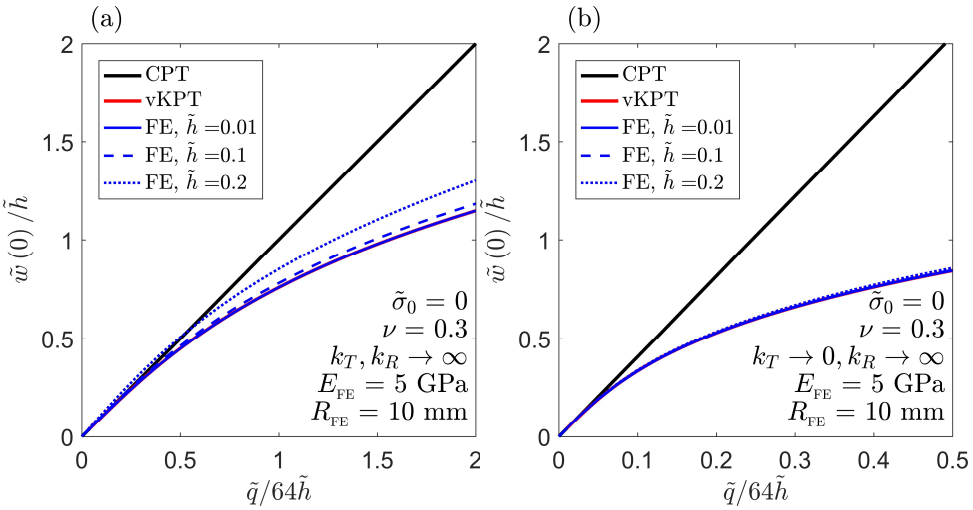

Figure 3-2: Center deflection as a function of applied pressure for CPT, vKPT and FE with a (a) clamped edge and (b) pinned edge. Dimensional parameters are used in the FE model.

3.3.3.2 Effects of pre-stress

For thin and flexible specimens, ensuring that the specimen is initially flat can be challenging. One way to achieve this is to pre-stretch the specimen prior to clamping it onto the BCT mount. This introduces a pre-stress that must be accounted for. The presence of pre-stress effectively stiffens the specimen. Figure 3-3 shows the center deflection as a function of applied pressure for three different pre-stress values ($\tilde{\sigma}_0 = 0, 2, 5$). As the pre-stress value increases, the center deflection decreases. Moreover, the CPT solution is applicable for a larger applied pressure at larger pre-stress values.

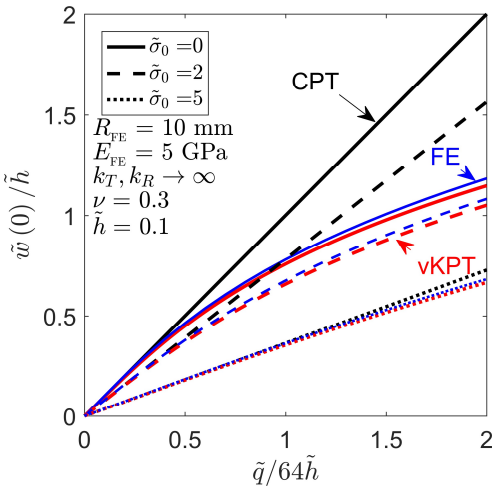

Figure 3-3: Center deflection as a function of applied pressure for CPT, vKPT and FE (black, red and blue colors respectively) with a clamped edge.

An advantage to having pre-stress in the specimen is that the deflection response is effectively linearized. This allows the CPT solution, instead of the more complicated vKPT solution, to be used even when the specimen geometry suggests nonlinear coupled deformation in absence of pre-stress. Figure 3-4 shows the maximum applied pressure, $\tilde{q}$, in which the FE model is within 5% of the CPT solution at a given $\tilde{\sigma}_0$. The CPT solution is applicable for any applied pressures that are smaller than the reported $\tilde{q}$. As the pre-stress increases, a larger maximum applied pressure is also allowed for the CPT solution. The sharp transition near $\tilde{\sigma}_0 \approx 1$ is due to the suppression of membrane effects that becomes important when $\tilde{q}/64\tilde{h} \geq 0.5$. The results are consistent with those obtained in [95] that compare the vKPT model with the CPT solution. In addition, the FE model also showed that the maximum applied pressure is larger when the thickness of the specimen is larger. This shows that shear stresses have a compounding effect on the BT and the BCT.

Therefore, it may be best to avoid designing specimen geometries that can have significant shear deformation unless analysis is to be done with an FE simulation that captures shear deformation.

In the range where the CPT is applicable, the center deflection for the clamped edge case is:

$$\tilde{w}(0) = \frac{2 - 2I_0\left(\sqrt{\tilde{\sigma}_0}\right) + \sqrt{\tilde{\sigma}_0} I_1\left(\sqrt{\tilde{\sigma}_0}\right)}{4\tilde{\sigma}_0^{3/2} I_1\left(\sqrt{\tilde{\sigma}_0}\right)} \tilde{q} \tag{3.12}$$

This is the same result as that reported in [95]. In the limit where $\tilde{\sigma}_0$ is very small, the equation reduces to a more commonly known form: $\tilde{w}(0) = \tilde{q}/64$ (which is plotted in Figure 3-2).

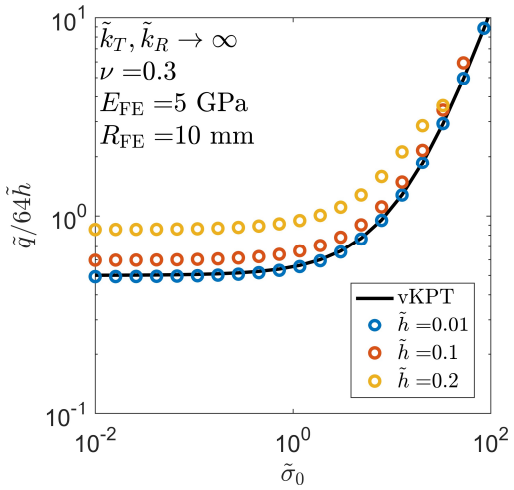

Figure 3-4: Critical applied pressure as a function of pre-stress for three different thicknesses. CPT is applicable for of the combinations of pre-stress and applied pressures below the lines.

3.3.3.3 Effects of compliant boundary condition

Slipping at the edge is usually prevented by permanently bonding the specimen to the mount, so typically $k_R \to \infty$. However, when specimens are thick, rotation at the edge may not be avoided easily, as excess clamping can also cause complex stresses at the edge. The effects of edge rotation due to compliant boundary conditions on the center displacement is investigated in Figure 3-5. As the torsion spring stiffness increases, the center displacement is significantly reduced. For the CPT solution, the ratio between a pinned edge ($k_T \to 0$) and clamped edge ($k_R, k_T \to \infty$) is $(1+\nu)/(5+\nu)$. There is a significant difference between the CPT and FE solutions at the pinned edge limit. The bending moment at the clamped edge increases the total bending energy contribution compared to the stretching energy contribution. Without the bending moment in the pinned edge case, the transition from bending dominated (CPT) to coupled bending and stretching (vKPT) is much sooner than the clamped edge case. This is also seen in Figure 3-2, where the deflection responses are quite different for the two edge conditions. In general, the specimen is considered to be perfectly clamped when $\tilde{k}_T \geq 10$ and pinned when $\tilde{k}_T \leq 0.1$. Other values of applied pressures do not change the $\tilde{k}_T$ values that define the transition. Other values of $\tilde{h}$ do not change the transition due to $\tilde{k}_T$ either.

The influence of compliance at the edge can be as much as three times different. Therefore, it is important to identify the correct boundary condition so that the appropriate mechanics model can be applied. The advantage of choosing a BCT geometry is that the BT can serve as a calibration to extract the compliant boundary conditions. Using the

displacements measured during the BT stage, the boundary conditions can be characterized without the influence of adhesion.

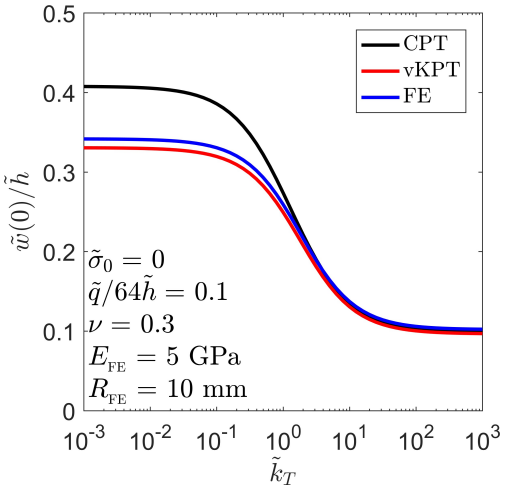

Figure 3-5: Center deflection as a function of torsion spring constant for three different pressures.

3.3.3.4 Typical displacement data

Experimental techniques used to extract mechanical properties from the bulge test typically measure the displacement of the specimen as a function of the applied pressure. The transverse displacement can be measured via optical profiling, which can be done via direct observation from the side, apply interferometry or implement 3D digital image correlation [89]. Another method is to measure the curvature of the deformed specimen via moiré deflectometry [29]. Alternatively, the in-plane displacements can be measured via 2D digital image correlation. Random markers may be placed on the surface of the specimen and a telecentric lens and camera is used to track the in-plane displacements during the test.

Depending on the situation of the experiment one of these methods may be used to obtain the displacement field.

Figure 3-6 and Figure 3-7 show the radial displacement, $\tilde{u}(\tilde{r})$, and transverse displacement $\tilde{w}(\tilde{r})$ as functions of radial position, $\tilde{r}$, for different values of $\tilde{h}$ and $\tilde{k}_T$. In these cases of $\tilde{h}$ and $\tilde{k}_T$, the differences between the vKPT and FE solutions are generally less than 10%, so the either model is suitable for the ranges of thicknesses and torsion spring stiffness chosen. A thinner specimen changes the radial displacement much more than the transverse displacement due to larger in-plane deformation caused by membrane stresses. The transition from clamped edge ($\tilde{k}_T \to \infty$) to pinned edge ($\tilde{k}_T \to 0$) is apparent near the edge for both transverse and radial displacements. Overall, the radial displacements are more sensitive to thickness and boundary condition but the range of radial displacement is smaller (in either cases, the range of radial displacements is less than $0.15\tilde{h}$ whereas the range of transverse displacements is around $1.5\tilde{h}$).

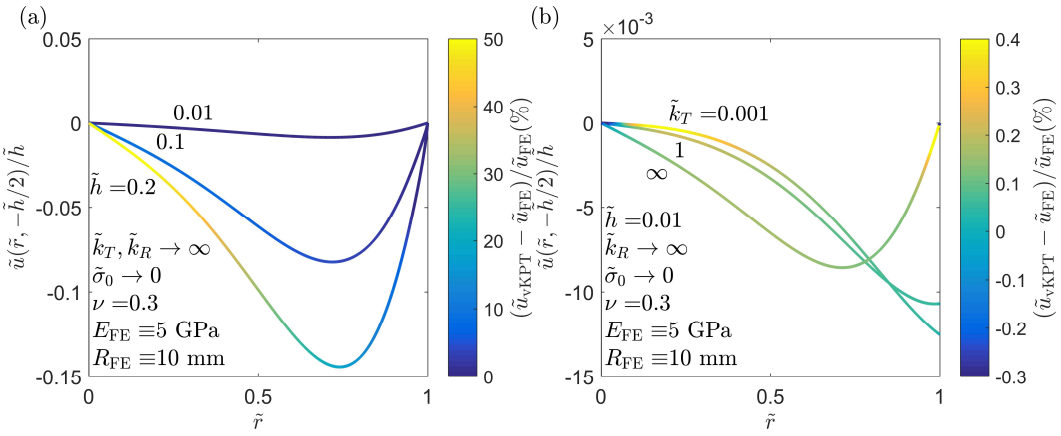

Figure 3-6: Radial displacement as a function of radial position for different values of (a) thickness and (b) torsion spring constant. The color on the lines show the differences between the vKPT solution and FE solution.

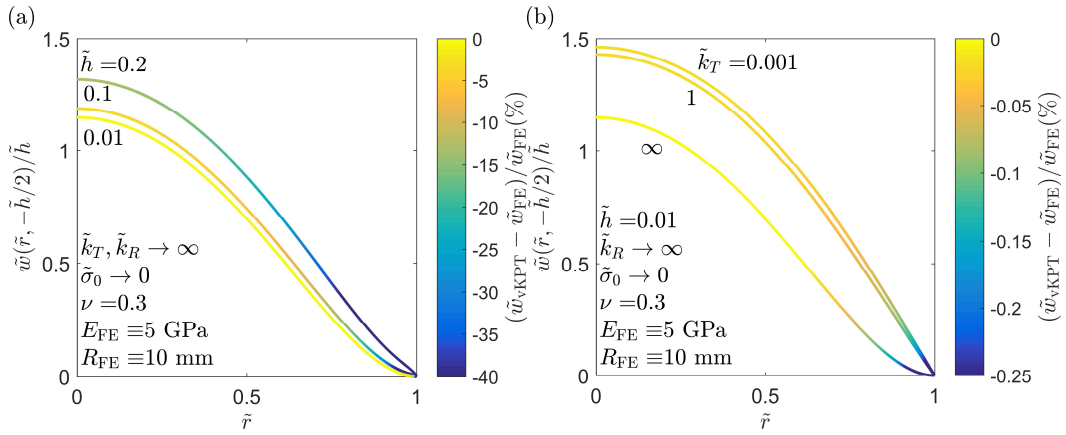

Figure 3-7: Transverse displacement as a function of radial position for different values of (a) thickness and (b) torsion spring constant. The color on the lines show the differences between the vKPT solution and FE solution.

Each of the measurement techniques discussed above has its own merits, so understanding the typical deformation response helps in choosing the best method for the BCT. For instance, 2D digital image correlation is very simple to implement but the radial displacements are small so the resolution is comparatively lower. On the other hand, interferometry has high resolution in transverse displacement measurements, but may be expensive to implement.

3.4 Blister contact test

3.4.1 Boundary conditions

The boundary conditions for the BCT are similar to those listed in the BT. The boundary conditions at the outer edge of the specimen, $\tilde{r} = 1$, (3.9)-(3.11) are used in conjunction with boundary conditions at the contact edge, $\tilde{r} = \tilde{b}$:

$$\widetilde{w} = \tilde{\delta} \tag{3.13}$$

$$\widetilde{w}' = 0 \tag{3.14}$$

$$\tilde{u} = \tilde{b}\tilde{u}' \tag{3.15}$$

An assumption of frictionless contact leads to the boundary condition in equation (3.15). In addition to the three boundary conditions, a fourth boundary condition, depending on the adhesion model, is needed to solve for $\tilde{b}$ at a given $\tilde{q}$.

3.4.2 Adhesion models

3.4.2.1 Hertz-type contact

For the Hertz-type model, there is no adhesion at the edge of the contact. This means that there is no external moment acting on the edge of contact, $\tilde{r} = \tilde{b}$:

$$\widetilde{w}'' + \frac{\nu\widetilde{w}'}{\tilde{b}} = 0 \rightarrow \widetilde{w}'' = 0 \tag{3.16}$$

In the absence of pre-stress, $\tilde{\sigma}_0 \to 0$, the relation between contact radius, $\tilde{b}$, and applied pressure, $\tilde{q}$, for a specimen with a clamped edge ($k_T, k_R \to \infty$) using the CPT is:

$$\tilde{q} = \frac{64\tilde{\delta}\left(\tilde{b}^2 - 1 - 2\log\tilde{b}\right)}{\left(\tilde{b}^2 - 3\right)\left(\tilde{b}^2 - 1\right)^2 - 2\log\tilde{b}\left(1 + 2\tilde{b}^2 - 3\tilde{b}^4 + 4\tilde{b}^4\log\tilde{b}\right)} \tag{3.17}$$

Closed-form analytical expressions can also be obtained for non-zero $\tilde{\sigma}_0$ and $\tilde{k}_T$, but they are rather lengthy, so they are not shown here.

3.4.2.2 Dugdale-type adhesion

Adhesion is the change in energy due to new surface creation. This energy is commonly approximately using the Lennard-Jones potential [36]. In the Lennard-Jones potential, the adhesive traction is a function of the separation gap between the two surfaces. Another way to represent adhesion is to adopt a Dugdale-type adhesion law. In the Dugdale-type adhesion model, a constant adhesion stress, σ_{adh}, acts over a specified adhesion range, δ_{adh}, as

$$\tilde{\sigma}_{\text{adh}}(\tilde{r}) = H\left[\widetilde{w}(\tilde{r}) - \tilde{\delta} + \tilde{\delta}_{\text{adh}}\right]\tilde{\sigma}_{\text{adh}}, \tag{3.18}$$

where $H[\xi]$ is the Heaviside function of ξ. The strain energy release rate G is the product of the adhesion stress and range, i.e. $\tilde{G} = \tilde{\sigma}_{\text{adh}}\tilde{\delta}_{\text{adh}}$. At the interface $\tilde{r} = \tilde{b} + \tilde{b}_{\text{adh}}$ there is a jump in applied stress, but the displacements and their derivatives must remain continuous, e.g., $\widetilde{w}\left(\tilde{b} + \tilde{b}_{adh}^{-}\right) = \widetilde{w}(\tilde{b} + \tilde{b}_{adh}^{+})$ and so on. Boundary condition equation (3.16) is used at

the contact edge. This problem can also be solved with the `bvp4c` function in MATLAB as a multipoint boundary value problem.

3.4.2.3 JKR-type adhesion

For materials that are soft or have large adhesion stress, the adhesive traction range can be small compared to other geometric quantities. In this case, it is appropriate to take the limit $\tilde{\delta}_{\text{adh}} \to 0$ in the Dugdale-type adhesion model. This limit is also known as the JKR-type adhesion model. The JKR-type adhesion model is analogous to the JKR theory for spheres [44]. In this model, the adhesion can be modeled as a moment that acts along the contact edge. According to the moment discontinuity method, this adhesive moment is directly related to the strain energy release rate, G, [101] and the fourth boundary condition at $\tilde{r} = \tilde{b}$ is:

$$\widetilde{w}'' + \frac{\nu \widetilde{w}'}{\tilde{b}} = \widetilde{M}_{\text{adh}} = \sqrt{2\tilde{G}} \tag{3.19}$$

The Dugdale and moment methods of solution described here are also equivalent to the energy balance approach used in [32].

3.4.3 Finite element simulation

3.4.3.1 Dugdale-type adhesion

For a Dugdale-type adhesion, the adhesion stress, σ_{adh}, is applied using the user subroutine `UTRACLOAD`. In addition to the model described in section 3.3.2, an analytical rigid surface

is created at the fixed gap δ above the top surface of the specimen. Using the user subroutine, when the top surface is within the adhesion range δ_{adh} a tensile adhesion stress σ_{adh} is applied to the top surface. Frictionless contact is assumed at the interface between the top surface of the specimen and the analytical rigid surface.

3.4.3.2 JKR-type adhesion

For JKR-type adhesion, the virtual crack closure technique (VCCT) [102] is used to calculate the strain energy release rates without using a user subroutine. In addition to the method outlined in section 3.3.2, the top-surface nodes that are within the contact radius are constrained to displace transversely by δ. The radial displacements of these nodes are not constrained to be consistent with the frictionless assumption. The reaction forces and the displacements near the crack opening are then used to calculate the strain energy release rate via the VCCT.

3.5 Results and discussion

The BCT is a hybrid load and displacement-controlled test. Typically, the applied pressure is controlled during the test but the rigid surface restricts the maximum transverse displacement of the specimen. The deformation mechanisms are not intuitive to identify as there are four geometrical parameters (b, δ, h and R) and three "load" parameters (q, G and σ_0). However, comparing the three mechanics models reveal some interesting results about the deformation mechanisms. Figure 3-8(a) compares the strain energy release rates,

G, between CPT and FE solutions as functions of geometries $\tilde{\delta}$ and $\tilde{h}$. The map is divided into three different regions each representing a type of deformation mechanism. In the region where the CPT agrees within 5% of the FE solution, the specimen deformation is dominated by bending stress. When $\tilde{h}$ is large, shear stress is important and the CPT solution is not applicable. On the other hand, as $\tilde{h}$ decreases or $\tilde{\delta}$ increases, membrane stress becomes more important and the CPT solution deviates from the FE solution. Figure 3-8(b) shows the comparison between vKPT and FE solutions. The contrast between the two figures show the contribution from membrane stress. As the vKPT solution is applicable for a wider range of $\tilde{\delta}$ and $\tilde{h}$, the vKPT model is preferred for the BCT.

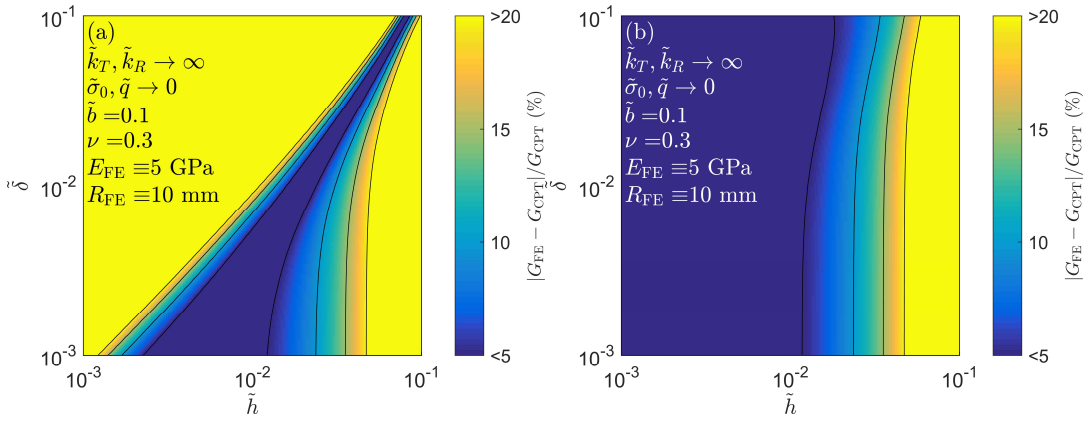

Figure 3-8: Map of the difference between the JKR-type adhesion FE solution and (a) the CPT solution, (b) the vKPT solution.

As discussed in the BT case, accounting for pre-stress is important in some cases of BCT specimens. Since pre-stress effectively increases the stiffness of the specimen, a larger applied pressure is needed to achieve the same contact size in the BCT. Determining the range of pre-stress in which it needs to be accounted for in the BCT can help understand

the limit in which simplification can be made. To do so, the vKPT solution with and without pre-stress are compared against each other for a Hertz-type contact. Figure 3-9 shows a contour plot of the cut-off value for pre-stress that deviates from the solution without pre-stress. This value suggests whether a measured pre-stress needs to be included in the BCT analyses or not. For example, if $\tilde{\delta}$ is 0.05 then $\tilde{\sigma}_0$ must be accounted for if it is greater than 10. For larger gaps this maximum allowable pre-stress is reduced.

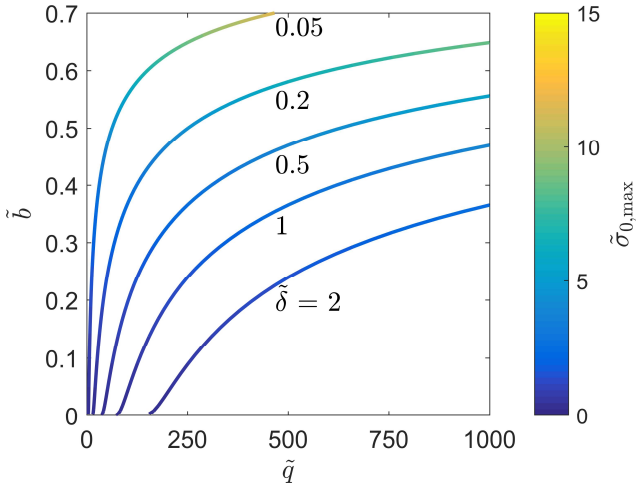

Figure 3-9: Map of pre-stress value that deviates from the classical plate theory solution without pre-stress by 5%. Numbers on line represent the constant gap $\tilde{\delta}$ for each line.

Figure 3-10 shows a contour plot of strain energy release rates as functions of contact radius and applied pressure using the vKPT model with JKR-type adhesion. For a blister contact test in equilibrium, the measured contact radius follows the constant strain energy release rate line as the applied pressure increases. The $\tilde{G} = 0$ line corresponds to a Hertz-type contact. For $\tilde{G} > 0$, there are two contact radii at the same $\tilde{G}$ and $\tilde{q}$. The smaller value is unstable (marked as dashed lines) as $\tilde{q}$ must decrease while $\tilde{b}$ increases. As a result,

the specimen jumps into contact when the pressure is large enough to push it into contact. Conversely, the specimen will jump out of contact once the pressure is at the minimum value on the fixed strain energy release rate curve.

As shown in Figure 3-10, it is possible that in order for a specimen to detach a negative applied pressure is needed. One way to avoid such scenario is to increase the gap $\tilde{\delta}$. Simulating the BCT using typical or expected parameters prior to experiments is recommended.

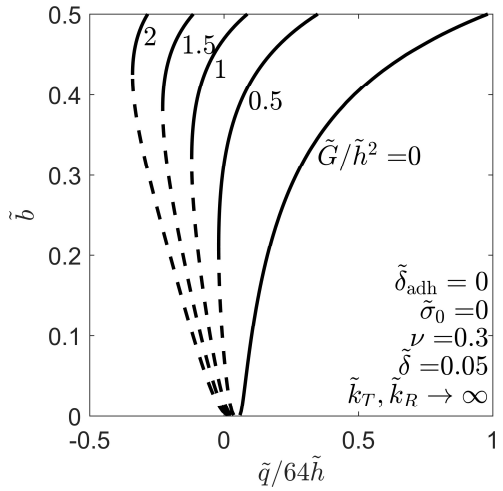

Figure 3-10: Typical contact radius response as a function of applied pressure calculated using vKPT. The dashed lines represent unstable contact.

Figure 3-11 shows the contact radius curves for different adhesion ranges and fixed adhesion. In the JKR-type adhesion ($\tilde{\delta}_{\mathrm{adh}} = 0$), the specimen jumps into and out of contact. As the adhesion range increases, the specimen jumps into contact but at a smaller contact radius; eventually the jump vanishes for a large adhesion range. At the limit where the

adhesion range is equal to the fixed gap, the specimen does not jump into contact at all. Thus, in addition to the change in contact radius shape, the initial contact radius (or last contact radius before the specimen detaches) also changes depending on the adhesion range. This may be leveraged in BCT experiments to extract the adhesion range between two surfaces.

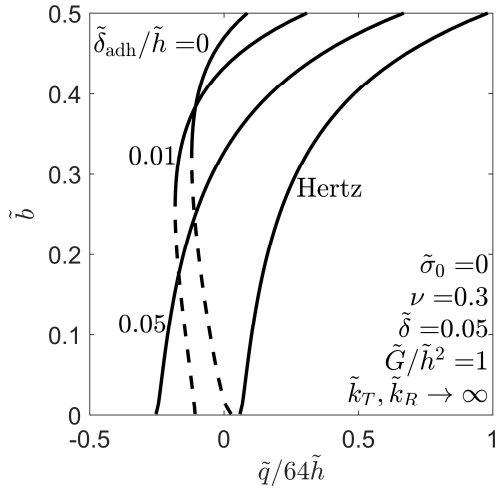

Figure 3-11: Contact radius as a function of applied pressure for different adhesion ranges calculated using the vKPT model. The Hertz-type contact case is also shown in the plot.

3.6 Summary

The mechanics of BCT is investigated in this work. The BCT can be used to characterize the adhesion between a thin and flat specimen and a flat substrate. The deformation mechanics of the specimen is studied using analytical models and finite element models. The ranges in which each deformation mechanism dominates (bending stress, shear stress and membrane stress) are identified. The effects of pre-stress and compliant boundary

conditions are also investigated. The deformation mechanics can be linearized and solved with a closed-form solution with sufficient pre-stress or low enough applied pressure. Compliance in the edge can lead to larger deformation and must be calibrated properly. The BT, which is the precursor to the BCT, is also studied using these models. The BT allows for calibration and characterization of mechanical properties of the specimen prior to and independent of the BCT.

With the results presented in this work, the following are some questions that should be addressed during the BCT design process: (1) For the typical test specimen geometry and mechanical properties, which analysis model is the most appropriate? (2) Is pre-stress going to be important and does the pre-stress simplify or complicate the analysis? (3) What kind of measurement technique, e.g. digital image correlation or interferometry, is the best to use to characterize adhesion in the BCT? (4) Which contact model is the most suitable for the BCT that is being considered? The answers to these questions are unique to each test specimen, so understanding the typical response of the BCT prior to implementing the experiments can help with choosing the best design for the set up.

CHAPTER 4: Characterization of rate-dependent adhesion of PDMS using the BCT

4.1 Background

4.1.1 Blister specimens for measuring adhesion

A number of experimental configurations based on circular pressurized membranes and plates have been investigated over the past several decades for the characterization of the fracture and adhesion properties of interfaces. These geometries are attractive as it is often easy to fabricate materials of interest as flat sheets or coatings on thicker substrates. In a simple blister test [65]–[69], a sheet or film is initially adhered to a substrate with a circular hole through which pressure is applied. The sheet deforms as a result of the applied pressure and if the pressure is sufficient, a crack propagates at the sheet-substrate interface. If the test is pressure controlled, unstable delamination will occur at a critical blister radius [64]. The instability can be avoided by using a volume-controlled test [65]. Alternatively, the instability can also be avoided through a use of a constrained blister test, where an adhesionless rigid surface is placed a small distance above the specimen to limit the maximum out-of-plane deflection [103]–[105]. While the blister and constrained blister tests have been widely used, these approaches only permit the characterization of separation and do not readily allow the formation of the adhesive contact to be characterized. The blister contact test (BCT) is distinct from these other blister tests because: (1) in the BCT, adhesion is measured between the membrane and a separate

reference surface rather than the surface the membrane is initially fabricated on; (2) as adhesive contact is first made during the test, the BCT provides the ability to characterize both the adhesion and separation behavior of the contact. The mechanics of the BCT specimen were studied in detail by [32] and has been used to characterize adhesion between a PET/Acrylate film and glass [28], [30]. Furthermore, stable adhesion and delamination is achieved over most of the contact range in the BCT even when pressure control is used [28].

4.2 Specimen mechanics

4.2.1 Finite element analysis

Finite element (FE) analysis was used to examine the BCT in cases in which classical plate theory was not valid. An axisymmetric model was developed in the ABAQUS commercial FE package [99]. In the model, the plate is meshed with 8-node axisymmetric continuum elements. The nodes along the outer radius are tied together to constrain translation and are connected to a torsion spring element to model the compliant boundary condition. The loading in the BCT is represented as a uniform pressure applied to the bottom surface of the plate. The nodes within the contact area are displaced by δ in the z-direction to model the contact with the reference surface. A nonlinear solver is used and the strain energy release rate is calculated from the displacements and the forces at the crack tip using the virtual crack closure technique [102]. Results of the VCCT were also verified with a J-integral calculation.

The FE model was also used to analyze the specimen deformation prior to contact with the reference surface. As described in Chapter 3, this case is used during specimen calibration. The FE model for this case is the same as that described for the BCT, except the only load on the specimen is the applied pressure as contact with the references surface does not occur. The in-plane displacements on the bottom surface of the plate are extracted from this model for comparison with data measured in the calibration experiments.

4.2.2 Comparison between analytical and FE results

The analytical model presented in Chapter 3 only accounts for bending deformation in the BCT, thus it is important to understand the range of applicability of the model for analyzing experimental data. The specimen geometry (R, h, and b) and degree of deformation (determined by δ and q) determine the importance of non-bending effects, such as membrane stresses and transverse shear, that will lead to deviations from the analytical solution. In such cases, the analytical model (equation (3.5)) is insufficient for the analysis of experimental data and the FE model is used to analyze the data instead.

In comparing the analytical and FE models, results are presented for cases in which the specimen has a radius, R = 10 mm, and the elastic properties are E = 2.1 MPa and ν = 0.49. These dimensions and properties are representative of the PDMS specimens used in the experiments described in this paper.

Figure 4-1(a) compares the FE and analytical predictions of deflection at the center of the specimen prior to contact with the reference surface. This case is essentially a bulge

test [64], [65], [69]. Specifically, results are shown for a fixed pressure of 100 Pa and a range of torsional spring stiffnesses that varies the boundary condition from pinned to clamped in Figure 4-1(a) at small deflections to demonstrate agreement between the FE and analytical models. While the overall agreement appears good, the FE predicted displacements are larger than the classical plate theory solution for most cases shown. It is evident that the shear deformation is important for thick specimens. For the h = 1.6 mm case, inclusion of the shear correction in the above equation leads to a 16% difference in center deflection, whereas the discrepancy between the classical plate theory solution and FE model in Figure 4-1(a) is 11%.

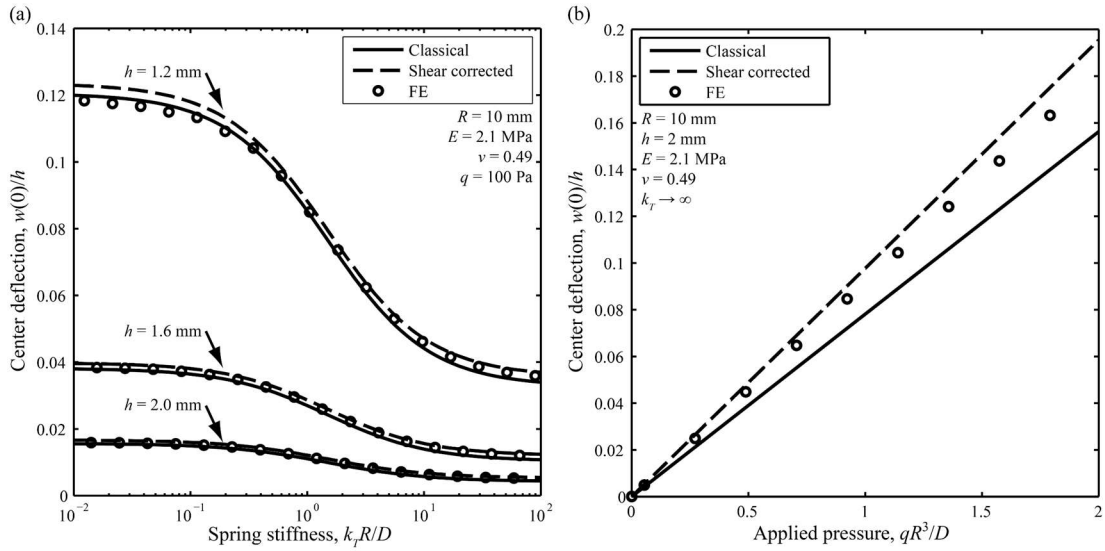

Figure 4-1: (a) Center deflection as a function of spring stiffness for a bulge test, results shown for a constant pressure of 100 Pa; (b) Center deflection as a function of applied pressure for a bulge test with a clamped edge.

For the thinnest specimen (h = 1.2 mm) and lower spring stiffness values in Figure 4-1(a), the analytical solution overestimates the center deflection. Begley and Mackin [106]

derived a dimensionless parameter $\lambda = \pi\tilde{q}\sqrt{12(1-\nu^2)}/\tilde{h}$ for the bulge test to determine the transition from plate to membrane behavior. When λ is less than 300 for clamped and 40 for simply supported circular plates, the membrane effects are expected to be negligible. For the thinnest specimen, h = 1.2 mm, in Figure 4-1(a), λ = 20, thus membrane effects are not expected to play a significant role, but still may be responsible for the slight under prediction by the analytical model. In the calibration experiments described later, the pressures are considerably larger (up to 4 kPa) on a specimen that is 2 mm thick, leading to λ = 103. Thus, membranes stresses will develop and effectively stiffen the membrane as shown in Figure 4-1(b). It is evident that both shear deformation and membrane effects can play meaningful roles in the deflection of the specimen prior to contact, thus the data obtained in the calibration tests in this work are analyzed with the FE model.

Once the specimen is pressurized into contact with the reference surface, the strain energy release rate at the edge of the contact is the primary quantity of interest. The percent difference between the strain energy release rates calculated from the FE and analytical models is summarized in Figure 4-10 as a function of the reference surface separation and specimen thickness for $\tilde{b} = 0.05, 0.2, 0.4$ and 0.6, $q = 0$, and $k_T \to \infty$. The region in which the bending solution agrees with the FE model to within ±5% is a function of the specimen thickness, $\tilde{h}$, the separation between the specimen and reference surface, $\tilde{\delta}$, and the contact radius, $\tilde{b}$. At large $\tilde{\delta}$ and small $\tilde{h}$, membrane effects dominate and use of the bending solution would produce large errors as shown in Figure 4-2. At $\tilde{\delta} = 100\tilde{h}$ and $\tilde{b} = 0.4$, the

membrane solution given by Xu and Liechti [28], which neglects bending stresses, is within 8% of our FE calculations. At large values of $\tilde{h}$ (i.e., the right-hand side of the plots in Figure 4-2), shear deformation in the specimen is significant and leads to deviations from the bending solution. Finally, note that the size of the region in which the bending solution is valid also depends on contact radius, $\tilde{b}$. Large contact radii reduce the size of the region in which the bending solution is valid because of larger shear effects in the region of the specimen that is not in contact. At small contact radii (e.g., $\tilde{b} = 0.05$), there is deformation in the contact region, similar to root rotation effects in the double cantilever beam specimen [59]. We note that Figure 4-2 could be used to select specimen condition for which equation (3.5) could be used to calculate G_c.

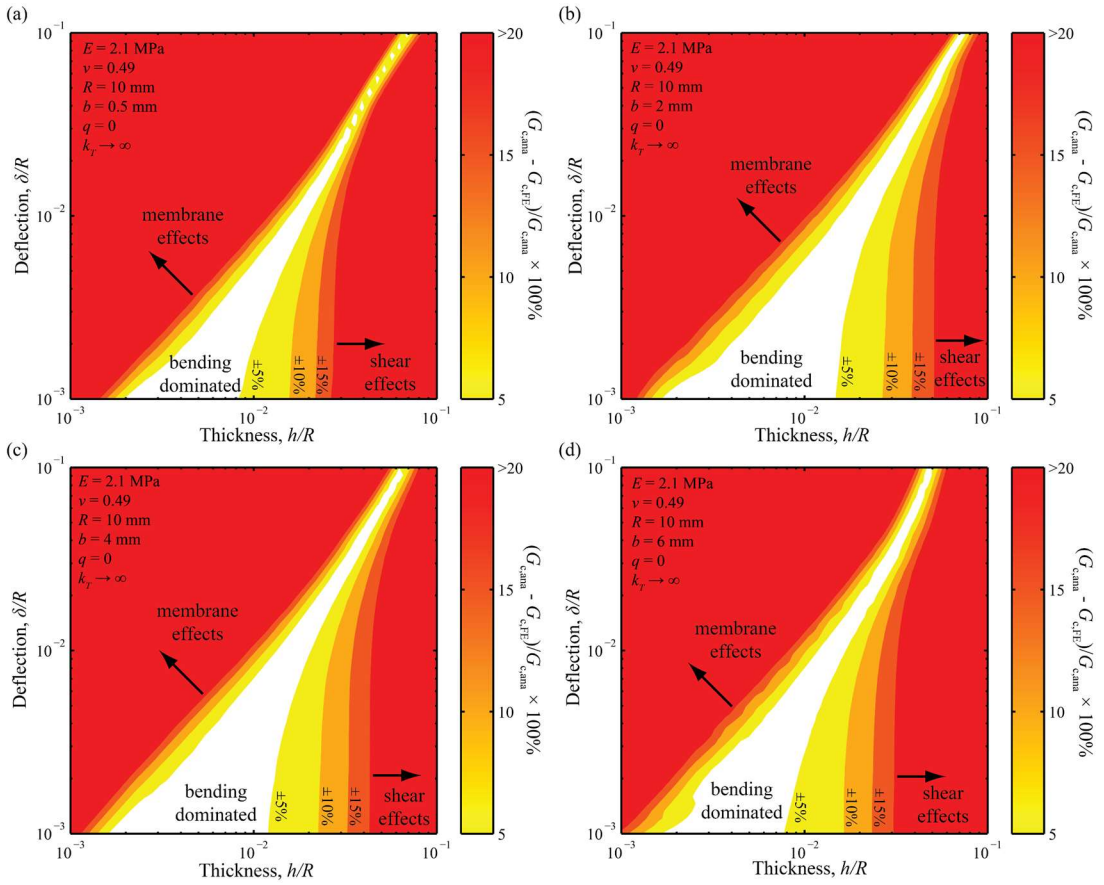

Figure 4-2: Percent difference between analytical solution, $G_{c,ana}$, and FE calculation, $G_{c,FE}$, of strain energy release rate as a function of deflection and thickness for the clamped edge blister contact test in the absence of applied pressure.

The specimens in the present study have $\tilde{\delta} = 0.05$ and $\tilde{h} = 0.21$. From the results in Figure 4-2, it is clear that G_c cannot be calculated from the experiments using the simple bending analysis (equation (3.5)). Thus, FE analysis is used to calculate G_c from the measured contact radius and pressure in all experiments. A straightforward analytical solution that captures the relevant mechanics is simply not available. Figure 4-3 shows the strain energy release rate as a function of applied pressure and contact radius for a typical specimen used in this study. The line for $G_c = 0$ represents adhesionless contact (i.e.,

assumptions similar to the Hertz analysis for spheres) and gives the minimum value of b at a given q. Also, note that at points that fall below the unstable boundary (indicated as a dashed line in Figure 4-3), the specimen will pull-off unstably from the reference surface if the adhesion is uniform across the contact.

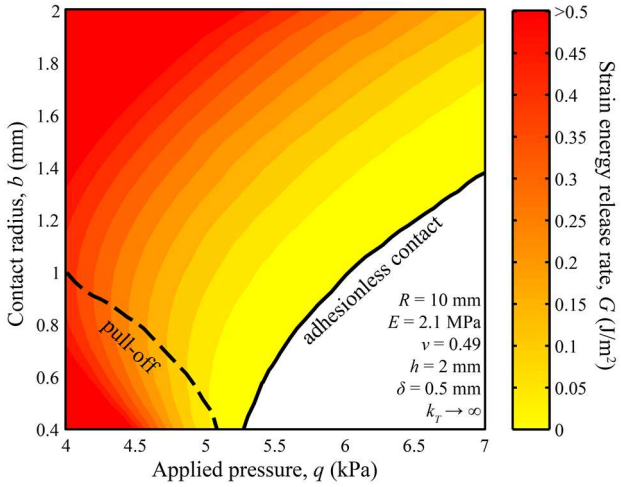

Figure 4-3: Critical strain energy release rate as a function of contact radius and applied pressure calculated using the FE model. Values are shown for specimen dimensions and elastic properties similar to those used in experiments.

4.3 Experimental approach

4.3.1 Specimen preparation and apparatus

The PDMS specimens were prepared from a Dow Corning (Midland, MI) Sylgard 184 elastomer kit. A 10:1 ratio of base and curing agent were mixed and degassed in a vacuum chamber until all gas bubbles were eliminated. The PDMS was molded between two smooth silicon wafers with metal balls used as spacers to define the specimen thickness;

specimens with nominal thickness of 2 mm were prepared. The specimens were cured at 85°C and atmospheric pressure for 4 hours on a hot plate.

Figure 4-4 shows a schematic of the test setup. The PDMS specimen was clamped between two flat precision steel washers. A 1 mm thick glass slide was used as a reference surface and was placed a small distance, δ, from the top surface of the specimen. The separation gap is set by the thickness of the washer between the specimen and reference surface. The cavity formed between the specimen and glass plate was vented to ensure no pressure build-up between the glass and specimen. A uniform white LED light source (Edmund Optics, Barrington, NJ) was used to illuminate the specimen. A camera (PixeLINK B741 1.3M pixels, Ottawa, ON) with a telecentric lens (Navitar 0.25X, Rochester, NY) was used to image the membrane and contact. The specimen was pressurized with nitrogen. Pressure was controlled by an electronic regulator (Parker Porter 415, Hatfield, PA) and independently measured using a commercial pressure sensor (Honeywell 24PC 0-5 psi differential, Golden Valley, MN). A computer was used to control the regulator and record pressure measurements and images from the camera.

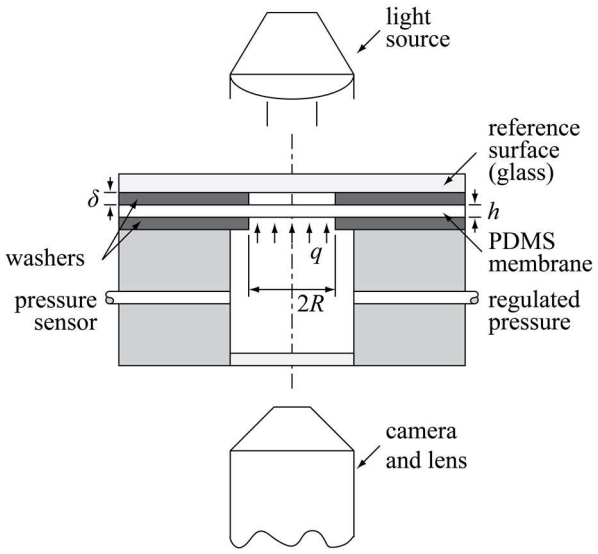

Figure 4-4: Schematic of experimental apparatus.

4.3.2 Specimen calibration

To determine the appropriate boundary conditions and elastic properties of the specimens, the in-plane displacement field on the bottom surface of the specimen was measured as a function of applied pressure using digital image correlation (DIC) [107], [108]. While 3-D displacements can be measured with DIC, a simple single-camera system that only allows in-plane displacements to be measured was used in this study. This is suitable because the out-of-plane displacement of the specimen is limited. A random pattern of markers was created on the bottom surface of the PDMS specimen by using black spray paint. The paint layer is substantially thinner than the specimen and is discontinuous, thus the spray paint has a negligible effect on the mechanical response of the specimen. Images of the entire specimen were recorded as the applied pressure on the specimen was increased to a maximum pressure of 4 kPa in increments of 1 kPa and then decreased. The image

sequence was subsequently analyzed using a freely available DIC script for MATLAB [109] to obtain full-field in-plane displacements across the specimen. A nonlinear least square optimization algorithm was used to determine the Young's modulus, E, and torsion spring stiffness, k_T, that allows for the best agreement between the measured in-plane displacements and the displacements predicted by the FE model.

Figure 4-5 shows an example of an in-plane displacement field measured on the bottom surface of a specimen during a calibration test. The displacements are clearly axisymmetric, as expected. Also, note that the displacements are not zero at the specimen boundary, demonstrating that the edge of the specimen is not perfectly clamped. The in-plane displacements at the edge are due to rotation of the specimen edge about the midplane of the specimen. DIC measurements on the top and bottom surface of select specimens showed that the displacements at the edge were nearly equal in magnitude and opposite in direction, indicating that the edge rotates, but does not slip in-plane. Figure 4-6 shows the measured displacements at multiple pressures as well as the FE calculated displacements for the same specimen that is shown in Figure 4-5. In Figure 4-6, the markers and error bars represent the measured radial displacements and the lines represent the FE predicted displacements using the E and k_T determined through fitting the FE model to the experimental data. The FE displacements agree well with the measured values, suggesting that the boundary conditions in the FE model are correct. Calibration experiments were performed on all specimens to determine E and k_T for each specimen. Table 6-1 summarizes the E and k_T determined for each specimen. The mean Young's modulus

extracted from all specimens is 2.24 MPa, which is consistent with literature values of PDMS [10], [14]. The magnitudes of the extracted k_T values suggest the boundary condition at the specimen edge is closer to clamped than pinned, which is what is expected given the experimental configuration.

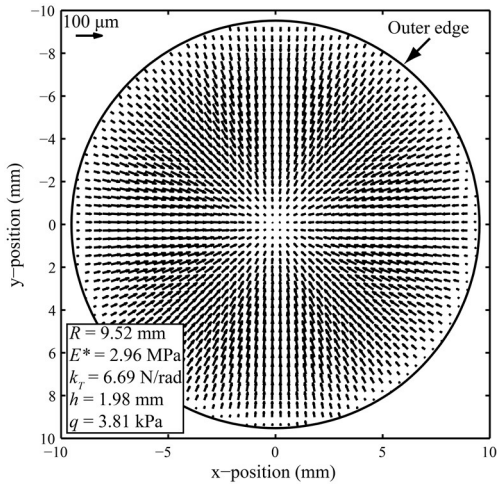

Figure 4-5: Vector map of measured displacements on the bottom surface of specimen 2 during a bulge test. The arrows show the direction of displacement and their lengths are the relative magnitudes of the displacements. The outer radius of the specimen is also shown in the figure.

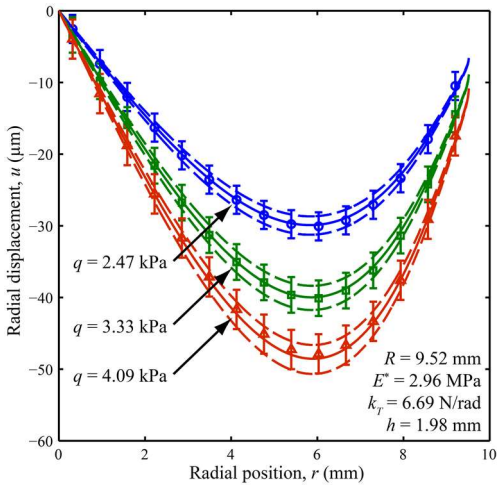

Figure 4-6: Radial displacements measured on a bulge test of specimen 2 at different pressures. The markers represent the DIC results fitted with a fourth order polynomial ($R^2 > 0.95$) and the error bars indicate the 95% prediction bounds of the fit. The solid lines are the FE results with E and k_T fit to the DIC results. The dashed lines are the FE results using the fit k_T and ±5% of the fit E.

Table 4-1: Properties of specimens determined using the bulge test. The gap δ is calculated using the pressure just before the specimen makes contact with the glass substrate. Poisson's ratio is assumed to be 0.49.

Experiment No.	Thickness h (mm)	Modulus E (MPa)	Stiffness k_T (N/rad)	Gap δ (mm)
1	1.98	2.04	3.37	0.46
2	1.98	2.25	6.69	0.46
3	1.98	2.28	6.11	0.47
4	1.98	2.38	4.58	0.44

4.3.3 Adhesion tests

Adhesive contacts between polymers often demonstrate rate-dependent behavior [14]. For example, the contact area can change even when the applied loading remains fixed over a period of time and the measured G_c is often a function of the contact or crack propagation

speed. Here, G_c is characterized during separation of the contact as the contact radius is decreasing ($db/dt < 0$) and during contact of the specimen and reference surface as the contact radius is increasing ($db/dt > 0$).

The BCT was performed by increasing the pressure to bring the PDMS specimen into contact with the glass reference surface, further increasing the pressure to cause the contact radius to grow, and then subsequently decreasing the pressure to separate the contact. The experiments were pressure controlled and the pressure was linearly varied between 0 and the maximum pressure (7 kPa) during each experiment. The loading/unloading rate was systematically changed such that the total loading/unloading time for the experiments ranged from 2 to 320 s. Images of the contact were acquired during the tests and contact radius was subsequently extracted from these images using an image analysis script in MATLAB. The strain energy release rate was calculated using the measured specimen properties, contact radius, and pressure using the FE model. Bond/crack velocity was calculated by numerically differentiating the measured contact radius with respect to time.

4.4 Results and discussions

4.4.1 PDMS-glass adhesion

Figure 4-7 shows the measured contact radius, b, versus pressure, q, for different loading and unloading rates. The data clearly shows adhesion hysteresis between loading and unloading, even in the slowest test. As the load/unload rate increases (or load/unload time

decreases), the gap between the load and unload curve widens and the hysteresis becomes more significant. The data in Figure 4-7 suggests that the strain energy release rate decreases as the loading rate increases. In unloading, strain energy release rate increases with increasing separation rate.

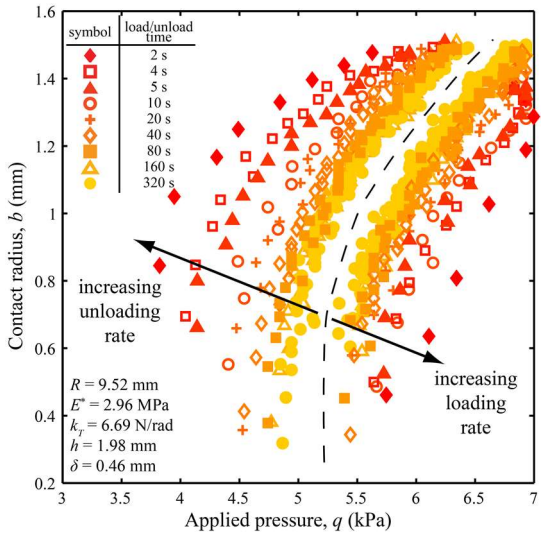

Figure 4-7: Experimental results for specimen 2 showing the effect of pressure rate on contact behavior. The dashed line is a visual aid to distinguish between loading and unloading parts of the data.

Figure 4-8(a) shows the FE calculated critical strain energy release rate, $G_{c,\mathrm{adv}}$, as a function of bond velocity, $\mathrm{d}b/\mathrm{d}t > 0$, for specimen 2. Since the BCT is pressure controlled, the bond (or crack) velocity is not constant in each test. By comparing all loading cases $G_{c,\mathrm{adv}}$ drops as bond velocity increases. At high bond velocity $G_{c,\mathrm{adv}}$ approaches zero corresponding to the adhesionless contact. This limit is not observed in contact separation, and equation (2.6) is unable to capture the limit at high bond velocity. Instead, equation (2.6) can be modified as:

$$G_{c,\mathrm{adv}} = G_{0,\mathrm{adv}}\left[1+\left(-\frac{\mathrm{d}b}{\mathrm{d}t}/v^*_{\mathrm{adv}}\right)^n\right]^{-1} \tag{4.1}$$

The model is bounded in high and low bond velocities, and the steady state strain energy release rate, $G_{0,\mathrm{adv}}$, and characteristic velocity, v^*_{adv}, have similar meaning to $G_{0,\mathrm{rec}}$ and v^*_{rec} for receding contact. It is unclear if the assumption of $n = 0.6$, used in receding contact analysis, is valid in advancing contact. As such, n is allowed to vary in the advancing contact model.

Figure 4-8(b) shows the collective results for three specimens and the fitted rate dependent model (equation (4.1)). The $G_{0,\mathrm{adv}}$ of 40.1 mJ/m^2 is similar to other experiments for PDMS/glass interface pair [65]. The experiment results are summarized in Table 4-2.

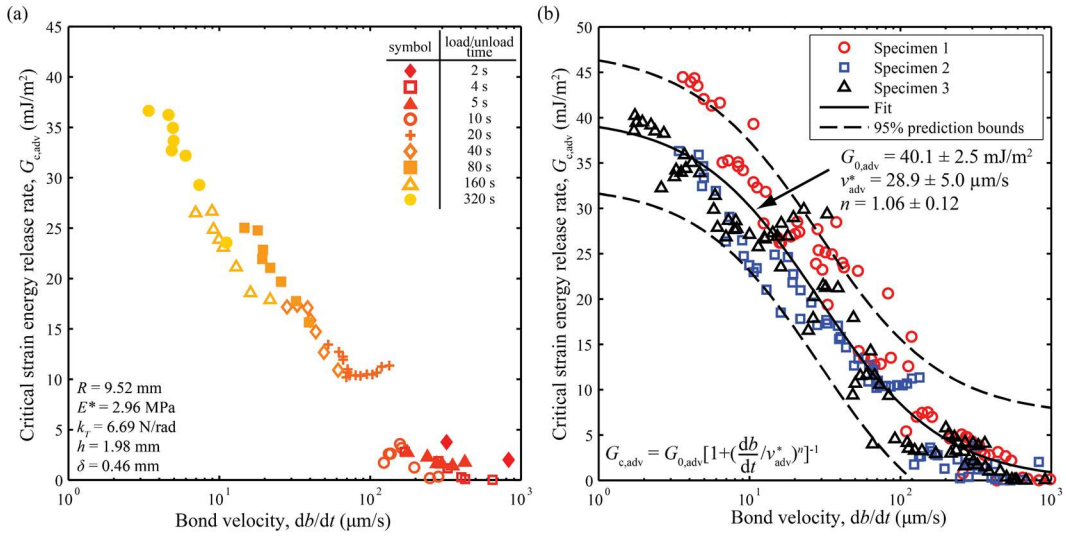

Figure 4-8: Measured critical strain energy release rate during bonding for (a) specimen 2; (b) specimens 1-3. The data is fitted with equation (4.1) ($R^2 = 0.90$) and the dashed lines are the 95% prediction bounds for the fit.

Figure 4-9(a) and (b) show the critical strain energy release rate during unloading ($\mathrm{d}b/\mathrm{d}t < 0$). The critical strain energy release rate, $G_{c,\mathrm{rec}}$, shows a distinct behavior from the loading data. The steady state strain energy release rate, $G_{0,\mathrm{rec}}$, is larger than that in advancing contact, $G_{0,\mathrm{adv}}$.

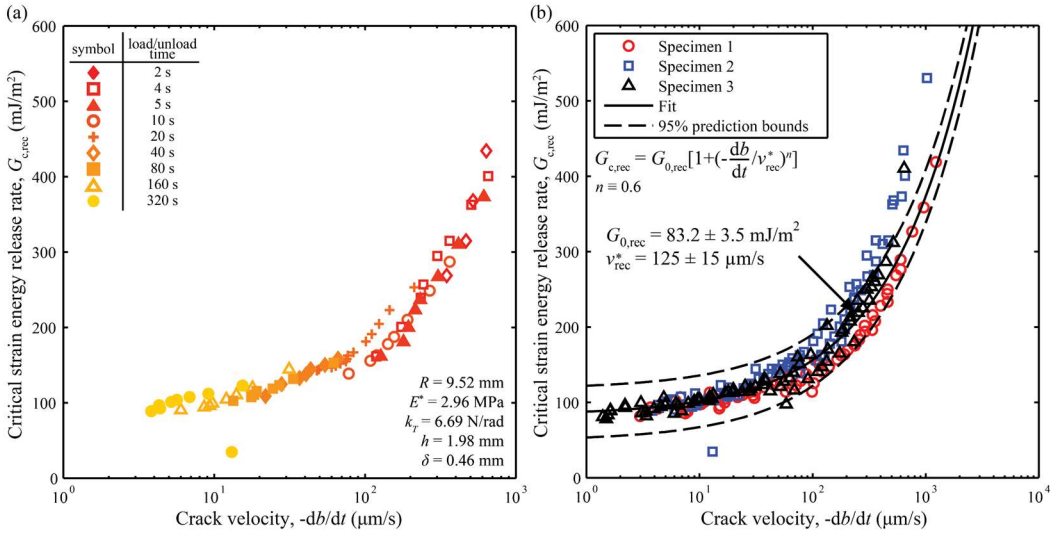

Figure 4-9: Measured critical strain energy release rate during separation for (a) specimen 2; (b) specimens 1-3. The data is fitted with equation (2.6) ($R^2 = 0.83$) and the dashed lines are the 95% prediction bounds for the fit.

The $G_{0,\mathrm{rec}}$ value of 83.2 mJ/m^2 is lower than that reported in [65] of 132 mJ/m^2, measured with a volume controlled blister test for PDMS-glass adhesion. In their experiments, they did not observe any rate-dependent effects for volumetric rates between 5 ml/hr and 25 ml/hr. However, we estimate $-\mathrm{d}b/\mathrm{d}t$ in their experiments to be around 200 μm/s. This would suggest $G_{c,\mathrm{rec}}$ is rate-dependent and closer to the reported values in [65]. The discrepancy in $G_{c,\mathrm{rec}}$ may also be due to the differences in PDMS formulation used, which can be indicated by the difference in measured Young's modulus.

The rate-dependent adhesion may be a result of the viscoelasticity of PDMS. In our study, PDMS is modeled as an elastic material in quasi-static loading and all rate-dependent effects are included in equations (2.6) and (4.1). In [49] a viscoelastic material in contact with a substrate would result in a similar rate-dependence as our empirical model, expect for large separation rates $\mathrm{d}h/\mathrm{d}t \ll 0$. The theoretical model shows a maximum $G_{c,\mathrm{rec}}$ at large separation rate, but we did not observe a maximum $G_{c,\mathrm{rec}}$ in our experiments. Furthermore, because the stress field near the contact edge is much larger than away from the contact edge, we expect the viscoelastic behavior to vary depending on the location in the PDMS. The far field stress, which is present due to applied pressure, is not accounted for in the theory, which may explain the discrepancy between the theory and experiments.

It is noted that $G_{0,\mathrm{rec}}$ is almost twice the value of $G_{0,\mathrm{adv}}$. This adhesion hysteresis may be due to the difference in mechanics for advancing and receding contacts. For advancing contact, air must be displaced for the contact to propagate [110]. The viscous dissipation to displace the air would lead to a lower $G_{c,\mathrm{adv}}$, as well as a rate-dependent response consistent with the experimental observation. For receding contact, surface roughness increases the effective contact area. The contact pressure allows the elastomer to make conformal contact with the substrate. With the increased effective contact area, $G_{c,\mathrm{rec}}$ is larger during separation [111]. Also, chemical rearrangement may occur in the interface between the elastomer and substrate [23]. Stronger bonds may form during contact which leads to higher $G_{c,\mathrm{rec}}$.

In these experiments the characteristic velocities v^* range from 28.9 to 125 μm/s, which are larger than the value reported in [51] but smaller than [9], [13]. In [51] the experimental crack velocity is less than 1 μm/s. In [9], [13] the experimental crack velocity ranges between 1 and 100 mm/s. In these experiment the range is from 1 to 1000 μm/s. The difference in range of the velocity measurements is possible to result in different v^* values. Also, the difference in chemical composition of PDMS and the curing conditions may affect the characteristic velocity.

Table 4-2: Summary of experimental results. Advancing contact data is fitted with equation (4.1) and the receding contact data is fitted with equation (2.6). The numbers inside the brackets are the 95% confidence bounds.

Exp. No.	Contact pair	Advancing contact			Receding contact	
		$G_{0,adv}$ (mJ/m^2)	v^*_{adv} (μm/s)	n	$G_{0,rec}$ (mJ/m^2)	v^*_{rec} (μm/s)
1-3	PDMS-Glass	40.1 <37.6, 42.6>	28.9 <23.9, 33.8>	1.06 <0.94, 1.18>	83.2 <79.6, 86.7>	125 <109, 140>
4	PDMS-PDMS	33.2 <32.2, 34.2>	36.8 <32.2, 40.5>	1.17 <1.07, 1.27>	88.0 <83.2, 92.8>	44.5 <39.2, 49.8>

4.4.2 PDMS-PDMS adhesion

As a further validation of the experiment, a glass slide coated with a PDMS layer of less than 10 μm was used such that the PDMS specimen comes into contact with a PDMS surface. As it is a thin layer of PDMS, the glass substrate still makes the surface effectively rigid. The loading and unloading results are shown in Figure 4-10(a) and (b) respectively. The results are similar to the PDMS-glass adhesion experiments. For advancing contact, we obtain a $G_{0,adv}$ of 33.2 mJ/m^2. This value is similar to the literature reported value of around 42 mJ/m^2 [14], [23], [56]. For receding contact, we measure a $G_{0,rec}$ of 88.0 mJ/m^2,

which is lower than the results obtained by Deruelle et al. [23] of around 125 mJ/m^2. This may be due to the differences in the composition and curing conditions of PDMS. The characteristic velocities for advancing and receding contacts are of similar magnitude, at 36.8 μm/s and 44.5 μm/s respectively. The reason for the similar rate-dependent responses for the PDMS-PDMS and PDMS-glass interfaces may be due to the viscoelastic response of the PDMS specimen and not influenced by the interface of the rigid substrate.

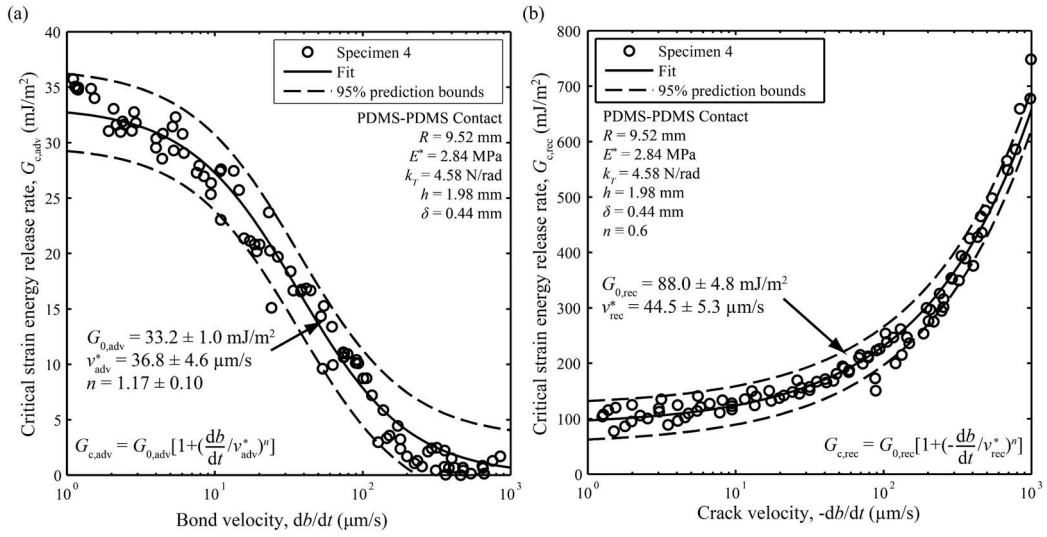

Figure 4-10: Strain energy release rate during (a) loading (R^2 = 0.98) and (b) unloading (R^2 = 0.99) for specimen 4 in contact with PDMS coated glass substrate.

4.5 Summary

In this chapter, a blister contact test is presented to measure the adhesive properties of PDMS-glass interface. An analytical derivation for the system was outlined and the range of applicability for the linear plate model is discussed. It was determined that shear and membrane deformations were important in the experiment, and thus the FE model was used

for analyses. During the bulge test of the PDMS specimen, the elastic modulus and boundary condition are found using DIC. In the BCT, adhesion between the PDMS-glass interface was shown to be rate-dependent for both advancing and receding contact. There is also significant adhesion hysteresis between the advancing and receding contacts, and became more significant as the rate increased. The steady state strain energy release rates were taken as the velocities approach zero and the results are in general agreement with literature values. A PDMS-PDMS adhesion test was also performed and results similar to the PDMS-glass experiments were observed.

The BCT provides a simple method to characterize adhesion of a flat sheet against a rigid surface. In particular, the flat specimens are easy to fabricate and different contact pairs with similar optical properties can be characterized without serious modification to the present technique. Furthermore, the mechanical and adhesive properties can be extracted in the same test. On the other hand, the current BCT depends on the axisymmetric behavior of the specimen. Care must be taken on the fabrication of a uniform thickness specimen as well as the gap uniformity. Uneven specimens can lead to asymmetric in-plane displacements measured with the DIC. Finally, the typical range of specimen dimensions falls in the regime where bending is not the dominant mechanical response, and thus the analysis is done numerically. With a careful selection of dimensions one may be able to use an analytical expression, e.g. the membrane model [28], to extract strain energy release rate efficiently.

CHAPTER 5: Role of bulk viscoelasticity, friction, and repeated contact in an adhesive contact between an elastomer and stiff surface

5.1 Introduction

Strong rate-dependent adhesion is often seen in polymer adhesive contacts [51]. The rate-dependent contact and separation behaviors of a poly(dimethylsiloxane) (PDMS) specimen was studied in chapter 4 and the rate-dependent behavior was attributed to the bulk viscoelasticity of the PDMS [19]. However, the effects of bulk viscoelasticity versus interfacial effects on rate-dependence was not characterized. In previous work, the thickness of PDMS was shown to alter the magnitude of rate-dependent separation but does not change the function dependence on speed [112]. To further investigate the role of bulk viscoelasticity on rate-dependent adhesion, a blister contact test (BCT) experiment was designed to control the amount of PDMS available in the contact experiments. This is done by applying a thin viscoelastic coating onto the rigid substrate and replacing the specimen with an elastic material (section 5.2).

Factors such as the viscoelasticity of the material can influence the dynamics of adhesive contact. Another important factor is the fact that adhesion can evolve over a number of repeated contact cycles [113]. In a repeated contact experiment between PDMS and smooth silicon wafer, the adhesion force decreased over 1000 cycles. The proposed mechanism for the change in adhesion is the detachment of uncured PDMS molecular

chains onto the previously pristine silicon wafer. However, there is a lack of other experiments in support of the research. A similar experiment in which the BCT was repeated 100 times was performed to verify and establish a better understanding of the mechanism.

In many tests, including the JKR test, a frictionless contact is assumed to reduce complexity of the analysis. The BCT analysis also adopts a frictionless contact assumption. For materials that are approximately incompressible (Poisson's ratio close to 0.5), this frictionless assumption is sufficient in the JKR test [114], [115]. However, for materials that are compressible or have a different geometry like the BCT, this frictionless assumption may not be suitable. In this chapter, the effects of friction on BCT are examined in two ways. Firstly, the effects of friction are studied experimentally by measuring the displacement field inside the contact area using the BCT. Comparisons between the experiment data and finite element (FE) simulations show that the polymeric contacts have no-slip friction. Secondly, the von Kármán plate theory (vKPT) model is extended to incorporate friction. The measured contact radius is compared with the modified model to illustrate the difference between frictionless and no-slip conditions.

5.2 Experiments and methods

5.2.1 Sample preparation

The polyethylene terephthalate (PET) film (McMaster-Carr) specimen is prepared by first bonding the bare PET film onto a mounting ring, with the bottom side of the PET film

facing up (Figure 5-1). Then a steel washer is bonded with a cyanoacrylate adhesive onto the bottom side of the film. While the glue is curing a 200 g weight is placed on the washer to create a controlled pre-stress. The cured specimen is then spray coated with paint markers using an air brush and released from the mounting ring. The specimen is cleaned by soaking in isopropanol prior to each series of experiments.

Figure 5-1: Image of a specimen during the preparation process. The 200 g weight was placed on top of the washer while the cyanoacrylate was curing. The PET film was mounted on a two-inch ring in this image.

PDMS specimens were also used in this chapter to demonstrate the effects of friction. The PDMS specimens were cut from flat sheets of commercially made silicone (BISCO, Rogers Corporation). The PDMS specimens were then cleaned by rinsing in isopropyl alcohol and dried with clean nitrogen gas. The specimens were sandwiched between two washers; the specimens were not bonded to either washer.

Silica disks with PDMS coatings were prepared as the contacting substrate in the BCT experiments in this chapter. PDMS was coated onto a one-inch diameter silica disk

via spin coating. Momentive RTV 315 PDMS base and curing agent of 10:1 ratio was first diluted with hexane inside a capped tube. Then the solution was mixed together using a vortex mixer to ensure the solution was evenly mixed. Afterwards, the solution was rested for a short period until no bubbles were visible (usually under 15 mins depending on the solution viscosity), during which the tube was capped to ensure the hexane did not evaporate from the solution. Following the PDMS preparation, approximately 2 mL of the solution was transferred onto the silica disk and covered the entire surface of the disk. The disk was placed on a spin coater and spun at a fixed speed for 160 seconds. Finally, the PDMS on the disk was cured on a hot plate at 95 °C for at least 4 hours. The spin coating process was done in clean room environment to minimize the amount of dust particles on the PDMS surface during the preparation process.

After the PDMS coating was completely cured, part of the coating near the edge was removed using a scalpel. Then, the thickness of the PDMS coating was measured using a 2D stylus profilometer (P-7 Stylus Profiler, KLA-Tencor). Figure 5-2 shows the thickness of the PDMS as a function of the spin rate. The PDMS film thickness is approximately a power law function of the spin rate and the general trend agrees with other publications [77], [116]. As the spin rate increases, the PDMS thickness decreases. Due to the PDMS solution's viscosity, the solution must be diluted using hexane to reach thicknesses of less than 5 μm thick, regardless of the spin rate.

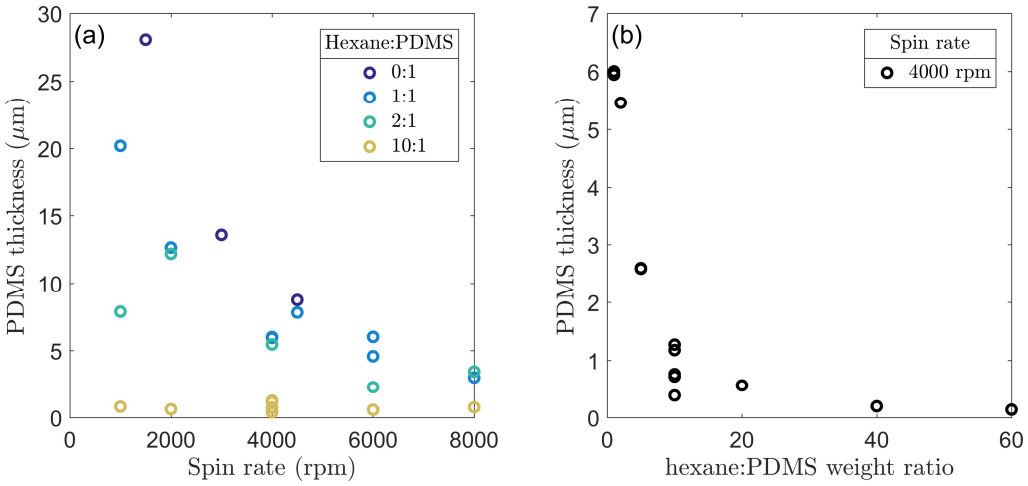

Figure 5-2:PDMS thickness as a function of (a) spin rates at different Hexane-to-PDMS weight ratios; and (b) Hexane-to-PDMS weight ratios at 4000 rpm.

5.2.2 3D digital image correlation

Digital image correlation (DIC) is used to non-destructively measure the displacement field of the blister during the experiment. DIC is a technique to resolve the deformation of unique features between two images. In the BCT, spray paint markers are deposited randomly on the bottom surface of the specimen. The telecentric lens and camera captures the deformation of the specimen without distortion. Typically, a single camera DIC system is only able to capture displacements that are in the imaging plane. A recently developed technique allows for the use of a diffraction grating to capture the axial displacement of the specimen with a single camera [89]–[91]. Figure 5-3 shows the updated schematic of the BCT implemented with the 3D-DIC technique. A diffraction transmission grating is placed between the specimen and the camera. A 1^{st} order diffraction pattern is formed next to the 0^{th} order (original) pattern in a single image captured by the camera. The normal DIC

analysis procedure is performed on both 0^{th} and 1^{st} order images to extract the in-plane displacement fields $u^i(x, y)$ and $v^i(x, y)$, where $i = 0, \pm 1$ denotes the diffraction order. The displacement field of the blister using the 0^{th} and 1^{st} order images is then:

$$u(x, y) = u^0(x, y)$$

$$v(x, y) = v^0(x, y) \tag{5.1}$$

$$w(x, y) = \frac{u^0(x, y) - u^{+1}(x, y)}{\tan\theta}$$

The diffraction angle θ is determined by the pitch of the diffraction grating, p, and the wavelength of the monochromatic light source, λ, by the grating equation $\theta = \sin^{-1} {}^{\lambda}/_{p}$. A larger θ gives a smaller error since the 1^{st} order image displacement is larger. However, it is also located further behind the 0^{th} order image, which may limit the maximum axial displacement of the specimen permissible by the depth of field of the lens. In the current experiment, a 300 grooves/mm, 17.5° blaze angle transmission diffraction grating (Edmund Optics #49-579) is used in conjunction with a 632.8 nm (FWHM of 1 nm) wavelength light source (Thorlabs FL632.8-1).

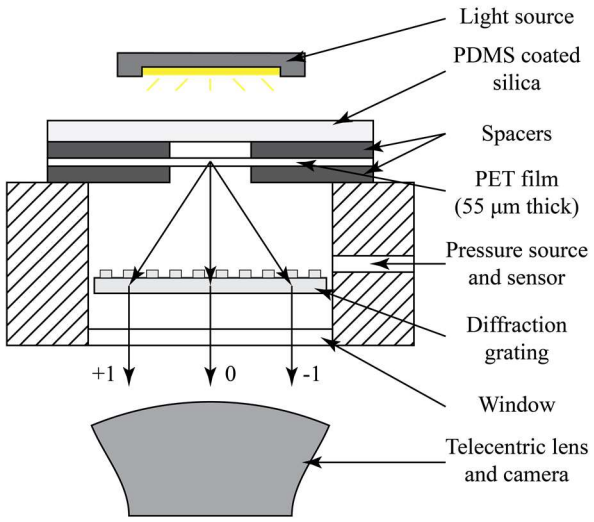

Figure 5-3:Experiment set up of the blister contact test with single camera 3D-DIC implemented. Figure is not drawn to scale.

5.2.3 Experiment Procedure

Before each experiment, the PET film and the PDMS-coated silica substrate are soaked and cleaned using isopropyl alcohol and dried with clean nitrogen gas to remove any dust and organic contamination on the surfaces. The PET film specimen is mounted inside the test chamber after the specimen is cleaned. A 0.38 mm thick washer, which defines the gap δ, is placed between the specimen and the substrate. A load-hold-unload test is repeated for 100 times before the rate-dependent contact tests for each experiment. Figure 5-4 shows the pressure-time profile of the repeated contact test and a typical contact radius measurement.

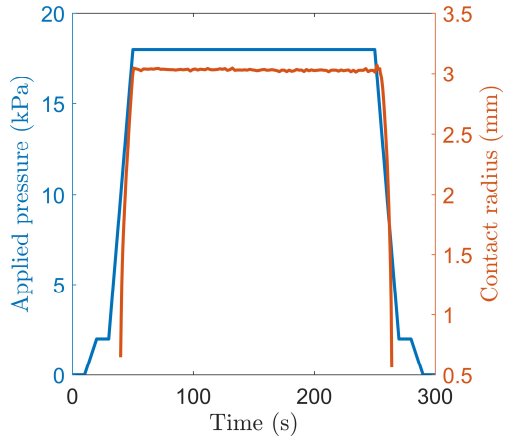

Figure 5-4:Example pressure-time profile and measured contact radius as a function of time for a repeated contact BCT. The data is taken from a 3.5 μm PDMS coating experiment.

5.2.3.1 Rate-dependent contact tests

Rate-dependent contact tests were performed immediately after the repeated contact tests, without any changes to the experiment set up. A typical pressure-time profile during the rate-dependent contact test is the same as the repeated contact test (Figure 5-4), except the load/unload rate for the two segments is varied between 2 and 1600 Pa/s. The load rate and unload rate are the same for each test. The order of these tests was randomized to minimize any other cycle-dependent effect not mitigated by the repeated contact tests.

5.3 Results and discussion

Figure 5-5 shows a typical rate-dependent contact test series. The contact radius for the load segment is smaller than that for the unload segment at a given pressure, indicating that there is contact (and adhesion) hysteresis in these tests. The trend for contact hysteresis as

a function of load/unload rate is the same regardless of the order of the tests performed, showing that the results are independent of the contact cycles.

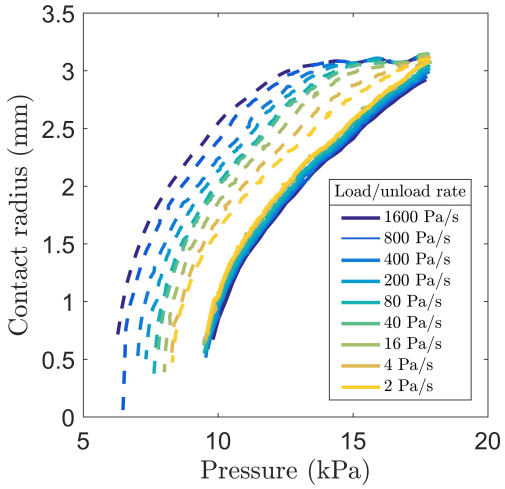

Figure 5-5: Typical contact-pressure response for a rate-dependent test. The solid lines represent the loading segment and the dashed lines represent the unloading segment.

The results section is organized as follows. Section 5.3.1 covers the process of specimen calibration using displacement data obtained by 3D-DIC. Section 5.3.2 investigates the quality of contact area and shows that the surface of the PET specimen is rough. This surface roughness contributes to some of the observations in the BCT. Section 5.3.3 shows the effect of PDMS oligomers transfer during repeated contact over multiple contact tests. Section 5.3.4 discusses the effects of thickness of the PDMS layer on rate-dependent adhesion. It was found that using thin PDMS layers results in reduction in rate-dependence for both contact and separation. The effects of friction in the BCT are explored in section 5.3.5. It was found that friction was present in the PET-PDMS contacts. Experiments on

PDMS specimens in contact with silica substrate are also used to support the findings. The effects of friction are modeled using the vKPT model and results were presented.

5.3.1 Specimen calibration

DIC is a subset-based displacement extraction method – each image is divided into small areas to calculate the local displacements. The key assumption is that each subset is assumed to undergo uniform deformation. This means that the displacements near boundaries, i.e. the outer edge of the blister, may be distorted. Figure 5-6 shows the displacement fields calculated using different subset sizes in comparison to the vKPT solution with elastic properties selected to match the data. The DIC displacements near the center are independent of the subset size. However, the DIC radial displacements near the outer edge vary significantly as a function of subset size. Following this observation, the displacement data near the outer edge is omitted when the data is used to extract the mechanical properties.

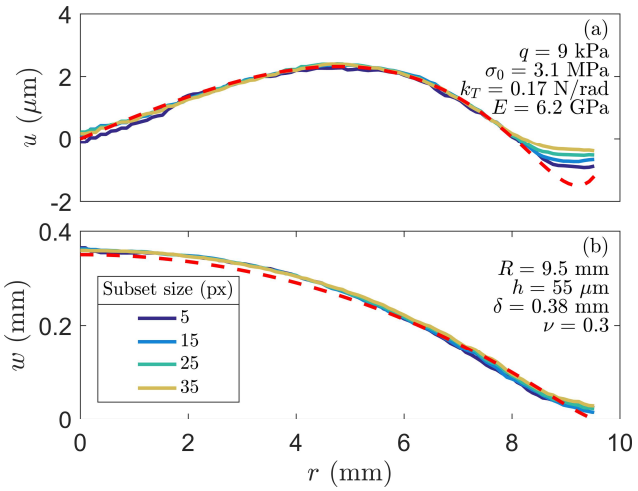

Figure 5-6: (a) Radial and (b) transverse displacements solved with 3D-DIC. The subset size used in 3D-DIC is varied between 5 pixels and 35 pixels. The lines represent the median values of the DIC results; the deviations for each dataset are approximately equivalent for all lines. The red dashed line is the vKPT solution. 5 pixels is equal to 0.14 mm.

Figure 5-7 shows the radial and axial displacements during a typical bulge test. The mechanical properties E, k_T and σ_0 were optimized in MATLAB using the vKPT model; the model results are plotted as dashed lines. Aside from the data near the outer edge, which has been excluded for reasons discussed previously, the experiment data (both u and w) match very well with the vKPT. The mechanical properties extracted from this fitting process were then used to calculate the strain energy release rates in the BCT. Note that the PET films used here are from a different vendor than those used in chapter 6, which have slightly different values of Young's modulus.

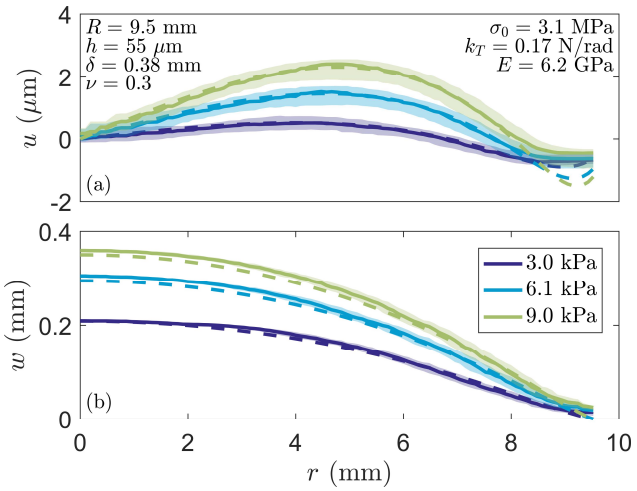

Figure 5-7: (a) Radial and (b) transverse displacement fields during the bulge test. Solid lines represent the 3D DIC results and dashed liens represent the vKPT model with optimized E, k_T and σ_0. The colored region highlights the 25th and 75th quantiles of the DIC results.

5.3.2 Contact area quality

During the tests, PDMS coatings with thicknesses less than 1 μm were not able to make conformal contact with the PET film (Figure 5-8). Since the PDMS coating layers are prepared in a cleanroom and there are no observable particles under an optical microscope near the PDMS surface, the non-conformal contact is believed to be due to the roughness of the PET film. The surface topography of the PET, measured using a white light interferometer (Zygo NewView 7300), shows that while the PET film is relatively smooth with RMS roughness less than 10 nm, there are large asperities present across the surface (Figure 5-9). These large asperities likely lead to the partial contact against thin PDMS coatings. All the adhesion experiments reported in the following sections are for PDMS

coatings greater than 2 μm thick and have good visually conformal contact inside the contact area.

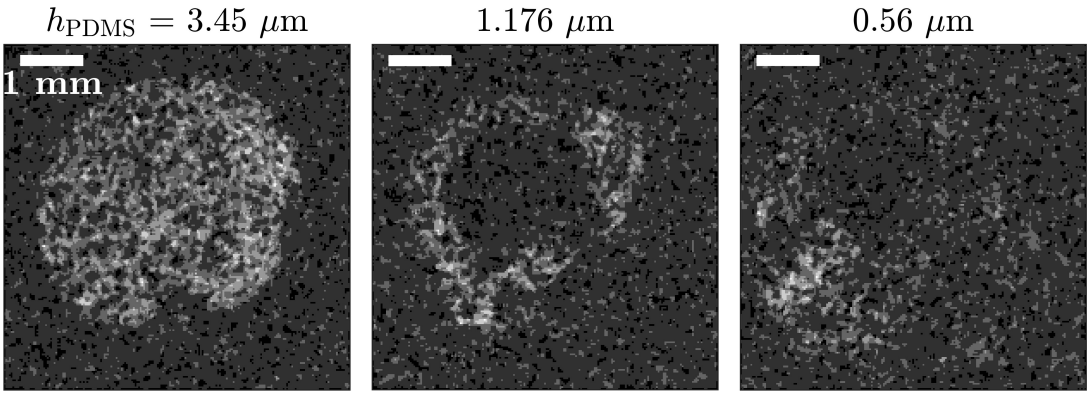

Figure 5-8: Images of the contact area during the blister contact test for three different PDMS coating thicknesses. There are spray paint markers present on the bottom surface inside the contact area. The area in contact is brighter in contrast than the area that is not in contact. Conformal contact is seen in the test against 3.45 μm thick PDMS coating. As the thickness drops below 2 μm the quality of the contact degrades quickly.

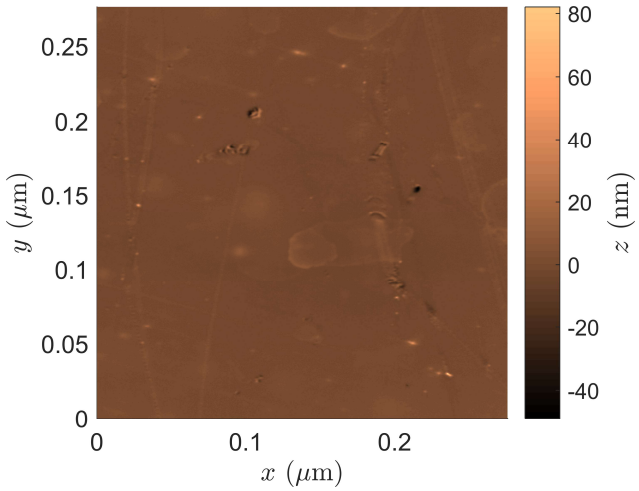

Figure 5-9: Example surface profile of the PET film collected using a white light interferometer. The average surface roughness parameters R_a and R_{rms} are 3.7 and 6.2 nm respectively.

5.3.3 Repeated contact tests

A load-hold-unload cycle was repeated 100 times to observe the effect of repeated contact. Figure 5-10 shows the measured contact radius as a function of contact cycles at the same points during the test. During loading, the measured contact radius drops by 0.1 mm in the first 10 cycles, then recovers slightly, by about 0.03 mm, over 90 cycles. In contrast, during unloading the measured contact radius increases monotonically by 0.1 mm over 100 cycles.

Kroner et al. [113] studied the effects of repeated pull-off between PDMS and silicon wafers using a JKR test. The pull-off force (which is proportional to adhesion energy) was found to decrease over 1000 cycles and the effect was stronger for a less cross linked PDMS. The proposed mechanism was that PDMS free oligomers transferred from the PDMS to the initially clean silicon surface with each contact, effectively turning the test from PDMS-silicon to PDMS-PDMS contact. Since silicon has a higher surface energy than PDMS, when the PDMS is transferred onto the silicon surface the effective adhesion decreases and the measured pull-off force decreases.

Similarly in this experiment, the PDMS oligomers transfer onto the PET surface, reducing the effective adhesion as PET has a slightly higher surface energy than PDMS (but much lower compared to silicon so the observed transfer effect is weaker) [2], [117]. However, as the surface asperities of PET are typically larger than those on a polished silicon surface, the transferred PDMS oligomers fill in the “valleys” on the PET asperities

more readily. This gradual evolution of surface topography then increases the contact radius (i.e. adhesion energy) as the number of contact cycles increases.

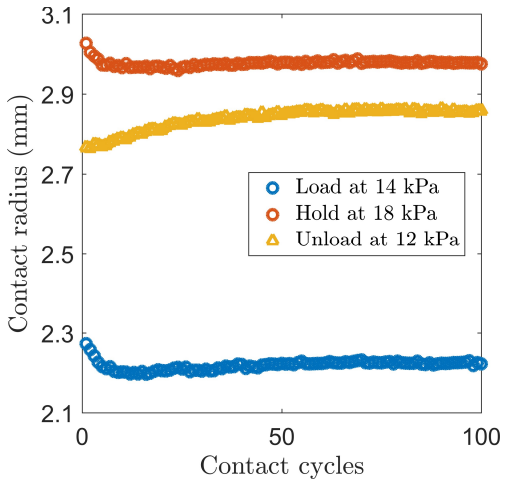

Figure 5-10: Contact radius at 12 kPa during loading and unloading as a function of repeated contact cycles.

5.3.4 Rate-dependent contact tests

Figure 5-5 shows a typical rate-dependent experiment. Strain energy release rates can be calculated using an appropriate mechanics model (section 3.4) at any selected data point of applied pressure and contact radius. At a given pressure, the contact radius is smaller for a higher load rate but is larger for a higher unload rate. Qualitatively, this means that the strain energy release rate is lower as the load rate increases, but higher as the unload rate increases. A larger adhesion hysteresis is observed when the load/unload rate increases. The loading strain energy release rates for a fixed contact radius of 2.5 mm are reported as a function of the contact propagation speed (Figure 5-11, Figure 5-12). The contact propagation speed is calculated by taking the derivative of an adaptive regression fit of the

contact radius versus time curve [118]. The quantitative results are consistent with the qualitative observations described earlier.

Rate-dependent adhesion is typically described by a power-law function known as the Gent model [57] (equation (2.6)). The measured separation energy increases with the contact propagation speed. When the contact propagation speed is large compared to the characteristic velocity v^* the Gent model can be approximated as: $G \approx A|\mathrm{d}b/\mathrm{d}t|^{\alpha}$. The factor α is analogous to the exponent n in equation (2.6), which is typically found to be around 0.6 and describes the degree of rate-dependence on adhesion. The BCT data is fitted with the approximated form to examine how the factor α varies with PDMS coating thicknesses. Other literature has shown that the thickness of the PDMS has no impact on the factor α but on the total adhesion energy A when the PDMS thickness is over 40 μm and contact radius of 3 mm [112]. Because the PDMS coating is not accounted for in the BCT analysis, the true adhesion energy deviates slightly from the reported values. Thus, only the exponent α is investigated in this study.

Typically, PDMS is modeled as an elastic material [119] but the viscoelastic material properties have also been characterized [112], [120]. This is because the viscoelastic component of PDMS is generally much weaker compared to other polymers such as pressure sensitive adhesives. The results show that the rate-dependence originates from the viscoelasticity of PDMS despite the weak viscoelastic components. Furthermore, the exponent α decreases as the thickness of the PDMS coating decreases (Figure 5-11(b)). In contrast, a constant exponent α of around 0.6 is often assumed in other literature and

shown to fit very well in the empirical model. This discrepancy may be because the thickness of PDMS in this study is much smaller than the other literature. The smallest PDMS thickness used in ref. [112] is around 50 μm, almost 4 times larger than the thickest sample used in this study. In comparison, the exponents found in this study are less than 0.17 during unloading, roughly 4 times smaller than the assumed constant exponent of 0.6.

Normally, when the thickness of the viscoelastic layer is large, the underlying rigid substrate does not affect the distribution of the contact stress. However, at very thin layers, the confinement of the viscoelastic material may introduce substrate effects similar to those found in thin film indentation tests [27]. The indenter radius used in ref. [112] was 3 mm and the modulus mismatch between the PDMS and substrate is likely greater than 1000 times at all times. According to ref. [27], the effective modulus of the confined thin film is approximately constant during the indentation test for all film thicknesses. This means the rate-dependence is insensitive to bulk viscoelasticity. However, if the PDMS film is thinner, as it is in the case of the BCT, then the effective modulus can scale with the PDMS time-dependent modulus. In this case, the rate-dependence is sensitive to bulk viscoelasticity.

The results also show stronger overall rate-dependence during unloading than loading. This may be due to both the dynamics of the PDMS layer (e.g. viscoelasticity and molecular rearrangement) as well as the roughness of the contact. When a viscoelastic material (PDMS) is pushed into contact with a rough surface (PET film), macroscopically the contact is conformal. However, the actual contact area may only be at some microscopic

asperities, reducing the true contact to be less than the macroscopically measured contact area [111]. Then, as the viscoelastic PDMS layer relaxes during the dwell period, the soft material fills the gaps between asperities. As the coating thickness decreases, the PDMS layer becomes more difficult to deform to conform to the roughness due to less material available. Thus, the rate-dependence is stronger in unloading than loading.

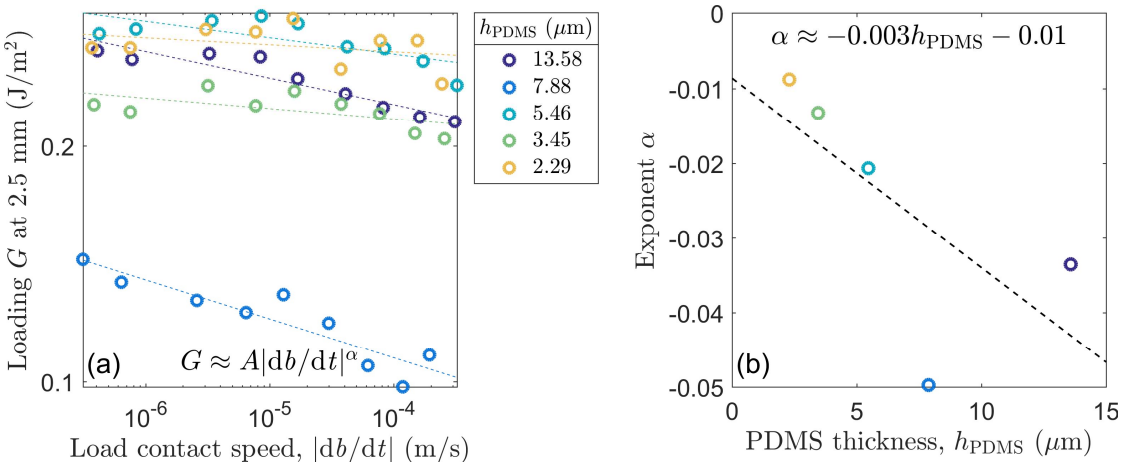

Figure 5-11: (a) Strain energy release rate as a function of contact speed during loading when the contact radius is at 2.5 mm. The dash lines are fits of the data using the equation shown in the figure. (b) Exponent α as a function of the PDMS coating thickness during loading.

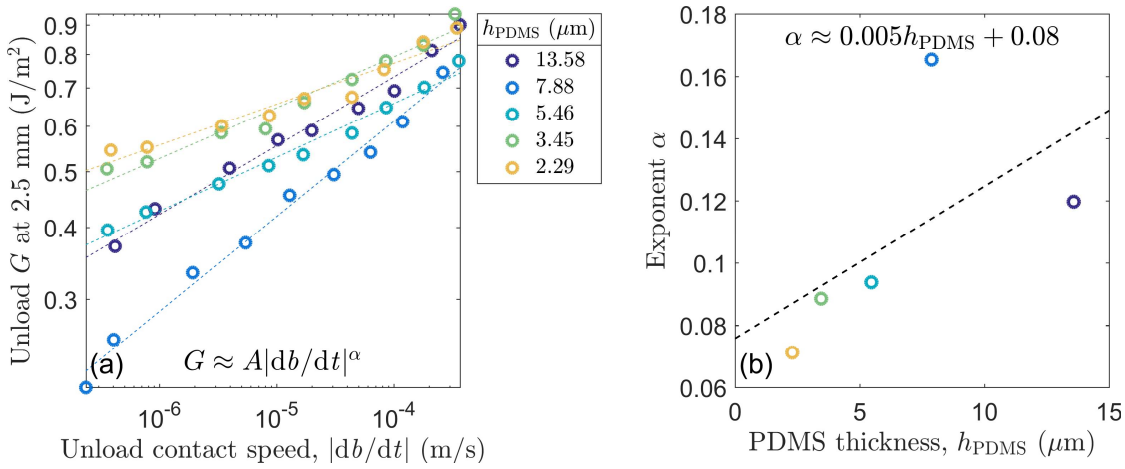

Figure 5-12: (a) Strain energy release rate as a function of contact speed during unloading when the contact radius is at 2.5 mm. The dash lines are fits of the data using the equation shown in the figure. (b) Exponent α as a function of the PDMS coating thickness during unloading.

5.3.5 Effects of friction

Frictionless contact is assumed in the analysis but friction is present in all contacts to different degrees. The 3D-DIC data collected inside the contact area allows for closer investigation of the effects of friction in the BCT. Figure 5-13 shows the displacement data for the PET specimen in contact during loading. FE simulations, also shown in Figure 5-13, without adhesion between frictionless and no-slip contact, are very similar to the measured displacement data. Note that the contact radius is measured directly using image processing, but the results agree with the transverse displacements from the 3D-DIC data (Figure 5-13(b)).

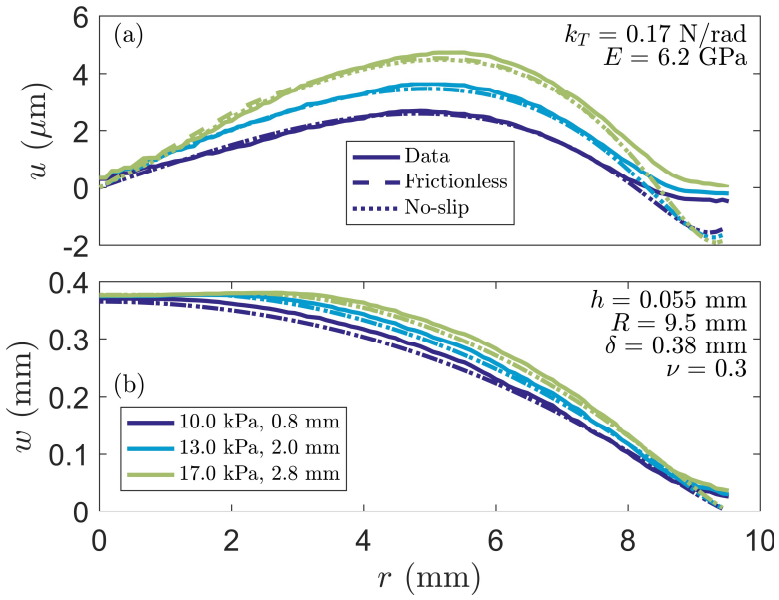

Figure 5-13: (a) Radial and (b) transverse displacements data as a function of radial position compared against Hertz-type contact BCT simulations for the PET specimen. The solid lines represent the data, long dashed lines represent FE frictionless contact and short dashed lines represent FE no-slip contact. The only distinguishable difference between the two FE solutions is u_r at around 2mm. The data shown is during the loading period.

Frictional force restricts in-plane motion on the specimen's top surface. For friction to have an impact on the measured displacements at the bottom surface, the specimen must deform primarily by bending or stretching. Shear deformation only results in transverse displacement and has no impact on the force balance in the axial direction. Stretching deformation is uniform in-plane displacement so its deformation has direct influence with friction. Bending deformation causes rotation about the neutral axis and results in in-plane deformation at the top and bottom surfaces.

For the PET specimen, the h/R ratio is around 0.005 and the δ/R ratio is around 0.04. This corresponds to a strong membrane dominated deformation (Figure 3-8). However, the magnitude of the in-plane deformation of the PET is still relatively small (<

10 μm). The slight difference between the two FE simulations (<0.2 μm difference in u_r) appear to favor the no-slip case more than the frictionless case.

To observe the more significant difference between frictionless and no-slip contact, two PDMS specimens of 0.25 and 0.51 mm in thicknesses were pressurized into adhesive contact with a silica substrate. For the PDMS specimens, the flexural rigidities, $D = Eh^3/12(1-\nu^2)$, of the specimens are much lower than that of the PET specimen, so in-plane displacements are much larger than that for the PET specimens (Figure 5-14 and Figure 5-15). Because of the larger portion of stretching deformation, the 0.25 mm PDMS specimen shows significant difference in radial displacements between frictionless and no-slip contact.

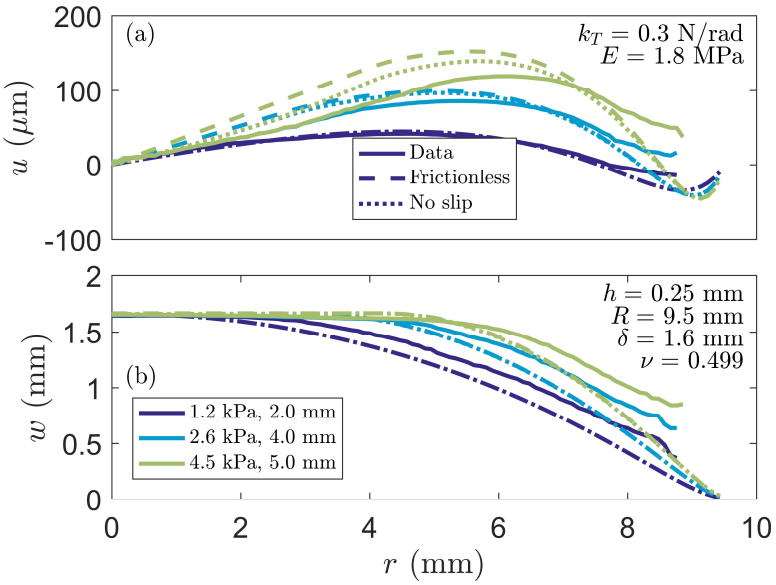

Figure 5-14: (a) Radial and (b) transverse displacements data as a function of radial position compared against Hertz-type contact BCT simulations for the thinner PDMS specimen. The solid lines represent the data, long dashed lines represent frictionless contact and short dashed lines represent no-slip contact. The data shown is during the loading period.

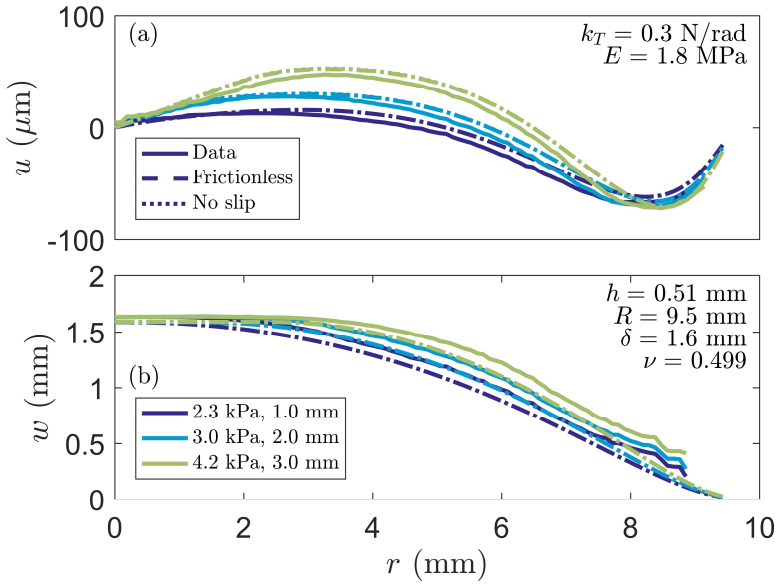

Figure 5-15: (a) Radial and (b) transverse displacements data as a function of radial position compared against Hertz-type contact BCT simulations for the thicker PDMS specimen. The solid lines represent the data, long dashed lines represent frictionless contact and short dashed lines represent no-slip contact. The data shown is during the loading period.

The displacement data for the PDMS specimens are different from the simulation results because of two reasons. Firstly, the simulation is for Hertz-type contact. At the same pressure, the contact radius for the simulation is smaller than an adhesive contact, so the transverse displacements for the simulation are smaller than the data. Secondly, subsequent repeated contact experiments with these PDMS specimens showed that there is some irreversible change in displacement. It is unlikely that the PDMS specimens underwent plastic deformation. Rather, the specimens either slipped along the edges during the experiment or the specimens were not entirely flat initially. This would cause the measured displacements to be larger than the simulations. An alternative observation is that as the pressure increases the radial displacements inside the contact area remain constant. This is

the same for the no-slip simulation but different for the frictionless simulation. Therefore, the 0.25 mm PDMS specimen is most likely a no-slip contact.

There have been some attempts to model adhesive contact with friction in literature [121]–[123], but resolving friction in an adhesive contact system is generally numerically challenging. The radial displacement profile inside the contact area depends on the time history of the contact because friction restricts in-plane motion while it is in contact. To incorporate the no-slip condition in the vKPT model, the solution is solved incrementally in chronological order. The BT model is first solved up until the contact is made. In the first increment where contact is made, frictionless boundary condition is used at the prescribed contact radius, i.e. $u_{r,1}(b_1) = b_1 u'_{r,1}(b_1)$. Then, in the next increment, the radial displacement at the contact edge is the prescribed as the radial displacement solved in the previous increment, i.e. $u_{r,i}(b_i) = u_{r,i-1}(b_i)$, where the subscript i is incremented from 2 to the end of the test.

Figure 5-16 presents results with the modified vKPT model. JKR-type adhesion with $G_{\text{load}} = 0.17\,\text{J/m}^2$ is assumed for loading. The difference between no-slip and frictionless contact is very small when the contact radius is small. At large contact radius (greater than approximately 2 mm), the applied pressure is larger for the no-slip contact than the frictionless contact. At contact radius of around 3 mm during loading, the no-slip model is in better agreement with the experiment data than the frictionless model. For unloading, the no-slip model is also in better agreement with the experiment than the frictionless model (a MD-type contact is assumed and $G_{\text{unload}} = 0.48\,\text{J/m}^2$, $\delta_{\text{adh}} = 10\mu\text{m}$).

The MD-type adhesion model represents a large adhesion range for unloading compared to negligible adhesion range for loading. The larger adhesion range for unloading than loading may be due to deformation of the PDMS layer under adhesion stress during the unloading process, effectively increasing the range of adhesion. This is analogous to the cohesive zones found in pressure sensitive adhesives. On the other hand, because the PET specimen is pushed into the PDMS layer, the contact front advances without the presence of contact stress outside of the contact.

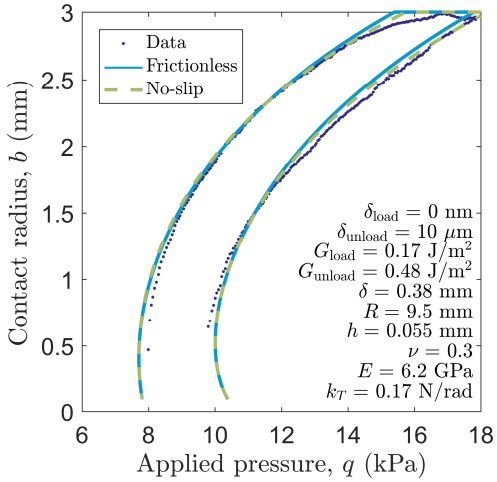

Figure 5-16: Contact radius as a function of applied pressure for the BCT. The data is for the PET-PDMS contact. The vKPT models assume $G_{load} = 0.17$J/m^2 *and JKR-type adhesion for loading,* $G_{unload} = 0.48$J/m^2, $\delta_{adh} =$ 10µm *MD-type adhesion for unloading.*

5.4 Summary

The degree of adhesion and separation rate-dependence was found to be dependent on bulk viscoelasticity. As the amount of viscoelastic material decreases, the degree of rate-

dependence decreases for both adhesion and separation. The result is important in thin film applications such as pressure sensitive adhesives and micro-transfer printing. The adhesive layer in these applications are typically less than 25 μm thick, approaching the regime where the rate-dependence can be altered. The rate-dependence on coating thickness can be leveraged to improve time-dependent properties in these applications.

With the DIC improvements on the BCT, friction was observed in both PET and PDMS specimens that have very different mechanical properties. In both cases, the specimens are closer to a no-slip contact. The vKPT model was modified to include a no-slip condition and the results showed better agreement with the experiment data than using a frictionless condition. The findings helped understand the adhesion condition better and improved the ability for the BCT to characterize adhesion experimentally.

CHAPTER 6: Characterization of pressure sensitive adhesives using the BCT

6.1 Introduction

The performance of pressure sensitive adhesives (PSAs) is very important in many commercial and research applications (Chapter 2). Many existing adhesion testing techniques are not suitable for PSAs due to their soft nature and the effects of the backing layer. In this chapter, the blister contact test (BCT) is used to assess the adhesion of three different types of PSAs and four different kinds of surfaces. The effect of the backing layer is accounted for inherently in the BCT analysis. The effect of the compliant PSA layer is investigated in this chapter and accounted for using a finite element (FE) analysis. The strain energy release rates between the PSAs and surface pairs are reported and compared to extract the acid-base interaction relationships.

6.2 Materials and methods

6.2.1 PSA specimens

To investigate the effects of acid-base interactions on PSA adhesion, PSAs of different compositions were prepared and subsequently characterized with the BCT. The compositions of the PSAs used in this study are summarized in Table 6-1. The PSAs were made by mixing the copolymers together, knife coating onto a nominally 55 μm thick PET sheet, and curing by exposure to an electron beam with an accelerating voltage of 180 kV

and at either 5 MRad or 10 MRad dosage. This produced a PSA layer with a nominal thickness of about 15 μm. The compositions of the PSAs were chosen such that each type displayed a specific type of acid-base interaction. The PSA containing acrylic acid (AA) is acidic, the one containing acrylamide (ACM) is basic, and the isobornyl acrylate (IBOA) is neutral.

Table 6-1: Three PSA formulations used in this study. 2-ethyl hexyl acrylate (2EHA) is a filler material that does not contribute to acid-base interactions.

PSA type	2EHA (%)	AA (%)	ACM (%)	IBOA (%)
Acidic	95	5	0	0
Basic	97.8	0	2.2	0
Neutral	93.2	0	0	6.8

6.2.2 Contacting substrates

Four different types of surfaces (silica, PMMA, PDMS and LDPE) were used in the experiments. The silica and PMMA substrates was purchased from McMaster-Carr (Princeton, NJ). The LDPE substrates were obtained from 3M. The PDMS surface was prepared by spin coating a PDMS layer of approximately 6 μm thick onto a silica substrate.

The surface energies of the substrates were characterized using the van Oss, Chaudhury and Good method [124]. Liquid contact angles using formamide (Sigma-Aldrich), diiodomethane (Sigma-Aldrich) and deionized water were measured using a standard goniometer (ramé-hart). The surface energies, γ_L, of these liquids are reported in [38]. Water is used as a baseline liquid and is assumed to have equal acidic (γ_L^+) and basic

(γ_L^-) surface energies at 25.5 mJ/m^2, and a dispersive component, γ_L^d, of 21.8 mJ/m^2, for a total surface energy of 78 mJ/m^2. Advancing contact angles of the three liquids were measured on each substrate. The components of the substrate surface energy were determined from the measured contact angles using the following equation $\frac{1}{2}\gamma_L(1+\cos\theta) = \sqrt{\gamma^d\gamma_L^d} + \sqrt{\gamma^-\gamma_L^+} + \sqrt{\gamma^+\gamma_L^-}$ [124]. Table 6-2 summarizes the dispersive component, γ^d, acidic polar component, γ^+, and basic polar component, γ^-, of the substrate surface energies. These values are similar to the results found in [125].

Table 6-2: Summary of surface energy characterization of the substrates. The advancing contact angles were measured using a goniometer and were based on six measurements. The surface energy components were calculated using the van Oss, Chaudhury and Good method as described in the text.

Surface	**Advancing contact angle (°)**			**Surface energy components (mJ/m^2)**		
	Water	**Fomamide**	**Diiodomethane**	γ^d	γ^-	γ^+
Silica	61.8 ± 7.8	47.2 ± 6.4	56.2 ± 2.2	30.7 ± 1.3	18.3 ± 10.6	1.5 ± 1.4
PMMA	65.1 ± 1.0	56.0 ± 2.2	38.2 ± 2.6	40.5 ± 1.3	21.0 ± 2.2	0.1 ± 0.1
LDPE	112.4 ± 4.9	92.3 ± 1.9	54.2 ± 5.9	31.9 ± 3.4	0.3 ± 0.9	1.7 ± 1.1
PDMS	117.4 ± 0.5	107.1 ± 2.8	92.5 ± 1.8	11.6 ± 0.8	1.3 ± 0.7	0.2 ± 0.2

In addition to the surface energy, the surface roughness of the substrates can also influence the measured adhesion of the PSA specimens [126]. The surface roughness of the substrates was characterized using a stylus profilometer (P-7, KLA-Tencor, CA) with a nominal probe radius of 2 μm. Line scans, 5 mm in length with 20,000 data points, were recorded and the average roughness, R_a, was calculated. At least six scans on each sample were acquired and the measured values are reported in Figure 6-1. Note, results throughout this paper, including in Figure 6-1, are presented in the form of box plots where the red

line represents the median of the data, the horizontal lines of the blue box represent the 25th and 75th quantiles, and the end of whiskers are the 10th and 90th quantiles. The measured surface roughness of the different substrates is a function of the fabrication method used to make the substrate and the substrate's mechanical properties. For example, the LDPE surface is easily scratched (e.g. during cleaning) and thus the roughness is the largest. The PDMS was spin coated onto a smooth silica disk (the same supplier as the silica samples) and has a low surface roughness. The silica and PMMA surfaces are both relatively smooth with average surface roughness of less than 100 nm.

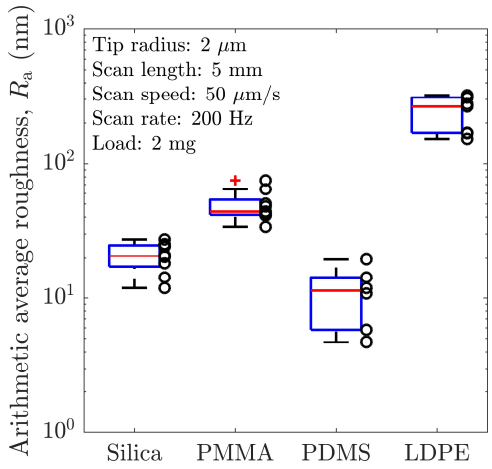

Figure 6-1: Surface roughness of the substrates used in the experiments. Each marker represents the result of a line scan using a stylus profilometer. The boxes and whiskers show the medians and quantiles of the data as described in the text.

6.2.3 BCT sample preparation

The PSA coated PET films were mounted with controlled pre-stress on metal washers (0.75" ID and 1.125" OD) for the BCT. This was done by first mounting the PET film with

the PSA side down to a PMMA ring with an inner diameter of 1.375”. Then a metal washer coated with Loctite 496 cyanoacrylate adhesive was placed in contact with the uncoated side of the PET film, and a 200 g weight was placed on the metal washer while the cyanoacrylate cured. This procedure resulted in a controlled pre-stress in the specimen that helped to keep the specimen initially flat. After the cyanoacrylate was cured, paint markers were randomly deposited onto the side of the specimen without the PSA using an air brush. The markers allowed 2D digital image correlation (DIC) [107] to be used to measure displacements induced by pressurization during the test and in turn extract mechanical properties and calibrate the specimen boundary conditions.

6.2.4 BCT experiment procedure

The prepared specimen was mounted in a custom BCT set up (Figure 6-2) and another washer with a nominal thickness of 0.38 mm was clamped between the specimen and the substrate. Pressurized dry nitrogen was applied to the bottom surface of the specimen and regulated by an electronic pressure regulator (Parker 415 series). A pressure sensor (Honeywell 24PC series) was used to independently monitor the pressure. The pressure regulator was controlled and data from the sensor was recorded via a custom MATLAB script controlling a data acquisition board (National Instruments USB-6211). All tests were pressure-controlled.

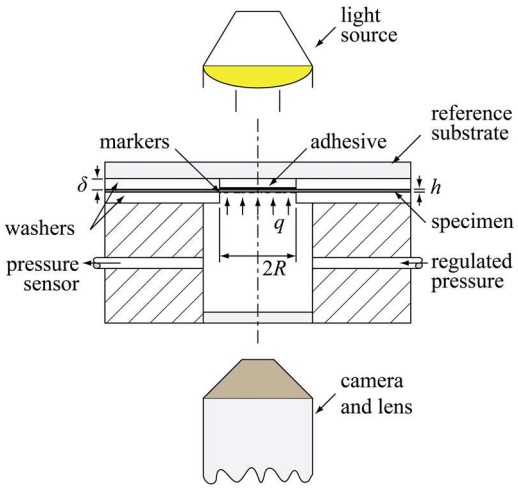

Figure 6-2: Schematic of the BCT experiment set up.

Figure 6-3 shows data from a typical blister contact test of a PSA specimen. Each test is divided into three segments – load, load-dwell and unload-dwell. During the load segment, the pressure was increased to 16 kPa at a constant rate of 40 Pa/s. The specimen makes contact with the substrate during this segment and the contact radius increases with increasing pressure. Then, during the load-dwell segment, the pressure was held at 16 kPa for an extended period of time. This segment was used to observe any time-dependent effects. Typically, the contact radius continues to increase during this segment but at a much slower rate than the load segment. The "load" strain energy release rate is reported at the value at end of this segment (a curve was fitted to around 100 data points near the end of the segment and the value was taken at the end time of the segment). In the unload-dwell segment, the pressure is first decreased to 12 kPa at a constant rate of -40 Pa/s, held at 12 kPa for a short period of time before finally decreased to 0 kPa at the same rate. The contact radius decreases during this segment and the strain energy release rate is reported

as the “unload” strain energy release rate (using the same fitting method as the “load” strain energy release rate).

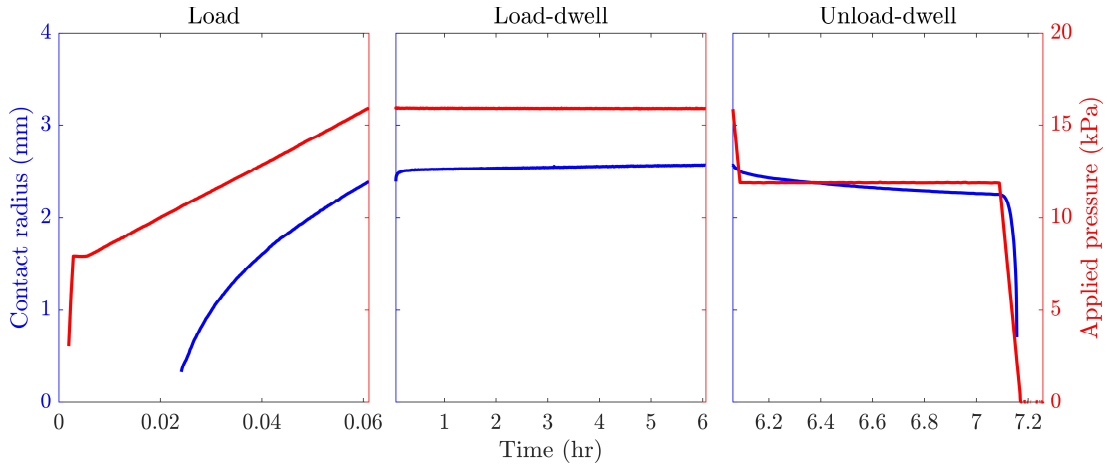

Figure 6-3: Typical applied pressure profile and measured contact radius during a BCT experiment. The specimen makes contact with the substrate as the pressure is increased to 16 kPa in the load segment. The pressure is then held at 16 kPa for 6 hours in the load-dwell segment. Afterwards, the pressure is reduced to 12 kPa and held at 12 kPa for 1 hour, before being reduced to 0 kPa in the unload-dwell segment. The pressure rates are at ±40 Pa/s for all ramp periods.

Over the course of the experiment, the specimen deformation and contact area was optically imaged. The bottom side of the specimen was imaged with a telecentric lens (Navitar 59LGU025) mounted on a digital camera (PixeLINK PL-A741). An LED white light (Metaphase Technologies white LED backlight) provided axial illumination from the top side of the specimen. Images captured during the experiment were used to calibrate the specimen and measure the contact radius. As the specimen was pressurized the markers on the specimen displace within the plane of view. By comparing images at different pressures using a 2D-DIC algorithm, the in-plane displacement field of the markers was extracted [109]. A mechanics model (described below) was fitted to the measured radial

displacements as a function of applied pressure and radial position in order to extract the elastic modulus and pre-stress of the specimen. The images captured during the BCT test were also used to optically track the contact area between the specimen and substrate. There is a distinct change in contrast when the specimen contacts the substrate, thus the contact edge can be identified via image processing. The edge of the contact area was tracked using a canny edge detector [127]. An ellipse and a circle were fitted to the traced edge. In all tests reported in this paper, the major and minor axes of the fitted ellipse were within 10% of the fitted circle radius, indicating that the specimen was reasonably axisymmetric. All image acquisition and image processing were done using custom MATLAB scripts.

The entire test set up was placed in an acrylic enclosure. The enclosure was purged with dry nitrogen gas and desiccants were placed inside the enclosure to maintain less than 10% RH. The temperature was monitored and was between 23 and 25°C for all tests.

6.3 BCT mechanics

The BCT was used to characterize the adhesion between PSAs coated on flexible sheets and various reference substrates. Figure 6-4 shows a diagram of the BCT. A circular specimen of radius R and film thickness h with an adhesive layer of thickness h_{adh} is clamped along the outer edge and a stiff substrate is placed a fixed distance δ above the undeformed specimen. The sheet is assumed to be linear elastic, isotropic, and homogeneous with Young's modulus E and Poisson's ratio ν. The adhesive layer is assumed to be incompressible with Young's modulus E_{adh}. The specimen has an initial

pre-stress σ_0 due to the preparation process. During a test, a uniform pressure q is applied on the bottom surface of the specimen and pushes the specimen into adhesive contact with the substrate resulting in a contact area with radius b.

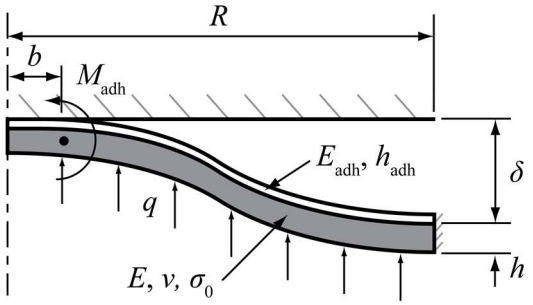

Figure 6-4: Mechanical diagram of the blister contact

6.3.1 Mechanics model of specimen deformation

A semi-analytical mechanics model is developed to analyze the results of the BCT (see also Chapter 3). The aim of the analysis is to allow for the calculation of the strain energy release rate, G, from the applied pressure, measured contact area, and other properties of the system. In this model the adhesive layer is not accounted for but its effect is examined in detail using finite element analysis in the next section. As the specimen is thin and undergoes moderate out-of-plane displacements relative to its thickness, nonlinear deformations that include coupled membrane and bending stresses are expected. Thus, axisymmetric von Kármán plate theory (vKPT) is used to analyze the specimen deformation. The vKPT governing equations in terms of radial displacements, $u(r)$, and out-of-plane displacements, $w(r)$, are [32]:

$$u'' + \frac{u'}{r} - \frac{u}{r^2} = -\frac{1-\nu}{2r} w'^2 - w'w''$$

$$\begin{aligned} D\left(\frac{w'}{r^3} - \frac{w''}{r^2} + \frac{2w'''}{r} + w''''\right) \\ = \frac{Eh}{1-\nu^2}\left[\begin{array}{l}(1-\nu)\left(\frac{uw'}{r^2} - \frac{u'w'}{r} - \frac{w'^2}{2r}\right) \\ +\nu\frac{uw''}{r} + u'w'' + \frac{w'^2 w''}{2}\end{array}\right] \\ +\sigma_0 h\left(\frac{w'}{r} + w''\right) + q, \end{aligned} \tag{6.1}$$

where $D = Eh^3/(1-\nu^2)$ is the flexural rigidity of the specimen. Seven boundary conditions are needed to solve the governing equations and the unknown strain energy release rate, G. The boundary conditions at $r = b$ are: $w = \delta$, $w' = 0$, $G = \frac{D}{2} w''^2$ and $u = u'b$. The boundary conditions at $r = R$ are: $w = 0$, $w' = 0$ and $u = 0$. The governing equations and boundary conditions are solved numerically in MATLAB using the `bvp4c` function [93]. Note that there are three underlying assumptions for these boundary conditions. First, G is directly related to the adhesive moment, M_{adh}, depicted in Figure 6-4 using a fracture mechanics model [101]. Second, the contact is assumed to be frictionless, which allows in-plane displacement within the contact area. Lastly, the outer edge is assumed to be perfectly clamped, which prohibits all displacements at the outer edge.

6.3.2 Finite element simulation of effect of PSA layer

A finite element (FE) model was used to investigate the effect of the PSA layer on the G calculation. While the backing sheet that the PSA is on is much stiffer than the PSA and will control the overall deformation of the specimen in response to the applied pressure, the compliance of the PSA layer can affect the local G at the interface. The specimen is modeled as an axisymmetric continuum in ABAQUS [99]. It is divided into an elastic layer, representing the PET, and a layer with hyperelastic constitutive response, representing the PSA. In the acidic PSA specimen chosen for Figure 6-5, the elastic layer has a Young's modulus of 5.7 GPa, Poisson's ratio of 0.3 and pre-stress of 4.7 MPa. The PSA layer is modeled as an incompressible neo-Hookean material, which has an equivalent Poisson's ratio of 0.5 and equivalent Young's modulus E_{adh}. To simulate adhesion, the nodes within the contact area on the top surface of the PSA layer are displaced vertically by an amount equal to the specified gap, δ, and uniform pressure q is applied on the bottom surface of the PET layer. The strain energy release rate at the crack tip was then calculated using ABAQUS' built-in J-integral method[1].

[1] J-integral was calculated in the FE simulations as the PSA layer was a hyperelastic material. However, to avoid confusion with interchanging between terms, "strain energy release rate" is still used for the FE solution. FE simulations in this work showed negligible differences using either an elastic or hyperelastic constitutive model for the PSA layer.

Figure 6-5 compares the strain energy release rates calculated from the FE model including the PSA layer and the strain energy release rates from vKPT model described in section 3.1. If the PSA had no effect, G_{FE} and G_{vKPT} would be equal to one another. The results are shown for three different contact radii / strain energy release rates that are representative of the experiments reported in this paper. The results show that the compliance of the PSA reduces the strain energy release rate. For an adhesive layer that is 15 μm thick and has a Young's modulus of 10 kPa, the reduction is approximately 40%. The effect is smaller when the adhesive is thinner and/or has a higher modulus.

It is worth noting that the ratios between G_{FE} and G_{vKPT} are approximately constant for all the data reported in this work (see section 6.3.2.1). Therefore, the qualitative observations from analyzing the BCT data with the vKPT model and the FE model are similar. This implies that if the PSAs have similar mechanical properties (h_{adh}, E_{adh}), then the qualitative conclusions for acid-base interactions are equivalent using either model. Hence, one may choose the appropriate model based on time and the goal of the BCT experiments (i.e., comparison between different PSA formulations versus measurement of exact values of adhesion energy). The vKPT model is typically faster to compute, while the finite element model is more accurate

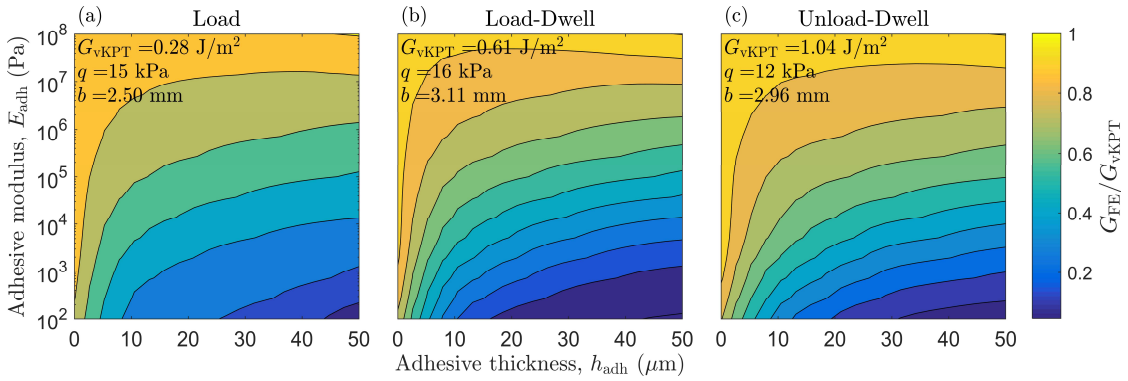

Figure 6-5: Strain energy release rate comparison between FE and vKPT model. The FE simulation includes an adhesive coating with varying Young's modulus and coating thickness. The mechanical properties are taken from the long dwell time experiment (Figure 6-12) during (a) the beginning of load-dwell segment, (b) the end of load-dwell segment, and (c) the end of the unload-dwell segment.

6.3.2.1 Correlation between vKPT and FE model

Figure 6-6 shows the correlation between the strain energy release rates calculated by vKPT model, G_{vKPT}, and that calculated by the FE model, G_{FE}, for the data reported in Figure 6-10 (which is included in the results section 6.4). G_{vKPT} is approximately 50% higher than G_{FE}. As the correlation is mostly linear, the qualitative observations from sections 6.4.2 and 6.4.3 are the same using either the vKPT model or FE simulation. The vKPT model is significantly faster than the FE simulation but does not account for the compliance of the PSA layer.

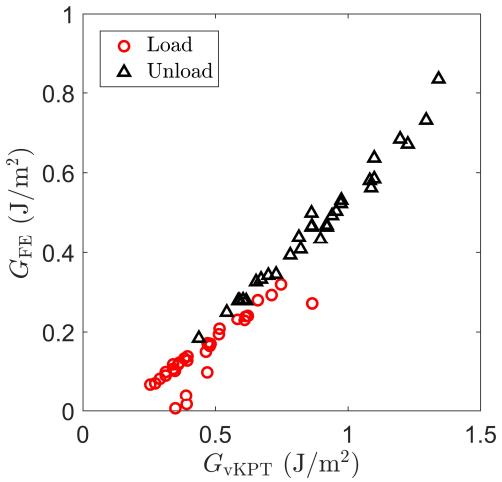

Figure 6-6: Correlation between the strain energy release rates calculated using the vKPT model and that calculated using the FE model. The FE model assumes an adhesive layer of 10 kPa in Young's modulus and 15 μm in thickness.

6.3.2.2 Viscoelastic properties of PSA specimens

The viscoelastic properties of the PSA specimens were characterized using a dynamic mechanical analysis. The temperature and frequency were varied to create a time-temperature superposition master curve for each PSA specimen [128]. For each test, the frequency was varied from 0.1 to 100 Hz and the temperature was varied between -60 and 170 °C. The reference temperature, T_r, is set to 25°C in the master curve. Since the temperature fluctuations during the BCT were very small, $T_r/T \approx 1$ and the shift factor $a(T) \approx 1$. The master curves for the storage modulus, $G_s(\omega)$, and loss modulus, $G_l(\omega)$, can be fitted with Prony series [99]:

$$G_s(\omega) = G_0\left[1 - \sum_{i=1}^{N} \bar{g}_i^P\right] + G_0 \sum_{i=1}^{N} \frac{\bar{g}_i^P \tau_i^2 \omega^2}{1 + \tau_i^2 \omega^2} \tag{6.2}$$

$$G_l(\omega) = G_0 \sum_{i=1}^{N} \frac{\bar{g}_i^P \tau_i^2 \omega^2}{1 + \tau_i^2 \omega^2} \tag{6.3}$$

where $G_0 \equiv \lim_{\omega \to \infty} G_s(\omega)$ is the instantaneous modulus, ω is the frequency, N is the number of terms in the Prony series and $\bar{g}_i^P$, τ_i are the fitting parameters in the Prony series. Instead of fitting both parameters, τ_i is set to be spaced evenly on logarithmic scale over the data. The fitting algorithm is weighted towards the storage modulus rather than loss modulus. Figure 6-7 shows the data (markers) and the 13-term Prony series fit (lines) of the three types of PSAs.

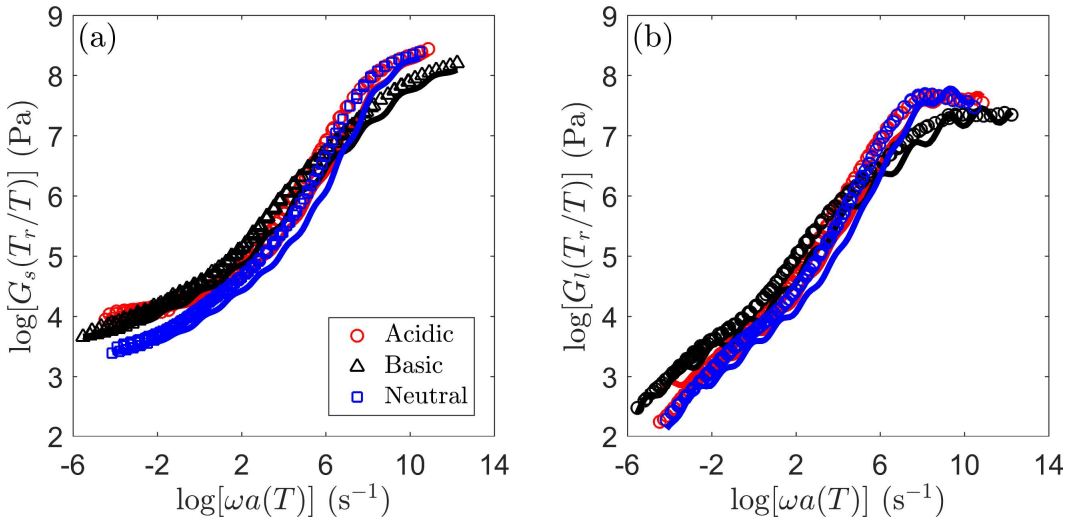

Figure 6-7: (a) Dynamic storage shear modulus and (b) dynamic loss shear modulus master curves of the three types of PSAs measured using a dynamic mechanical tester. The markers represent the data and the lines are the Prony series fits to the data.

6.4 Results and discussion

The results section is organized as follows. First, the calibration tests to obtain the mechanical properties (Young's modulus and pre-stress) are summarized in section 6.4.1. Then, the effect of PSA specimen cure dosage is measured and reported in section 6.4.2. Next, the acid-base interactions for the PSA and substrate pair are characterized in section 6.4.3. The contact area during the BCT are inspected closely in section 6.4.4. Finally, viscoelastic contributions of the PSA layer are explored in section 6.4.5.

6.4.1 Calibration of BCT specimens

The Young's modulus E and pre-stress σ_0 of each specimen tested was determined by pressurizing the specimen, but without contact to the reference substrate, and using 2D-DIC to measure the in-plane displacements. The measured radial displacement field was compared to predictions from the vKPT model. The boundary conditions for the vKPT model at plate center, $r = 0$, are modified to: $w' = 0$, $w'' = 0$ and $u = 0$. The Young's modulus and pre-stress in the model were varied to achieve agreement between the model predictions and measurements. Figure 6-8 shows the results for two of the specimens at three different applied pressures. By fitting the model to the experimental data, the PSA specimens were determined to have a Young's modulus of 5.7 GPa and pre-stresses between 2 and 8 MPa (the pre-stress values varied between specimens). In the fitting, the Poisson's ratio was assumed to be 0.3.

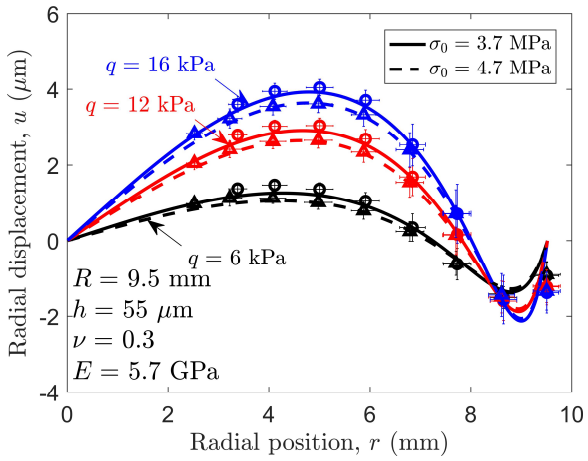

Figure 6-8: Comparison of radial displacements between experiment data (markers) and the vKPT (line) calculated using the fitted Young's modulus E and pre-stress σ_0. Two specimens (circle markers, solid lines vs. triangle markers, dashed lines) at three different pressures (6, 12, 16 kPa with black, red, blue colors respectively) are shown.

Independent tensile tests were also performed on bare PET films. Briefly, tensile strips that were nominally 20 by 150 mm were loaded in tension at a rate of 5 mm/min in a standard tensile test machine. Displacements were measured using 2D-DIC during the tests. The average Young's modulus and Poisson's ratio from the tensile tests were 5.6 GPa and 0.32 respectively.

6.4.2 Curing dosage effects

The PSAs tested were cured by electron beam radiation at two levels of dosages, 5 and 10 MRad, to study the degrees of crosslinks in the adhesive. Figure 6-9 shows the measured strain energy release rates for the acidic PSA specimen. The difference between the two dosages during loading is small, suggesting that there is no effect from the two levels of cure dosages. However, the unload strain energy release rates are higher for the lower

dosage. When the PSA is pushed into contact, the dosage level plays less of a role than the chemical bonding between the two surfaces, as the crosslinked polymers are compressed together. However, as the surfaces separate, the polymer chains are stretched apart. A less cured PSA has fewer entangled polymer chains and is allowed to stretch more. This causes the unload strain energy release rates to be higher in the lower dosage.

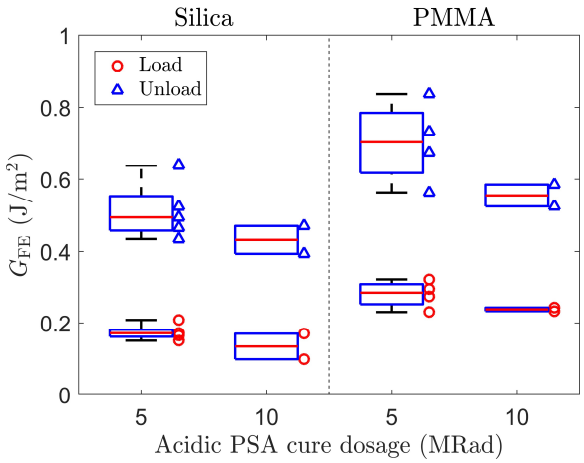

Figure 6-9: Measured strain energy release rates between the acidic PSA specimen and two different substrates. The box-and-whiskers plots follow the same conventions defined in Figure 6-1. Load data is taken at the end of the 6-hour load-dwell period and unload data is taken at the end of the 1-hour unload-dwell period.

6.4.3 Acid-base interactions

Adhesive contact between two surfaces is affected by the chemical composition of the PSAs relative to the composition of the surfaces. The experimental results for the different PSA-substrate pairs in Figure 6-10 show the measured strain energy release rates are strongly dependent on the type of acid-base interactions. The experiment results can be explained with reference to the surface energy components measured by the contact angle

method (Table 6-2). PMMA has a larger basic surface energy component than silica, so the acidic PSA adheres stronger to PMMA than silica. The silica also has a weak acidic surface energy component, so the strain energy release rate is higher than PMMA when it makes adhesive contact with the basic PSA. LDPE and PDMS are both mostly dispersive with no polar components, so they do not adhere to the acidic PSA as well. The LDPE-acidic PSA contact has a larger unload strain energy release rate than PDMS-acidic PSA contact, this is believed to be due to the larger surface roughness of the LDPE.

For the neutral PSA, only dispersive interaction is expected with the silica and PMMA substrate. The strain energy release rate between PMMA-neutral PSA is higher than that between silica-neutral PSA since the PMMA has a larger measured dispersive surface energy component than silica.

The results show that the BCT can be used as an alternative method to estimate the polarity of acid-base interactions between PSAs and different substrate materials. Previously, most tests for acid-base interactions of the surfaces, such as micro-calorimetry or contact angle measurements [38], are chemistry based, and do not account for the physical properties of the specimen. The BCT provides a mechanics-based test for specimens that are thinly coated on a substrate. Similar to the van Oss, Chaudhury and Good method, by performing BCT against reference substrates (silica, PMMA, etc.), the polarity of the unknown material can be deduced. The measured strain energy release rates in the BCT provide a better metric for determining the adhesion strength of PSA on the substrate than the thermodynamic work of adhesion values obtained from contact angle

measurements, as the BCT accounts for the geometrical and mechanical properties of the specimen whereas contact angle measurements only report the surface chemistry.

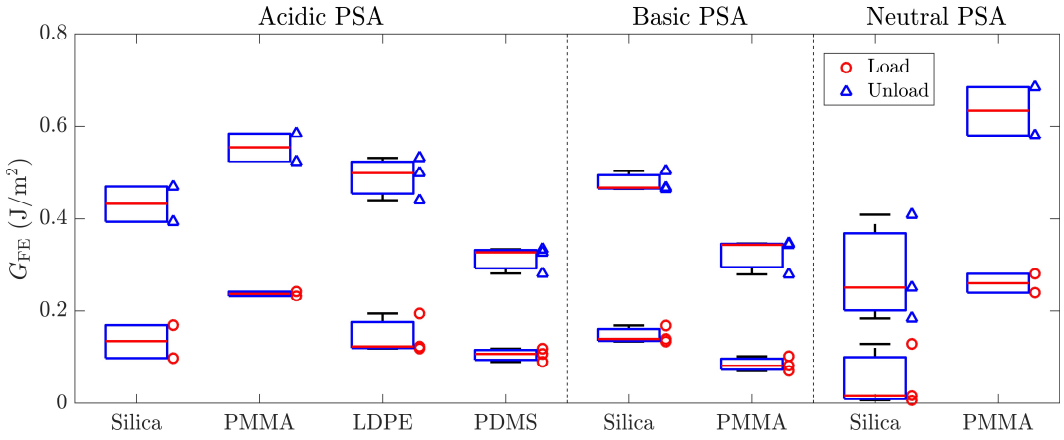

Figure 6-10: Measured strain energy release rates for the three different PSAs (10 MRad dosage) in contact with several different substrates. In the analysis to calculate the strain energy release rate, the adhesive layer is assumed to be 15 μm thick and have a Young's modulus of 10 kPa.

6.4.4 Typical contact characteristics

The contact area was imaged and the contact radius was tracked optically during the experiments. Figure 6-11 shows the contact area during the three segments for a typical test. During the load segment, the contact edge is well defined by a sharp change in contrast. However, during the load-dwell segment finger-like structures are observed near the contact edge. In addition, some cavities are observed near the inner contact edge during unloading. The size of the fingers grows as the dwell time increases. The fingers and cavities have been observed in other experiments [129]–[131] during unloading but were not reported during loading. In those experiments, the formation of these fingers or cavities were caused by factors such as the elastic modulus, adhesion energy and degree of

confinement of the soft elastomeric layer. The initiation of cavities occurs when the adhesion energy is greater than the elastic modulus of the soft polymer during separation [132]. The formation of fingers is related to the confinement (thickness of adhesive) of the soft polymer layer, as well as the ratio of the elastic modulus of the soft polymer versus the rigidity of the substrate. In both cases, their physical appearances are the results of mechanical instabilities that choose the most energetically favorable shape. In either case, the size of these instabilities is only a fraction of the total contact area in the BCT. To be consistent, the inner contact edge is used to calculate the strain energy release rates.

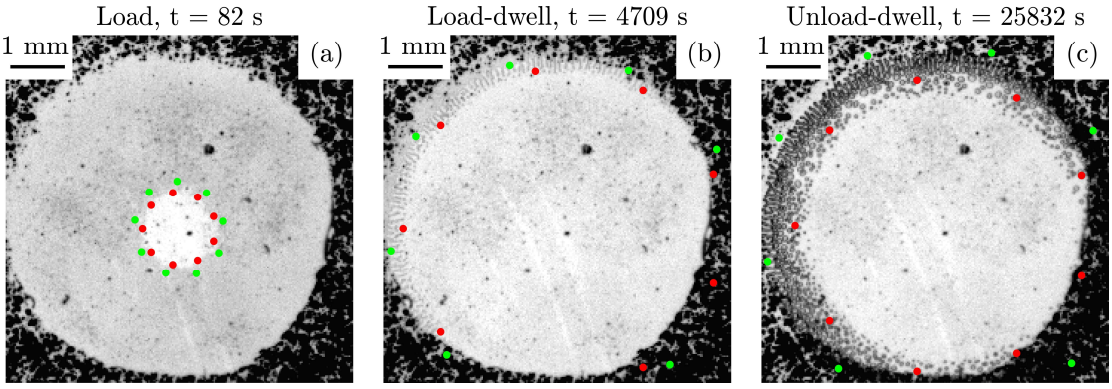

Figure 6-11: Images of contact area during (a) load, (b) load-dwell and (c) unload-dwell segments for the acidic PSA specimen. The red and green markers are the abest fits of the inner and outer contact edges respectively. Most of the instabilities are observed between the inner and outer contact edges. The data is taken from the acidic PSA in contact with a PMMA substrate.

6.4.5 Long-term contact behavior and viscoelasticity of the PSAs

During a typical BCT on the PSAs in this work, the contact area continues to change even when the applied pressure is held for an extended period of time. To investigate the time-dependence of the PSA specimens, a blister contact test with a 10-day load-dwell segment

was performed. Figure 6-12 shows the measured contact radius during the dwell segment. The measured strain energy release rate follows the shape of the contact radius curve closely and can be approximated by the inset equation. Under constant test conditions the contact area continues to grow over 10 days. This behavior could be caused by viscoelasticity of the PSA, evolution of interface bonding, or both.

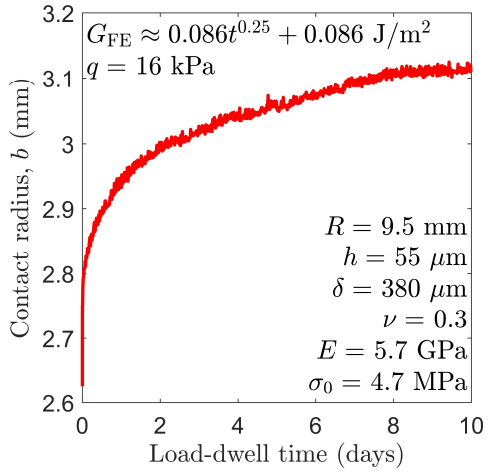

Figure 6-12: Contact radius during the load-dwell period at 16 kPa over 10 days. The corresponding strain energy release rate is approximated by the equation in the figure. The measured G_{FE} increases from 0.09 to 0.24 J/m^2 during the load-dwell period. The data is taken from the acidic PSA specimen in contact with a PDMS surface.

To investigate if the viscoelasticity of the PSA layer contributes significantly to the long term growth of the contact area, dynamic mechanical tests were performed on PSAs (see section 6.3.2.2 for details). Viscoelastic material properties for the PSAs were extracted and the data was used to define the constitutive response of the PSA in the aforementioned ABAQUS FE analysis. Figure 6-13 shows the simulated Hertz-type contact (without adhesion) during the load-dwell segment. It is evident that the

viscoelasticity of PSA leads to very long time-dependent changes in contact radius. This time-dependent effect in the simulation is solely due to the viscoelasticity of the PSA layer, even though the stiffness of the PSA is much less than the stiffness of the substrate at the time scales of the experiments. The inclusion of adhesion in the FE model can potentially further enhance the time-dependent effect to be more comparable quantitatively with the experiment data. Evolving interfacial bonding, chemical or mechanical in nature, may also contribute to the time-dependent effect.

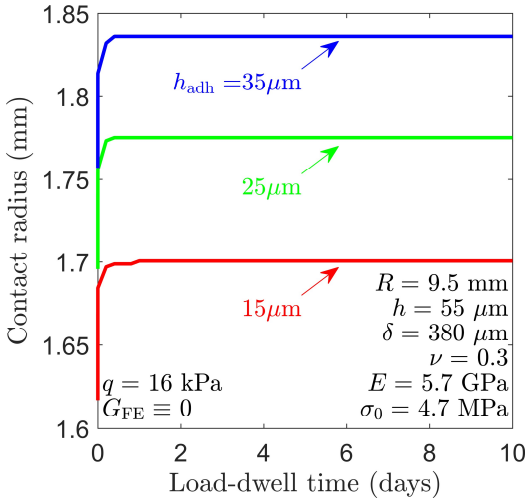

Figure 6-13: FE simulations of the BCT with a viscoelastic PSA layer of three different thicknesses included. The mechanical properties for the PSA were taken from the acidic PSA's dynamic mechanical test results, assuming the Poisson's ratio is 0.5.

6.5 Summary

The adhesive properties of thin PSA layers coated on PET films were characterized using the BCT. PSAs of three different compositions were tested against four different types of

substrates. The effect of acid-base interactions was clearly seen in the adhesion measurements. The BCT results qualitatively agree with those extracted using a traditional liquid contact angle measurement technique. The BCT demonstrated the ability to measure the effect of acid-base interactions on adhesion between the PSA and a substrate using a mechanics based test. The results present an opportunity to mechanically characterize PSA in the form of a thin coating on an elastic sheet. The long time-dependence of PSA was also investigated and the viscoelastic behavior of PSA was shown to influence the time-dependence significantly despite the thin layer and low stiffness compared to the elastic layer it is coated on. During the tests, instabilities in the form of cavities and fingering were observed near the contact edge. More work is required to study these instabilities in detail.

CHAPTER 7: Summary and contributions

7.1 Summary

The adhesive properties of flexible polymer sheets are important for a wide variety of applications, such as pressure sensitive adhesive tapes, microtransfer printing of thin electronic devices, and bioinspired adhesives. These applications typically employ a flat sheet geometry to reduce manufacturing challenges. The contact and separation properties of these soft polymer sheets in contact with a stiff substrate are important in these applications. However, traditional adhesion testing techniques present challenges in characterizing these systems due to the geometry as well as the mechanical properties. While the peel test is the most commonly used adhesion testing method for these types of applications, it is only able to measure the separation properties.

To address the lack of a comprehensive testing technique, the blister contact test (BCT) was developed to characterize the contact and separation behaviors of flat polymer sheets in contact with a stiff substrate (Chapter 3). The BCT inflates a circular flat specimen by pressure and pushes the specimen into adhesive contact with a stiff substrate. The contact area and applied pressure were monitored and the strain energy release rate was calculated from the adhesion and separation data using a mechanics model. The design and mechanics of the BCT was studied in detail. A nonlinear von Kármán plate theory, which includes bending and stretching deformation, was used to derive the mechanics model for the BCT. The model solution was compared against finite element analyses to establish the

relationships between specimen geometries (thickness, deflection, etc.) and the deformation mechanics (shear, bending and stretching). The results are used to identify the appropriate mechanics model and assumptions for data analysis.

An experimental set up was developed to implement the BCT (Chapter 4). 2D digital image correlation (2D-DIC) was implemented initially to measure the in-plane displacements during the test for specimen calibrations. The radial displacements from experiments were compared with the mechanics model during the bulge test (BT), the inflation period before the specimen made adhesive contact, and the mechanical properties of the specimen were determined through fitting. Once the specimen made adhesive contact, the contact radius was tracked as a function of the applied pressure and the strain energy release rate was calculated with the appropriate mechanics model.

Rate-dependent contact and separation behaviors between poly(dimethylsiloxane) (PDMS) specimen and glass substrate were first characterized to validate the BCT experiment set up. The strain energy release rates were found to depend on the contact propagation rate in a power law relation. This power law related the strain energy release rate with the contact propagation rate with a steady state strain energy release rate, a characteristic contact velocity and a scaling exponent. For receding contact, the strain energy release rate increased as the contact rate increased. The results agreed with the well-known empirical model proposed by Gent and used in many other literatures. For advancing contact, the strain energy release rate decreased as the contact rate increased. A modified empirical model from the Gent model was used to fit the results. The steady state

strain energy release rate for advancing contact was comparable to the thermodynamic work of adhesion for a PDMS-glass interface.

Rate-dependent adhesion and separation properties of polymers are commonly leveraged in transfer printing applications. Rate-dependence was attributed to the bulk viscoelasticity of the polymer in other literature but was not investigated in detail in the BCT experiments in Chapter 4. To study the mechanical influence of bulk viscoelasticity, PDMS coatings of different thicknesses on silica substrates were used to make contact with an elastic PET film using the BCT (Chapter 5). The variation of thickness allowed the control of the bulk material properties with the surface properties unchanged. It was found that the exponent in the rate-dependent expression depended on the thickness of the PDMS layer when the layer was below 10 μm thick, in contrast to the reports in the literature. This rate-dependence was likely due to thin film confinement effects and was not observed unless the layer was sufficiently thin.

To study the effects of friction on BCT, 3D-DIC was implemented experimentally (Chapter 5). Using 3D-DIC, the radial and axial displacements were measured both inside and outside of the contact area during the experiments. Experimentally, the measured radial displacements inside the contact area showed that friction restricts in-plane motion inside the contact area. Both polyethylene terephthalate (PET)-PDMS and PDMS-silica contacts were closer to no-slip than frictionless. Following the experimental observation, the no-slip boundary condition was implemented in the vKPT model. The no-slip condition

showed slightly better fits to the experimentally measured contact radius than the frictionless condition.

The BCT experiments were also used to characterize contact and separation properties of pressure sensitive adhesives in contact with different substrates (Chapter 6). PET specimens with PSA coatings of different chemical compositions were used to make adhesive contact with different substrates (PMMA, LDPE, silica and PDMS). The PET specimens have vastly different mechanical properties compared to the PDMS specimens used in Chapter 4. Furthermore, the PSA coatings interact with the substrates via acid-base interactions, different from the purely dispersive interaction observed in PDMS contacts. Specifically, the three PSA coatings represent acidic, basic, and neutral polarities. The results from a series of BCTs showed that the acidic PSA adheres strongest to the PMMA surface, basic PSA adheres strongest to the silica surface, and the neutral PSA adheres strongest to the PMMA surface. From the experiments, it was deduced that the PMMA was a basic surface, the silica surface was acidic (and slightly basic), and the LDPE and PDMS surfaces were dispersive (non-polar). These results agreed with the surface energy characterization of the same substrates using the traditional contact angle measurement method. During the experiment, it was also found that the strain energy release rate continued to increase during the dwell period for more than 10 days. Finite element simulations that included a viscoelastic layer representing the PSAs were performed. The results confirmed that the dwell time effect was partially due to the viscoelastic PSA layer despite its low stiffness compared to the PET film.

7.2 Contributions

Even though there were a few published reports of the BCT, little work had been done to establish the proper mechanics for implementing the BCT successfully. For instance, the BCT was analyzed using membrane theory without quantitative justification of whether bending stresses were as important as membrane stresses. Analytical models that have similar simplifying assumptions were incapable of providing sufficient comparisons of these deformation mechanics to draw conclusions. To this end, a finite element model was developed to compare against the analytical models. The finite element model included all deformation mechanisms and the direct comparison with each mechanics models allowed each deformation mechanism to be quantified. The ranges of the important parameters for each deformation mechanism can aid future designs and implementation of the BCT.

One of the BCT experiments reported in literature [28] measured the slope of the blister outside the contact area to extract adhesion range. In this work, a direct full field 3D displacement characterization of BCT specimens was implemented using 3D-DIC. Complemented with the precise closed-loop control of applied pressure and ability to track contact radius with sub-pixel resolution, the 3D-DIC measurement technique provides an abundance of information to characterize adhesion and separation behaviors of flat specimens. Using the 3D displacement data of a PET-PDMS contact, friction was experimentally characterized and its effects were modeled using a modified vKPT model. Traditional adhesion testing methods, such as the JKR test, often assume a friction

condition, so the ability to observe the effects of friction directly provided more accurate understanding of the contact mechanics between the surfaces.

A key application of the BCT in this work is the characterization of rate-dependent adhesion and separation behavior of soft polymers. Many pressure sensitive adhesives exhibit strong rate-dependent behavior. However, most existing tests are focused on characterizing the separation behavior only. The BCT controls loading and unloading pressure and rate directly using an electronic pressure regulator, achieving contact and separation rates that span several orders of magnitudes. The separation data with PDMS-glass contact compares favorably with other literature using the Gent model. For loading data, there are few reports that characterizes the rate-dependence. The loading data for the BCT was described using a modified Gent model. The results revealed that the steady state strain energy release rates for loading are comparable to the thermodynamic work of adhesion, whereas the steady state strain energy release rates for unloading are often larger than the thermodynamic work of adhesion due to other effects, e.g. roughness and humidity, unaccounted for.

Polar interactions between surfaces can be quite important in the performance of pressure sensitive adhesives that have applications against targeted surfaces. The acid-base interactions can enhance adhesion significantly, but the low modulus of the pressure sensitive adhesive makes its characterization in separation-based tests difficult. The measured separation energy of PSA is often much larger than their elastic energy, leading to significant amount of plastic deformation in the form of cavitation and fibrillation.

Therefore, studying the adhesion behavior rather than the separation behavior allows a more accurate characterization of fundamental adhesion of PSAs. To do so, the acid-base interactions of three PSAs with different formulations were characterized using the BCT. The results, compared with contact angle measurements, demonstrated that the BCT can be used to identify the surface energy polarities of an unknown PSA using reference surfaces. The BCT provides a mechanics-based test for characterizing acid-base interactions and an alternative to the traditional chemistry-based contact angle test.

7.3 Future work

7.3.1 Experimental improvements for the BCT

The current BCT provides a rich amount of information – the 3D displacement fields are extracted and the contact area is measured optically during the experiment. Nonetheless, there is room for improvement for the experiment. Firstly, because of the partial obstruction of the 1st order diffraction image, the transverse displacement field can be only extracted on part of the specimen. To this end, the BCT pressure chamber can be resized to allow full view of the 1st order diffraction image. This is a very simple modification to improve the quality of the displacement data significantly.

Furthermore, some simple improvements to the setup can lead to higher resolution in displacement measurements easily. In [89], [90], the theoretical transverse displacement resolution is less than one pixel using the current BCT design. This is equivalent to less than 25 microns in transverse displacement resolution. More importantly, this resolution

directly scales with the camera resolution – replacing a one-megapixel camera in the current set up with a two-megapixel camera would result in twice the resolution in both in-plane and transverse displacement. With higher transverse displacement resolution, adhesion range extraction may be possible with the BCT. Using the contact radius that is extracted optically, the displacement fields can be fitted to extract an adhesion range between the contact pair.

In the BCT set up, the electronic pressure regulator limits the applied pressure and the pressure must range between 2 kPa and 20 kPa. This can be challenging for testing soft materials such as Sylgard 527, an alternate PDMS formulation used in some cell adhesion experiments [133], and Ecoflex, a popular elastomer for fabricating flexible electronics [134]. These materials typically undergo very large deformation at applied pressures below 6 kPa. To be able to characterize these types of samples successfully, a different electronic pressure regulator with a lower pressure range is recommended. Alternatively, the sample radius can be reduced to increase the effective stiffness of the specimen. In the bulge test, the deflection scales with the radius to the fourth power, based on CPT. Reducing the sample radius from 10 mm to 5 mm effectively reduces the deflection by 16 times, or increases the applied pressure by 16 times. This is an effective method to modify the BCT experiment without significant investment. However, the relative optical resolution is reduced with a smaller blister size.

7.3.2 Mechanics model for shear-corrected plate theory

Specimens with low modulus used in the BCT often have larger thicknesses as a compensation to achieve reasonable flexural rigidity. As a result, shear stresses are significant in these types of specimens. In Chapter 4, specimens that have significant shear stresses are analyzed using FE analyses. To improve the speed of the BCT analyses, a plate theory with shear correction may be implemented. Traditionally, Mindlin plate theory [135] is used to model shear-enhanced plates. In this theory, a shear correction factor is used as the shape of shear stress distribution is not compatible. At this point, it is unclear how adhesion influences this shear correction factor in the BCT. Alternatively, a third-order shear corrected plate theory [100] can be solved without the assumption of the shear correction factor. A compatible shear stress distribution is assumed in this theory. In either case, the shear stress must be accounted for in the adhesion contact cases. A similar boundary condition suggested in [101] may be sufficient, but special care must be taken to ensure the mechanics model is properly derived.

CHAPTER 8: APPENDIX

Two MATLAB functions are included here. The first one, `vKPT_BCT`, is used to solve the BCT problem using the vKPT mechanics model (Chapter 3). If parameters related to adhesion are not defined in the input, then the BT case is solved. Otherwise, the MD-type adhesion law is adopted if an adhesion range is given or the JKR-type adhesion model is used if there is no adhesion range.

The second function, `BCT_FE_Simulation`, is used to solve the BCT problem using FE analysis (Chapter 3). The function first generates an input (.inp) file and is sent to ABAQUS for execution. Depending on the inputs, a user subroutine (.sub) file may also be generated to model a traction-separation relationship. The output data is extracted by executing a python (.py) script that reads full precision data directly from the output database (.odb) file.

8.1 MATLAB code for solving the vKPT BCT

```
function [q, b, G, w0, Ur, Uz, BVP_Solution, ContactMode] = vKPT_BCT(vKStats,
z, r)
% [q, b, G, w0, Ur, Uz, BVP_Solution, ContactMode] = vKPT_BCT(vKStats, z, r)
% Input parameter list in structure form
% Normalized parameters: Nu, k, P, z, kR, kT
%            Nu: Poisson's ratio
%           Tau: Pre-stress                 sqrt(12*(1-Nu^2)*s0*R^2/(Es*h^2))
%             P: Pressure                   q*R^4/(Es*h^4)
%             b: Contact radius             b/R
%         delta: Gap                        delta/h
%            kR: Radial spring              kR_d*R/(Es*h)
%            kT: Torsion spring             kT_d*R/(Es*h^3/(12*(1-Nu^2)))
%             G: Strain energy release rate G*R^4/(Es*h^5)
%         d_adh: Adhesion range             d_adh/h
%           Ur0: Prescribed stretch         Ur0/h
% Dimensional parameters: q, Es, sigma_0, Nu, h, R, z, kR, kT
%             q: Pressure                   [Pa]
```

```
%            Es: Young's modulus            [Pa]
%       sigma_0: Pre-stress                 [Pa]
%            Nu: Poisson's ratio            [-]
%             h: Thickness                  [m]
%             R: Radius                     [m]
%             z: z-position                 [m]
%          kR_d: Radial spring              [Pa]
%          kT_d: Torison spring             [N/rad]
%         d_adh: Adhesion range             [m]
%             G: Strain energy release rate [J/m^2]
%           Ur0: Prescribed stretch         [m]
%==========================================================================
% Solved system of equations y in BVP_Solution
%   y(1) - w        - Axial displacement
%   y(2) - w'
%   y(3) - w''
%   y(4) - w'''
%   y(5) - Sr       - Radial force (Nr*R^2/(Es*h^3))
%   y(6) - Sr'
%==========================================================================
% ContactMode - | None | Hertz_b | Hertz_q | JKR | MD | DMT |
%==========================================================================
%
% v1.0 - 05/21/2016
%   Changed system of ODE to include w
% v1.1 - 05/27/2016
%   Clean up code
%   MD part in progress
% v2.0 - 10/20/2016
%   Clean up code
% v3.0 - 11/23/2016
%   Added prescribed stretch for no-slip model

[Nu, Tau, b, P, kT, kR, r, delta, d_adh, G, h, R, Es, Ur0, ContactMode] =
Setup_Params(vKStats, r);
s_adh = 0;
BVPOptions = bvpset('RelTol', 1e-6, 'AbsTol', 1e-6, 'NMax', 50000, 'Stats',
'off', 'Vectorized', 'on');
% disp(ContactMode);

nBias = 5; % Node bias (using error function) towards edge
% BVP types
switch ContactMode
    case 'None'
        % Specify q
        % Output w0, b = G = 0
        b = 1e-7;
        x0 = MakeGrid([b,1],201,'bias');
        BVP_Initial = bvpinit(x0, @InitialSolution);
        BVP_Solution = bvp4c(@ODE_OneRegion, @BC_BT, BVP_Initial, BVPOptions);
        G = nan;
    case 'Hertz_q'
        % Specify delta, b
        % Optimize delta = Uz(b) by varying q at fixed b
        % Output q, w0 = delta, G = 0
        P = 1; % Initialize P
        optoptions = optimoptions('lsqnonlin', 'Display', 'Off');
```

```
        P = lsqnonlin(@(q)Optimize_BVP_OneRegion(q,ContactMode),
16*delta/(3*(1-Nu^2)), 0, inf, optoptions); % Optimize and update P
        x0 = MakeGrid([b,1],201,'bias');
        BVP_Initial = bvpinit(x0, @InitialSolution);
        BVP_Solution = bvp4c(@ODE_OneRegion, @BC_BCT_OneRegion, BVP_Initial,
BVPOptions);
        G = 0;
    case 'Hertz_b'
        % Specify delta, q
        % Optimize delta = Uz(b) by varying b at fixed q
        % Output b, w0 = delta, G = 0
        b = 0.1; % Initialize b
        optoptions = optimoptions('lsqnonlin', 'Display', 'Off'); % iter-
detailed
        b = lsqnonlin(@(b)Optimize_BVP_OneRegion(b,ContactMode), 0.1, 1e-7,
0.9, optoptions); % Optimize and update b
        x0 = MakeGrid([b,1],201,'bias');
        BVP_Initial = bvpinit(x0, @InitialSolution);
        BVP_Solution = bvp4c(@ODE_OneRegion, @BC_BCT_OneRegion, BVP_Initial,
BVPOptions);
        G = 0;
    case 'JKR_q'
        % Specify delta, b, G
        % Output q, w0 = delta
        P = 0.1; % Initialize q
        optoptions = optimoptions('lsqnonlin', 'Display', 'Off');
        Pmax = lsqnonlin(@(q)Optimize_BVP_OneRegion(q,'Hertz_q'),
16*delta/(3*(1-Nu^2)), 0, inf, optoptions); % Set maximum P
        optoptions = optimset('Display', 'Off');
        P = fzero(@(q)Optimize_BVP_OneRegion(q,ContactMode), [-2,1]*Pmax,
optoptions);
        x0 = MakeGrid([b,1],201,'bias');
        BVP_Initial = bvpinit(x0, @InitialSolution, G);
        BVP_Solution = bvp4c(@ODE_OneRegion, @BC_BCT_OneRegion, BVP_Initial,
BVPOptions);
    case 'JKR_b'
        % Specify delta, q, G
        % Output b, w0 = delta
        optoptions = optimoptions('lsqnonlin', 'Display', 'Off');
        b0 = lsqnonlin(@(b)Optimize_BVP_OneRegion(b,'Hertz_b'), 0.1, 1e-7, 0.9,
optoptions); % Optimize and update b0 to set lower bound
        b = lsqnonlin(@(b)Optimize_BVP_OneRegion(b,ContactMode), (b0+0.9)/5,
b0, 0.9, optoptions); % Optimize and update b
        x0 = MakeGrid([b,1],201,'bias');
        BVP_Initial = bvpinit(x0, @InitialSolution, G);
        BVP_Solution = bvp4c(@ODE_OneRegion, @BC_BCT_OneRegion, BVP_Initial,
BVPOptions);
    case 'JKR_G'
        % Specify delta, q, b
        % Output G, w0 = delta
        x0 = MakeGrid([b,1],201,'bias');
        BVP_Initial = bvpinit(x0, @InitialSolution, 1);
        BVP_Solution = bvp4c(@ODE_OneRegion, @BC_BCT_OneRegion, BVP_Initial,
BVPOptions);
        G = BVP_Solution.parameters;
    case 'MD_q'
        % Specify delta, b, G, d_adh
        % Optimize G = sigma_adh*d_adh by varying q at fixed b and G
```

```
        % Output G, w0 = delta
        optoptions = optimoptions('lsqnonlin', 'Display', 'off');
        Pmax = lsqnonlin(@(q)Optimize_BVP_OneRegion(q,'Hertz_q'),
16*delta/(3*(1-Nu^2)), 0, inf, optoptions); % Set maximum P
        optoptions = optimoptions('fmincon', 'Display', 'off', 'Algorithm',
'sqp');
        x = fmincon(@(x)0, [0.05,Pmax*0.8], [], [], [], [], [1e-4,-Pmax*2],
[0.9,Pmax], @(x)deal([],Optimize_BVP_TwoRegions(x,ContactMode,1000)),
optoptions);
        b_adh = x(1)*(1-b);
        P = x(2);
        x0 = [MakeGrid([b,b+b_adh],201,'bias'),
MakeGrid([b+b_adh,1],201,'bias')];
        BVP_Initial = bvpinit(x0, @InitialSolution_MD, 1000);
        BVP_Solution = bvp4c(@ODE_TwoRegions, @BC_BCT_TwoRegions, BVP_Initial,
BVPOptions);
    case 'MD_b'
        % Specify delta, q, G, d_adh
        % Optimize G = sigma_adh*d_adh by varying b at fixed q and G
        % Output G, w0 = delta
        optoptions = optimoptions('fmincon', 'Display', 'off', 'Algorithm',
'sqp');
        x = fmincon(@(x)0, [1,1]*0.1, [], [], [], [], [1,1]*1e-7, [0.9,0.9],
@(x)deal([],Optimize_BVP_TwoRegions(x,ContactMode,1000)), optoptions);
        b = x(2);
        b_adh = x(1)*(1-b);

        x0 = [MakeGrid([b,b+b_adh],201,'bias'),
MakeGrid([b+b_adh,1],201,'bias')];
        BVP_Initial = bvpinit(x0, @InitialSolution_MD, 1000);
        BVP_Solution = bvp4c(@ODE_TwoRegions, @BC_BCT_TwoRegions, BVP_Initial,
BVPOptions);
    case 'MD_G'
        % Specify delta, q, b, d_adh
        % Optimize b_adh by varying d_adh = Uz(b+b_adh) at fixed q and b
        % Output G, w0 = delta
        optoptions = optimoptions('lsqnonlin', 'Display', 'off');
        b_adh = lsqnonlin(@(x)Optimize_BVP_TwoRegions(x,ContactMode,1000), (1-
b)/5, 0, 1-b, optoptions); % Optimize and update b0 to set lower bound

        x0 = [MakeGrid([b,b+b_adh],201,'bias'),
MakeGrid([b+b_adh,1],201,'bias')];
        BVP_Initial = bvpinit(x0, @InitialSolution_MD, 1);
        BVP_Solution = bvp4c(@ODE_TwoRegions, @BC_BCT_TwoRegions, BVP_Initial,
BVPOptions);
        G = BVP_Solution.parameters;
    case 'DMT_q'
        % Specify delta, b
        % Optimize delta = Uz(b) by varying q at fixed b
        % Output q, w0 = delta, G = 0
        P = 1; % Initialize P
        s_adh = G/delta;
        optoptions = optimoptions('lsqnonlin', 'Display', 'Off');
        P = lsqnonlin(@(q)Optimize_BVP_OneRegion(q,ContactMode), 1, 0, inf,
optoptions); % Optimize and update P
        x0 = MakeGrid([b,1],201,'bias');
        BVP_Initial = bvpinit(x0, @InitialSolution);
```

```
        BVP_Solution = bvp4c(@ODE_OneRegion, @BC_BCT_OneRegion, BVP_Initial,
BVPOptions);
    case 'DMT_b'
        % Specify delta, q
        % Optimize delta = Uz(b) by varying b at fixed q
        % Output b, w0 = delta, G = 0
        b = 0.1; % Initialize b
        s_adh = G/delta;
        optoptions = optimoptions('lsqnonlin', 'Display', 'Off');
        b = lsqnonlin(@(b)Optimize_BVP_OneRegion(b,ContactMode), 0.1, 1e-7,
0.9, optoptions); % Optimize and update b
        x0 = MakeGrid([b,1],201,'bias');
        BVP_Initial = bvpinit(x0, @InitialSolution);
        BVP_Solution = bvp4c(@ODE_OneRegion, @BC_BCT_OneRegion, BVP_Initial,
BVPOptions);
    case 'DMT_G'
        % Specify delta, q, b, d_adh = delta
        % Optimize delta = Uz(b) by varying G = sigma_adh*d_adh at fixed q and
b
        % Output G, w0 = delta
        optoptions = optimoptions('lsqnonlin', 'Display', 'Off');
        G = lsqnonlin(@(G)Optimize_BVP_OneRegion(G,ContactMode), 1, 0, inf,
optoptions); % Optimize and update G
        x0 = MakeGrid([b,1],201,'bias');
        BVP_Initial = bvpinit(x0, @InitialSolution_MD);
        BVP_Solution = bvp4c(@ODE_OneRegion, @BC_BCT_OneRegion, BVP_Initial,
BVPOptions);
end

% Get displacement fields (dimensionalized)
x0 = linspace(b, 1, 1001);
y = deval(BVP_Solution, x0);
for ii=numel(z):-1:1
    % Ur(r>b)/h = h/R*r*(r*Sr'+(1-Nu)*Sr) + z/h*theta*h^2/R
    % Ur(r<b)/h = h^2/R*(1-Nu)*Sr*r
    Ur2(:,ii) = h^2/R*x0.*(x0.*y(6,:)+(1-Nu)*y(5,:)) - z(ii)*y(2,:)*h/R;
    Ur_0 = Ur2(1,ii);
    Ur(:,ii) = interp1(x0, Ur2(:,ii), r/R);
    Ur(r/R<b,ii) = Ur_0*r(r/R<b)/R/b;
    w0(ii) = y(1,1)*h;
    Uz(:,ii) = interp1(x0, y(1,:)*h, r/R);
    Uz(r/R<b,ii) = w0(ii);
end

% Dimensionalize output parameters
q = P/R^4*(Es*h^4);
b = b*R;
G = G/R^4*(Es*h^5);

    function y = MakeGrid(x, nNodes, Type)
        switch lower(Type)
            case 'linear'
                y = linspace(min(x), max(x), nNodes);
            case 'bias'
                y_linear = linspace(min(x), max(x), nNodes);
                y = erf(nBias*((y_linear-min(y_linear))/range(y_linear)-0.5));
                y = (y-min(y))/range(y);
                y = y*range(y_linear)+min(y_linear);
```

```
        end
    end
%%
    function residual = Optimize_BVP_OneRegion(x, Type)
        switch Type
            case {'Hertz_q', 'JKR_q', 'DMT_q'}
                P = x;
            case {'Hertz_b', 'JKR_b', 'DMT_b'}
                b = x;
            case 'DMT_G'
                G = x;
                s_adh = G/delta;
        end
        x0_2 = MakeGrid([b,1],101,'bias');
        switch Type
            case {'Hertz_q', 'Hertz_b'}
                BVP_Initial_2 = bvpinit(x0_2, @InitialSolution);
                BVP_Solution_2 = bvp4c(@ODE_OneRegion, @BC_BCT_OneRegion,
BVP_Initial_2, BVPOptions);
                Uz_2 = deval(BVP_Solution_2, x0_2, 1);
                residual = max(Uz_2) - delta;
            case {'JKR_q', 'JKR_b'}
                BVP_Initial_2 = bvpinit(x0_2, @InitialSolution, G);
                BVP_Solution_2 = bvp4c(@ODE_OneRegion, @BC_BCT_OneRegion,
BVP_Initial_2, BVPOptions);
                residual = G - BVP_Solution_2.parameters;
            case {'DMT_q', 'DMT_b', 'DMT_G'}
                BVP_Initial_2 = bvpinit(x0_2, @InitialSolution);
                BVP_Solution_2 = bvp4c(@ODE_OneRegion, @BC_BCT_OneRegion,
BVP_Initial_2, BVPOptions);
                Uz_2 = deval(BVP_Solution_2, x0_2, 1);
                residual = max(Uz_2) - delta;
        end
    end
%%
    function residual = Optimize_BVP_TwoRegions(x, Type, InitialGuess)
        switch Type
            case 'MD_q'
                b_adh2 = x(1)*(1-b);
                P = x(2);
            case 'MD_b'
                b = x(2);
                b_adh2 = x(1)*(1-b);
            case 'MD_G'
                b_adh2 = x(1);
        end
        x0_2 = [MakeGrid([b,b+b_adh2],101,'bias'),
MakeGrid([b+b_adh2,1],101,'bias')];
        BVP_Initial_2 = bvpinit(x0_2, @InitialSolution_MD, InitialGuess);
        BVP_Solution_2 = bvp4c(@ODE_TwoRegions, @BC_BCT_TwoRegions,
BVP_Initial_2, BVPOptions);
        residual(1) = delta - BVP_Solution_2.y(1,BVP_Solution_2.x(1:end-
1)==BVP_Solution_2.x(2:end)) - d_adh;
        switch Type
            case 'MD_G'
            otherwise
                residual(2) = BVP_Solution_2.parameters - G;
        end
```

```
    end

%% ODE_OneRegion
function dydx = ODE_OneRegion(x,y,~)
%================
%   y(1) - w
%   y(2) - w'
%   y(3) - w''
%   y(4) - w'''
%   y(5) - Sr
%   y(6) - Sr'
%================
dydx = [
    y(2,:)
    y(3,:)
    y(4,:)
    Tau^2*(y(2,:)./x+y(3,:)) + 12*(1-
Nu^2)*(y(5,:).*(y(2,:)./x+y(3,:))+y(2,:).*y(6,:)+(P+s_adh)) - (2*y(4,:)./x-
y(3,:)./x.^2+y(2,:)./x.^3)
    y(6,:)
    -y(2,:).^2./(2*x.^2) - 3*y(6,:)./x
    ];
end

%% ODE_TwoRegions
function dydx = ODE_TwoRegions(x,y,region,varargin)
%================
%   y(1) - w
%   y(2) - w'
%   y(3) - w''
%   y(4) - w'''
%   y(5) - Sr
%   y(6) - Sr'
%================
if numel(varargin)==1
    s_adh = varargin{1}/d_adh;
end
dydx = [
    y(2,:)
    y(3,:)
    y(4,:)
    y(4,:)*nan
    y(6,:)
    -y(2,:).^2./(2*x.^2) - 3*y(6,:)./x
    ];
switch region
    case 1
        dydx(4,:) = Tau^2*(y(2,:)./x+y(3,:)) + 12*(1-
Nu^2)*(y(5,:).*(y(2,:)./x+y(3,:))+y(2,:).*y(6,:)+(P+s_adh)) - (2*y(4,:)./x-
y(3,:)./x.^2+y(2,:)./x.^3);
    case 2
        dydx(4,:) = Tau^2*(y(2,:)./x+y(3,:)) + 12*(1-
Nu^2)*(y(5,:).*(y(2,:)./x+y(3,:))+y(2,:).*y(6,:)+P) - (2*y(4,:)./x-
y(3,:)./x.^2+y(2,:)./x.^3);
end
end

%% BC_BT
```

```
function residual = BC_BT(ya,yb)
%================ r = b
% 1) w'(b) = 0
% 2) w'''(b) + w''(b)/b - w'(b)/b^2 = 0 (Shear vanishes)
% 3) Sr'(b) = 0
%================ r = 1
% 4) w(1) = 0
% 5 a) w'(1) = 0
% 5 b) w''(1) + (Nu+kT)*w'(1) = 0
% 6 a) Sr'(1) + (1-Nu)*Sr(1) = 0
% 6 b) Sr'(1) + (1/kR+(1-Nu))*Sr(1) = 0
%================
%   y(1) - w
%   y(2) - w'
%   y(3) - w''
%   y(4) - w'''
%   y(5) - Sr
%   y(6) - Sr'
%================
residual = [
    %================ r = b
    ya(2,:)
    ya(4,:) + ya(3,:)/b
    ya(6,:)
    %================ r = 1
    yb(1,:)                                          % 4) w(1) = 0
    yb(2,:)                                          % 5 a) w'(1) = 0
    yb(6,:) + (1-Nu)*yb(5,:)                         % 6 a) Sr'(1) + (1-Nu)*Sr(1) =
0
    ];
if kT<inf % Torsion spring
    residual(5,:) = yb(3,:)+(Nu+kT)*yb(2,:);         % 5 b) w''(1) +
(Nu+kT)*w'(1) = 0
end
if kR<inf % Linear spring
    residual(6,:) = yb(6,:) + ((1-Nu)+1/kR)*yb(5,:); % 6 b) Sr'(1) + (1/kR+(1-
Nu))*Sr(1) = 0
end
end

%%
function residual = BC_BCT_OneRegion(ya,yb,varargin)
%================ r = b
% 0) w(b) = delta
% 1) w'(b) = 0
% 2) w''(b) + w'(b)/b = G (Moment vanishes)
% 3) Sr'(b) = 0
%================ r = 1
% 4) w(1) = 0
% 5 a) w'(1) = 0
% 5 b) w''(1) + (Nu+kT)*w'(1) = 0
% 6 a) Sr'(1) + (1-Nu)*Sr(1) = 0
% 6 b) Sr'(1) + (1/kR+(1-Nu))*Sr(1) = 0
%================
%   y(1) - w
%   y(2) - w'
%   y(3) - w''
%   y(4) - w'''
```

```
%   y(5) - Sr
%   y(6) - Sr'
%================
residual = [
    %================ r = b
    ya(2,:)                                                 % 1) w'(b) = 0
    ya(3,:)                                                 % 2) w''(b) + w'(b)/b =
0 (Moment vanishes)
    ya(6,:)                                                 % 3) Sr'(b) = 0
    %================ r = 1
    yb(1,:)                                                 % 4) w(1) = 0
    yb(2,:)                                                 % 5 a) w'(1) = 0
    yb(6,:) + (1-Nu)*yb(5,:)                                % 6 a) Sr'(1) + (1-
Nu)*Sr(1) = 0
    ];
if kT<inf % Torsion spring
    residual(5,:) = yb(3,:)+(Nu+kT)*yb(2,:);                % 5 b) w''(1) +
(Nu+kT)*w'(1) = 0
end
if kR<inf % Linear spring
    residual(6,:) = yb(6,:) + ((1-Nu)+1/kR)*yb(5,:);        % 6 b) Sr'(1) +
(1/kR+(1-Nu))*Sr(1) = 0
end
if Ur0~=0 % Prescribed radial displacement
    residual(3,:) = (ya(6,:)*b^2 + (1-Nu)*ya(5,:)*b)*h/R - Ur0;
end
switch numel(varargin)
    case 1 % Adhesive boundary condition
        residual(2:end+1,:) = residual(1:end,:);
        residual(1,:) = ya(1,:) - delta;                        % 0) w(b) = delta
        residual(3,:) = ya(3,:).^2/(24*(1-Nu^2)) - varargin{1};         % 2)
(w''(b)+Nu*w'(b)/b)^2/(24*(1-Nu^2)) + Sr(b)^2*(1-Nu^2)/2 - G = 0
%         if Ur0~=0
%             residual(3,:) = ya(3,:).^2/(24*(1-Nu^2)) + ya(5,:).^2*(1-Nu^2)/2
- varargin{1};       % 2) (w''(b)+Nu*w'(b)/b)^2/(24*(1-Nu^2)) + Sr(b)^2*(1-
Nu^2)/2 - G = 0
%         else
%             residual(3,:) = ya(3,:).^2/(24*(1-Nu^2)) - varargin{1};       %
2) (w''(b)+Nu*w'(b)/b)^2/(24*(1-Nu^2)) - G = 0
%         end
end
end

%%
function residual = BC_BCT_TwoRegions(ya,yb,varargin)
%================ r = b
% 1) w(b) = delta
% 2) w'(b) = 0
% 3) w''(b) + Nu/b*w'(b) = 0 (Moment vanishes)
% 4) Sr'(b) = 0
%================ r = b + b_adh
% 5) w(b+b_adh) continuous
% 6) w'(b+b_adh) continuous
% 7) w''(b+b_adh) continuous
% 8) w'''(b+b_adh) continuous
% 9) Sr(b+b_adh) continuous
% 10) Sr'(b+b_adh) continuous
%================ r = 1
```

```
% 11) w(1) = 0
% 12 a) w'(1) = 0
% 12 b) w''(1) + (Nu+kT)*w'(1) = 0
% 13 a) Sr'(1) + (1-Nu)*Sr(1) = 0
% 13 b) Sr'(1) + (1/kR+(1-Nu))*Sr(1) = 0
%=================
%   y(1) - w
%   y(2) - w'
%   y(3) - w''
%   y(4) - w'''
%   y(5) - Sr
%   y(6) - Sr'
%=================
residual = [
    %================= r = b
    ya(1,1) - delta                                 % 1) w(b) = delta
    ya(2,1)                                         % 2) w'(b) = 0
    ya(3,1)                                         % 3) w''(b) + Nu/b*w'(b) = 0
(Moment vanishes)
    ya(6,1)                                         % 4) Sr'(b) = 0
    %================= r = b + b_adh
    ya(1,2) - yb(1,1)                               % 5) w(b+b_adh) continuous
    ya(2,2) - yb(2,1)                               % 6) w'(b+b_adh) continuous
    ya(3,2) - yb(3,1)                               % 7) w''(b+b_adh) continuous
    ya(4,2) - yb(4,1)                               % 8) w'''(b+b_adh) continuous
    ya(5,2) - yb(5,1)                               % 9) Sr(b+b_adh) continuous
    ya(6,2) - yb(6,1)                               % 10) Sr'(b+b_adh) continuous
    %================= r = 1
    yb(1,2)                                         % 11) w(1) = 0
    yb(2,2)                                         % 12 a) w'(1) = 0
    yb(6,2) + (1-Nu)*yb(5,2)                        % 13 a) Sr'(1) + (1-Nu)*Sr(1) =
0
    ];
if kT<inf % Torsion spring
    residual(12) = yb(3,2)+(Nu+kT)*yb(2,2);         % 12 b) w''(1) +
(Nu+kT)*w'(1) = 0
end
if kR<inf % Linear spring
    residual(13) = yb(6,2) + ((1-Nu)+1/kR)*yb(5,2); % 13 b) Sr'(1) + (1/kR+(1-
Nu))*Sr(1) = 0
end
if Ur0~=0 % Prescribed radial displacement
    residual(4) = (ya(6,1)*b^2 + (1-Nu)*ya(5,1)*b)*h/R - Ur0;
end
end
%% InitialSolution_MD
    function v = InitialSolution_MD(x,~)
        v = [
            1
            -sin(pi*x)
            -0.68
            1
            1
            1
            ];
    end
%% InitialSolution
    function y_init = InitialSolution(x)
```

```
        switch ContactMode
            case {'None', 'Hertz_q', 'Hertz_b'}
                y_init = [
                    4.22505802320866 + 0.00235483981737092.*P +
0.00413688049019489.*Tau.^2.*x.^2 + 2.07685271635051e-7.*P.^2.*x.^2 -
2.07685271635051e-7.*P.^2 - 0.00413688049019489.*Tau.^2 -
0.429222318601614.*x.^3 - 4.22505802320866.*x.^2 - 0.00235483981737092.*P.*x.^2
                    2.24328228943419 + 0.125525171340784.*Tau.*x +
10.8887739755353.*x.^22.4392854051475 +
0.00360845252857989.*P.*x.^33.3964664181967 - 13.1159219008074.*x -
2.24328228943419.*(0.00175771846077752.*P).^x
                    0.00512953485789494.*Tau.^2 + 3.90524054694194e-11.*P.^3 +
9.68657475034975e-7.*x.*P.^2 + sqrt(0.00512953485789494.*x.*Tau.^3 +
9.68657475034975e-7.*x.*P.^2) - 9.4813772977615 - 0.00312259634419969.*P -
0.00778657757386713.*P.*x
                    2.73496746169758e-13./x.^3 +
(1.52656010996839.*x).^21.8914830884045 - 0.0217089552959753.*P.*x.^2
                    6.89670382604281 + 0.0788611681526172.*P +
0.0128822438976647.*x.*Tau.^2 - 0.0657110167117835.*Tau.^2 -
0.00659244583560794.*P.*log(P) - 0.00499790217780969.*P.*x.^2 -
1.3418123808989.*x.*5.56953968680206.^x
                    0.0337731569779024.*x.*Tau.^2 + 8.81487741531761e-
7.*x.*P.^2 - 9.21337110962305.*x - 0.0114522007314549.*P.*x -
0.00530243292295085.*P.*x.^2
                    ];
            otherwise
                y_init = [
                    1
                    -sin(pi*x)
                    -0.68
                    1
                    1
                    1
                    ];
        end
    end
end

%% Setup_Params
function [Nu, Tau, b, P, kT, kR, r, delta, d_adh, G, h, R, Es, Ur0,
ContactMode] = Setup_Params(vKStats, r)
% Initialize parameters that may not be supplied
if ~isfield(vKStats, 'delta')
    vKStats.delta = [];
end
if ~isfield(vKStats, 'b')
    vKStats.b = [];
elseif isnan(vKStats.b)
    vKStats.b = [];
    vKStats.d_adh = 0;
end
if isfield(vKStats, 'P') && ~isfield(vKStats, 'q')
    vKStats.q = nan;
elseif ~isfield(vKStats, 'P') && isfield(vKStats, 'q')
    vKStats.P = [];
elseif ~isfield(vKStats, 'P') && ~isfield(vKStats, 'q')
    vKStats.q = [];
    vKStats.P = [];
```

```
end
if ~isfield(vKStats, 'G')
    vKStats.G = [];
elseif vKStats.G==0 % Convert to Hertz-type contact
    vKStats.G = [];
    vKStats.d_adh = 0;
end
if ~isfield(vKStats, 'd_adh')
    vKStats.d_adh = 0;
elseif isempty(vKStats.d_adh) || isnan(vKStats.d_adh)
    vKStats.d_adh = 0;
end
if ~isfield(vKStats, 'kR') || isnan(vKStats.kR)
    vKStats.kR = inf;
end
if ~isfield(vKStats, 'kT') || isnan(vKStats.kR)
    vKStats.kT = inf;
end
if ~isfield(vKStats, 'Ur0') || isnan(vKStats.Ur0)
    vKStats.Ur0 = 0;
end

if     ~isempty(vKStats.q) &&  isempty(vKStats.b) &&  isempty(vKStats.delta) &&
isempty(vKStats.G) &&  vKStats.d_adh==0
    ContactMode = 'None';
elseif ~isempty(vKStats.q) &&  isempty(vKStats.b) && ~isempty(vKStats.delta) &&
isempty(vKStats.G) &&  vKStats.d_adh==0
    ContactMode = 'Hertz_b';
elseif  isempty(vKStats.q) && ~isempty(vKStats.b) && ~isempty(vKStats.delta) &&
isempty(vKStats.G) &&  vKStats.d_adh==0
    ContactMode = 'Hertz_q';
elseif  isempty(vKStats.q) && ~isempty(vKStats.b) && ~isempty(vKStats.delta) &&
~isempty(vKStats.G) &&  vKStats.d_adh==0
    ContactMode = 'JKR_q';
elseif ~isempty(vKStats.q) &&  isempty(vKStats.b) && ~isempty(vKStats.delta) &&
~isempty(vKStats.G) &&  vKStats.d_adh==0
    ContactMode = 'JKR_b';
elseif ~isempty(vKStats.q) && ~isempty(vKStats.b) && ~isempty(vKStats.delta) &&
isempty(vKStats.G) &&  vKStats.d_adh==0
    ContactMode = 'JKR_G';
elseif  isempty(vKStats.q) && ~isempty(vKStats.b) && ~isempty(vKStats.delta) &&
~isempty(vKStats.G) &&  vKStats.d_adh<vKStats.delta
    ContactMode = 'MD_q';
elseif ~isempty(vKStats.q) &&  isempty(vKStats.b) && ~isempty(vKStats.delta) &&
~isempty(vKStats.G) &&  vKStats.d_adh<vKStats.delta
    ContactMode = 'MD_b';
elseif ~isempty(vKStats.q) && ~isempty(vKStats.b) && ~isempty(vKStats.delta) &&
isempty(vKStats.G) &&  vKStats.d_adh<vKStats.delta
    ContactMode = 'MD_G';
elseif  isempty(vKStats.q) && ~isempty(vKStats.b) && ~isempty(vKStats.delta) &&
~isempty(vKStats.G) &&  vKStats.d_adh>=vKStats.delta
    vKStats.d_adh = vKStats.delta;
    ContactMode = 'DMT_q';
elseif ~isempty(vKStats.q) &&  isempty(vKStats.b) && ~isempty(vKStats.delta) &&
~isempty(vKStats.G) &&  vKStats.d_adh>=vKStats.delta
    vKStats.d_adh = vKStats.delta;
    ContactMode = 'DMT_b';
```

```
elseif ~isempty(vKStats.q) && ~isempty(vKStats.b) && ~isempty(vKStats.delta) &&
isempty(vKStats.G) &&  vKStats.d_adh>=vKStats.delta
    vKStats.d_adh = vKStats.delta;
    ContactMode = 'DMT_G';
else
    error('Unknown contact mode.');
end

if isfield(vKStats, 'Tau') % Normalized parameters
    Nu = vKStats.Nu;
    Tau = vKStats.Tau;

    P = vKStats.P;
    b = vKStats.b;
    delta = vKStats.delta;
    G = vKStats.G;
    d_adh = vKStats.d_adh;
    kT = vKStats.kT;
    kR = vKStats.kR;
    Ur0 = vKStats.Ur0;

    h = 1;
    R = 1;
    Es = 1;
else % Dimensional parameters
    Es = vKStats.Es;
    s0 = vKStats.sigma_0;
    Nu = vKStats.Nu;
    h = vKStats.h;
    R = vKStats.R;

    q = vKStats.q;
    b = vKStats.b;
    delta = vKStats.delta;
    G = vKStats.G;
    d_adh = vKStats.d_adh;
    kT_d = vKStats.kT;
    kR_d = vKStats.kR;
    Ur0_d = vKStats.Ur0;

    % Normalize parameters
    Tau = sqrt(12*(1-Nu^2)*s0*R^2/(Es*h^2));
    kR = kR_d*R/(Es*h);
    kT = kT_d*R/(Es*h^3/(12*(1-Nu^2)));
    P = q*R^4/(Es*h^4);
    G = G*R^4/(Es*h^5);
    b = b/R;
    delta = delta/h;
    d_adh = d_adh/h;
    Ur0 = Ur0_d/h;
end

if iscolumn(r)
    r = r';
end
end
```

8.2 MATLAB code for solving the ABAQUS FE model

```
function varargout = BCT_FE_Simulation(varargin)
% [b, q, t, w0, X, dX, J] = BCT_FE_Simulation(Exp, density, fname)
% ================================ Inputs ================================
% Exp       - Es, Nu, h, R, delta, q, kT, sigma_0
% density   - [R_elements, h_elements, ElementType]
% fname     - File name
% ================================ Outputs ================================
% b         - Contact radius
% q         - Pressure
% t         - Time
% w0        - Center axial displacement
% X         -
% dX        -
% J         - J-integral (for ContactModel: JKR only)
% ================================ Exp ================================
% Exp.Es = [4e9, 1e6]; % Young's modulus
% Exp.Nu = [0.3, 0.5]; % Poisson's ratio
% Exp.h = [50e-6, 10e-6]; % Thickness
% Exp.R = 10e-3; % Radius
% Exp.delta = 0.4e-3; % Gap
% Exp.kT = nan; % Compliant boundary
% Exp.sigma_0 = 0; % Prestress
%
% Exp.ViscoType = 'Prony'; % | Prony | Modulus |
% Exp.Visco = []; % Viscoelastic parameters for film | Modulus: [Re(g*),
Im(g*), Re(k*), Im(k*), freq] | Prony: [g, k, tau]
%
% Exp.ContactModel = 'Hertz'; % | JKR | MD | LJ | Hertz | None |
% Exp.Frictionless = true;
% Exp.FrictionCoefficient = inf; % (Frictionless) 0 < FrictionCoefficient < inf
(No slip)
% Exp.G = 0.1;
% Exp.delta_adh = 1e-6;
%
% Exp.q = 8000; % Applied pressure
% Exp.t = 1; % Time for each pressure step
% Exp.ActiveAdhesion = 1;
% Exp.StepSize = 0.05; % 1e-5 < t < 1
% Exp.StepContinue = false;
%
% Exp.StepType = 'Static'; % | Static | Riks | Stabilize | Visco | Direct
% Exp.FEName = 'BCT_MD_Test';
% Exp.OutputData = 'All'; % | All | Final | Step
% Exp.AnalysisType = 'SimulationAnalysis'; % | Simulation | Analysis |
SimulationAnalysis |
% Exp.ConvertUnits = 'kg|m|s'; % | mg|um|s | g|mm|s | kg|m|s
% Exp.WriteFrequency = 1; % Integer, >= 1
%
% Exp.ALLSDTOL = 0.05; % Adaptive automatic stabilization parameter (default:
0.05)
% Exp.StablizeEnergy = 2e-4; % Automatic stabilization value for dissipated
energy fraction (default: 2e-4)
% Exp.DispControls = [5e-3, 1e-2, 1e-8];
```

```
% % 1.1. Ratio of the largest residual to the corresponding average flux norm
for convergence
% % 1.2. Ratio of the largest solution correction to the largest corresponding
incremental solution value
% % 2.3. Criterion for zero displacement increment (and/or zero penetration if
CONVERT SDI=YES)
% %      compared to the characteristic element length in the model. (Default:
1e-8)
% Exp.TimeControls = [4, 10, 4, 5];
% % 1. number of equilibrium iterations (without severe discontinuities) after
% %    which the check is made whether the residuals are increasing in two
% %    consecutive iterations (Default: 4)
% % 5. number of consecutive equilibrium iterations (without severe
discontinuities)
% %    above which the size of the next increment will be reduced (Default: 10)
% % 6. maximum number of consecutive equilibrium iterations (without severe
discontinuities)
% %    allowed in consecutive increments for the time increment to be
% %    increased (Default: 4)
% % 8. maximum number of cutbacks allowed for an increment. (Default: 5)
% Exp.ContactPenalty = [0, 0, 1];
% % 1. User-defined linear penalty stiffness. If this field is left blank or
% %    is zero, the final linear penalty stiffness has the default value or
% %    is multiplied by the scale factor given in the third field of the data
% %    line.(Default: 0)
% % 2. Clearance at which the contact pressure is zero, c0. (Default: 0)
% % 3. Scale factor for the default linear penalty stiffness or for the linear
% %    penalty stiffness if specified in the first field of the data line.
% %    (Default: 1)
%
% Exp.NodeBias = 1; % <1: skew to left | >1: skew to right | scalar: single
skew | 2-values: skew from mid-plane
% Exp.nNodes = 100000;
% Exp.ElementType = 4;
% ========================================================================

Exp = Dist_Args(varargin);
Exp = Convert_Units(Exp, 'To', Exp.ConvertUnits);

if regexpi(Exp.AnalysisType, 'Simulation')
    BCT_MakeINP(Exp);
    pause(1);
    % FEA
    delete('*.lck');
    switch upper(Exp.ContactModel)
        case {'MD', 'LJ'}
            Make_UserSubroutine(Exp);
            [~,~] = system(sprintf('abaqus interactive job=%s cpus=%i user=%s',
Exp.FEName, Get_NCores, [Exp.FEName, '_userSub.for']));
        case {'HERTZ', 'JKR', 'NONE'}
            [~,~] = system(sprintf('abaqus interactive job=%s cpus=%i',
Exp.FEName, Get_NCores));
    end
end
if regexpi(Exp.AnalysisType, 'Analysis')
    % Outputs
    [X,dX,b,q,w0,t,J] = BCT_GetOutputs(Exp);
```

```
    for ii=['b', 'm', 't']
        Outputs = struct;
        Outputs.X = X.(ii);
        Outputs.dX = dX.(ii);
        Outputs = Convert_Units(Outputs, 'From', Exp.ConvertUnits);
        X.(ii) = Outputs.X;
        dX.(ii) = Outputs.dX;
    end
    Outputs = struct;
    Outputs.b = b;
    Outputs.q = q;
    Outputs.w0 = w0;
    Outputs.t = t;
    Outputs.J = J;
    Outputs = Convert_Units(Outputs, 'From', Exp.ConvertUnits);
    b = Outputs.b;
    q = Outputs.q;
    w0 = Outputs.w0;
    t = Outputs.t;
    J = Outputs.J;

    varargout = cell(1, nargout);
    for ii=1:nargout
        switch ii
            case 1
                varargout{ii} = b;
            case 2
                varargout{ii} = q;
            case 3
                varargout{ii} = t;
            case 4
                varargout{ii} = w0;
            case 5
                varargout{ii} = X;
            case 6
                varargout{ii} = dX;
            case 7
                varargout{ii} = J;
            otherwise
                varargout{ii} = [];
        end
    end
else
    varargout = cell(1, nargout);
end

end

%% BCT_MakeINP
function BCT_MakeINP(Exp)
[node, Nh, NMult, MidRadNode, MidAxialNode, ContactLength] = Get_NodeInfo(Exp);

file = fopen([Exp.FEName, '.inp'], 'w');
finishup = onCleanup(@()fclose(file));
fprintf(file,
'**==========================================================================
====================\n');
fields = fieldnames(Exp);
```

```
for ii=1:numel(fields)
    if isnumeric(Exp.(fields{ii}))
        fprintf(file, '**% 25s: %s\n', fields{ii},
num2str(Exp.(fields{ii})(:)', '%-10g'));
    elseif ischar(Exp.(fields{ii}))
        fprintf(file, '**% 25s: %s\n', fields{ii}, Exp.(fields{ii}));
    elseif islogical(Exp.(fields{ii}))
        fprintf(file, '**% 25s: %s\n', fields{ii},
num2str(Exp.(fields{ii})(:)', '%-10g'));
    elseif iscellstr(Exp.(fields{ii}))
        fprintf(file, '**% 25s: %s\n', fields{ii},
cell2mat(cellfun(@(x)sprintf('%-10s', x), Exp.(fields{ii})(:)',
'UniformOutput', false)));
    end
end
fprintf(file,
'**============================================================================
====================\n');
fprintf(file, '** Job name: %s\n', Exp.FEName);
fprintf(file, '** Generated with Matlab %s\n', version);
fprintf(file, '** Generated on: %s\n', date);
fprintf(file, '** %i node elements\n', Exp.ElementType);
fprintf(file, '*Heading\n');
fprintf(file, '*Preprint, echo=NO, history=NO, model=NO, contact=NO\n');
fprintf(file,
'**============================================================================
====================\n');
switch upper(Exp.ContactModel)
    case {'HERTZ', 'MD', 'LJ'}
        fprintf(file, '*Node\n');
        fprintf(file, '% 9i, % 8.4E, % 8.4E\n', 999999999, 0, Exp.delta);
        fprintf(file, '*Surface, Type=Segments, Name=SurfRigid\n');
        fprintf(file, 'START, % 8.4E, % 8.4E\n', Exp.R, Exp.delta);
        fprintf(file, 'LINE, % 8.4E, % 8.4E\n', 0, Exp.delta);
        fprintf(file, '*Rigid Body, Analytical Surface=SurfRigid, REF
NODE=999999999\n');
    case {'JKR', 'NONE'}
end
if ~isnan(Exp.kT)
    fprintf(file, '*Node,  NSet=RefNode\n');
    fprintf(file, '999999998, % 8.4E, % 8.4E\n', (node(2,2)+node(4,2))/2,
(node(2,3)+node(4,3))/2);
end
fprintf(file, '*Node\n');
if node(6,1)>node(4,1) % Coating layer exists
    fprintf(file, '% 9i, % 8.6E, % 8.6E\n', node(1:6,:)');
else
    fprintf(file, '% 9i, % 8.6E, % 8.6E\n', node(1:4,:)');
end
if ~isempty(MidRadNode) % Bi-directional node bias
    fprintf(file, '% 9i, % 8.6E, % 8.6E\n', MidRadNode');
end
if ~isempty(MidAxialNode)
    fprintf(file, '% 9i, % 8.6E, % 8.6E\n', MidAxialNode');
    fprintf(file, '*NSet,  NSet=CenterNode_S\n');
    fprintf(file, '% 9i\n', node(1,1));
    fprintf(file, '*NSet,  NSet=OuterEdgeNode_S\n');
    fprintf(file, '% 9i\n', node(2,1));
```

```
    fprintf(file, '*NSet,  NSet=CenterNode_N\n');
    fprintf(file, '% 9i\n', node(3,1));
    fprintf(file, '*NSet,  NSet=OuterEdgeNode_N\n');
    fprintf(file, '% 9i\n', node(4,1));
    fprintf(file, '*NSet,  NSet=CenterNode_M\n');
    fprintf(file, '% 9i\n', MidAxialNode(1,1));
    fprintf(file, '*NSet,  NSet=OuterEdgeNode_M\n');
    fprintf(file, '% 9i\n', MidAxialNode(2,1));
    fprintf(file, '*NFill, NSet=CenterPlate_S, Bias=%g\n', Exp.NodeBias(3));
    fprintf(file, 'CenterNode_S,     CenterNode_M, % 9i, % 9i\n',
(MidAxialNode(1,1)-node(1,1))/Nh, Nh);
    fprintf(file, '*NFill, NSet=CenterPlate_N, Bias=%g\n', (2-
Exp.NodeBias(3)));
    fprintf(file, 'CenterNode_M,     CenterNode_N, % 9i, % 9i\n', (node(3,1)-
MidAxialNode(1,1))/Nh, Nh);
    fprintf(file, '*NFill, NSet=OuterEdgePlate_S, Bias=%g\n', Exp.NodeBias(3));
    fprintf(file, 'OuterEdgeNode_S,  OuterEdgeNode_M, % 9i, % 9i\n',
(MidAxialNode(2,1)-node(2,1))/Nh, Nh);
    fprintf(file, '*NFill, NSet=OuterEdgePlate_N, Bias=%g\n', (2-
Exp.NodeBias(3)));
    fprintf(file, 'OuterEdgeNode_M,  OuterEdgeNode_N, % 9i, % 9i\n',
(node(4,1)-MidAxialNode(2,1))/Nh, Nh);
    fprintf(file, '*NSet,  NSet=CenterPlate\n');
    fprintf(file, 'CenterPlate_S,    CenterPlate_N\n');
    fprintf(file, '*NSet,  NSet=OuterEdgePlate\n');
    fprintf(file, 'OuterEdgePlate_S, OuterEdgePlate_N\n');
else
    fprintf(file, '*NGen,  NSet=CenterPlate\n');
    fprintf(file, '% 9i, % 9i, % 9i\n', node(1,1), node(3,1), Nh);
    fprintf(file, '*NGen,  NSet=OuterEdgePlate\n');
    fprintf(file, '% 9i, % 9i, % 9i\n', node(2,1), node(4,1), Nh);
end
if ~isempty(MidRadNode) % Bi-directional node bias
    fprintf(file, '*NGen,  NSet=MidPlate\n');
    fprintf(file, '% 9i, % 9i, % 9i\n', round(sum(node(1:2,1))/2),
round(sum(node(3:4,1))/2), Nh);
    fprintf(file, '*NFill, NSet=InnerPlate, Bias=%g\n', Exp.NodeBias(1));
    fprintf(file, 'CenterPlate, MidPlate, % 9i, % 9i\n', MidRadNode(1,1)-
node(1,1), 1);
    fprintf(file, '*NFill, NSet=OuterPlate, Bias=%g\n', Exp.NodeBias(2));
    fprintf(file, 'MidPlate,    OuterEdgePlate, % 9i, % 9i\n', node(2,1)-
MidRadNode(1,1), 1);
    fprintf(file, '*NSet,  NSet=Plate\n');
    fprintf(file, 'InnerPlate,  OuterPlate\n');
else % Single-directional node bias
    fprintf(file, '*NFill, NSet=Plate, Bias=%g\n', Exp.NodeBias(1));
    fprintf(file, 'CenterPlate, OuterEdgePlate, % 9i, % 9i\n', node(2,1)-
node(1,1), 1);
end
if node(6,1)>node(4,1) % Adhesive layer exists
    fprintf(file, '*NGen, NSet=CenterCoating\n');
    fprintf(file, '% 9i, % 9i, % 9i\n', node(3,1), node(5,1), Nh);
    fprintf(file, '*NGen, NSet=OuterEdgeCoating\n');
    fprintf(file, '% 9i, % 9i, % 9i\n', node(4,1), node(6,1), Nh);
    if ~isempty(MidRadNode) % Bi-directional node bias
        fprintf(file, '*NGen, NSet=MidCoating\n');
        fprintf(file, '% 9i, % 9i, % 9i\n', round(sum(node(3:4,1))/2),
round(sum(node(5:6,1))/2), Nh);
```

```
        fprintf(file, '*NFill, NSet=InnerCoating, Bias=%g\n', Exp.NodeBias(1));
        fprintf(file, 'CenterCoating,    MidCoating, % 9i, % 9i\n',
MidRadNode(1,1)-node(1,1), 1);
        fprintf(file, '*NFill, NSet=OuterCoating, Bias=%g\n', Exp.NodeBias(2));
        fprintf(file, 'MidCoating,       OuterEdgeCoating, % 9i, % 9i\n',
node(2,1)-MidRadNode(1,1), 1);
        fprintf(file, '*NSet, NSet=Coating\n');
        fprintf(file, 'InnerCoating,     OuterCoating\n');
    else % Single-directional node bias
        fprintf(file, '*NFill, NSet=Coating, Bias=%g\n', Exp.NodeBias(1));
        fprintf(file, 'CenterCoating,    OuterEdgeCoating, % 9i, % 9i\n',
node(2,1)-node(1,1), 1);
    end
    fprintf(file, '*NSet, NSet=Center\n');
    fprintf(file, 'CenterPlate,      CenterCoating\n');
    fprintf(file, '*Nset, NSet=OuterEdge\n');
    fprintf(file, 'OuterEdgePlate,   OuterEdgeCoating\n');
else
    fprintf(file, '*NSet, NSet=Center\n');
    fprintf(file, 'CenterPlate\n');
    fprintf(file, '*Nset, NSet=OuterEdge\n');
    fprintf(file, 'OuterEdgePlate\n');
end
fprintf(file, '*NSet, NSet=Top, Generate\n');
fprintf(file, '% 9i, % 9i, % 9i\n', node(5,1), node(6,1), 1);
fprintf(file, '*NSet, NSet=Bottom, Generate\n');
fprintf(file, '% 9i, % 9i, % 9i\n', node(1,1), node(2,1), 1);
switch upper(Exp.ContactModel) % Crack tip nodes
    case 'JKR'
        fprintf(file, '*NSet, NSet=ContactArea, Generate\n');
        fprintf(file, '% 9i, % 9i, % 9i\n', node(5,1), node(5,1)+ContactLength,
1);
        fprintf(file, '*NSet, NSet=CrackSet, Generate\n');
        fprintf(file, '% 9i, % 9i, % 9i\n', [-2,2]+node(5,1)+ContactLength, 1);
        fprintf(file, '*NSet, NSet=CrackTip\n');
        fprintf(file, '%i\n', node(5,1)+ContactLength);
end
fprintf(file,
'**================================================================================
====================\n');
switch NMult
    case 1 % 4-node element
        if Exp.Nu(1)>0.48 || isnan(Exp.Nu(1)) % Hybrid elements for
incompressible material
            fprintf(file, '*Element, Type=CAX4H\n');
        else
            fprintf(file, '*Element, Type=CAX4\n');
        end
        fprintf(file, '% 9i, % 9i, % 9i, % 9i, % 9i\n', 1, node(1,1),
node(1,1)+1, node(1,1)+Nh+1, node(1,1)+Nh);
        fprintf(file, '*ElGen, ElSet=ElPlate\n');
        fprintf(file, '% 9i, % 9i, % 9i, % 9i, % 9i, % 9i, % 9i\n', 1,
Exp.R_elements, 1, 1, Exp.h_elements(1), Nh, Nh);
        if node(6,1)>node(4,1) % Coating layer exists
            if Exp.Nu(2)>0.48 || isnan(Exp.Nu(2)) % Hybrid elements for
incompressible material
                fprintf(file, '*Element, Type=CAX4H\n');
            else
```

```
                fprintf(file, '*Element, Type=CAX4\n');
            end
            fprintf(file, '% 9i, % 9i, % 9i, % 9i, % 9i\n',
1+Nh*Exp.h_elements(1), node(3,1), node(3,1)+1, node(3,1)+Nh+1, node(3,1)+Nh);
            fprintf(file, '*ElGen, ElSet=ElCoating\n');
            fprintf(file, '% 9i, % 9i, % 9i, % 9i, % 9i, % 9i\n',
1+Nh*Exp.h_elements(1), Exp.R_elements, 1, 1, Exp.h_elements(2), Nh, Nh);
        end
    case 2 % 8-node element
        if Exp.Nu(1)>0.48 || isnan(Exp.Nu(1)) % Hybrid elements for
incompressible material
            fprintf(file, '*Element, Type=CAX8H\n');
        else
            fprintf(file, '*Element, Type=CAX8\n');
        end
        fprintf(file, '% 9i, % 9i, % 9i, % 9i, % 9i, % 9i, % 9i, % 9i, % 9i\n',
1, node(1,1), node(1,1)+2, node(1,1)+Nh*2+2, node(1,1)+Nh*2, node(1,1)+1,
node(1,1)+Nh+2, node(1,1)+Nh*2+1, node(1,1)+Nh);
        fprintf(file, '*ElGen, ElSet=ElPlate\n');
        fprintf(file, '% 9i, % 9i, % 9i, % 9i, % 9i, % 9i, % 9i\n', 1,
Exp.R_elements, 2, 1, Exp.h_elements(1), Nh*2, Nh);
        if node(6,1)>node(4,1) % Coating layer exists
            if Exp.Nu(2)>0.48 || isnan(Exp.Nu(2)) % Hybrid elements for
incompressible material
                fprintf(file, '*Element, Type=CAX8H\n');
            else
                fprintf(file, '*Element, Type=CAX8\n');
            end
            fprintf(file, '% 9i, % 9i, % 9i, % 9i, % 9i, % 9i, % 9i, % 9i, %
9i\n', 1+Nh*Exp.h_elements(1), node(3,1), node(3,1)+2, node(3,1)+Nh*2+2,
node(3,1)+Nh*2, node(3,1)+1, node(3,1)+Nh+2, node(3,1)+Nh*2+1, node(3,1)+Nh);
            fprintf(file, '*ElGen, ElSet=ElCoating\n');
            fprintf(file, '% 9i, % 9i, % 9i, % 9i, % 9i, % 9i, % 9i\n',
1+Nh*Exp.h_elements(1), Exp.R_elements, 2, 1, Exp.h_elements(2), Nh*2, Nh);
        end
    otherwise
end
fprintf(file, '*ElSet, ElSet=ElBottom, Generate\n');
fprintf(file, '% 9i, % 9i, % 9i\n', 1, Exp.R_elements, 1);
fprintf(file, '*ElSet, ElSet=ElTop, Generate\n');
fprintf(file, '% 9i, % 9i, % 9i\n', Nh*(sum(Exp.h_elements)-1)+1,
Nh*(sum(Exp.h_elements)-1)+Exp.R_elements, 1);
fprintf(file,
'**=============================================================================
==================\n');
% Surfaces
fprintf(file, '*Surface, Name=SurfBottom\n');
fprintf(file, 'ElBottom, S1\n');
fprintf(file, '*Surface, NAME=SurfTop\n');
fprintf(file, 'ElTop, S3\n');
fprintf(file,
'**=============================================================================
==================\n');
% Sections and material properties
fprintf(file, '*Solid Section, ElSet=ElPlate, Material=IsotropicMaterial\n');
fprintf(file, '*Material, Name=IsotropicMaterial\n');
if isnan(Exp.Nu(1)) || Exp.Nu(1)==0.5
    fprintf(file, '*Hyperelastic, Neo Hooke, Moduli=Long Term\n');
```

```
    fprintf(file, '% 8.6E, % 8.6E\n', Exp.Es(1)/6, 0);
else
    fprintf(file, '*Elastic\n');
    fprintf(file, '% 8.4E, %0.5f\n', Exp.Es(1), Exp.Nu(1));
end
if node(6,1)>node(4,1) % Coating layer exists
    fprintf(file, '*Solid Section, ElSet=ElCoating,
Material=CoatingMaterial\n');
    fprintf(file, '*Material, Name=CoatingMaterial\n');
    if ~isempty(Exp.Visco) % Viscoelastic coating
        if isnan(Exp.Nu(2)) || Exp.Nu(2)==0.5 % Hyperelastic, D1 = 0, C10 =
Es/6
            fprintf(file, '*Hyperelastic, Neo Hooke, Moduli=Instantaneous\n');
            fprintf(file, '% 8.6E, % 8.6E\n', Exp.Es(2)/6, 0);
        else
            fprintf(file, '*Elastic, Moduli=Instantaneous\n'); % Specify G_0
            fprintf(file, '%10.8E, %0.5f\n', Exp.Es(2), Exp.Nu(2));
        end
        switch lower(Exp.ViscoType)
            case 'prony'
                if size(Exp.Visco,1)==3
                    Exp.Visco = Exp.Visco';
                elseif all(size(Exp.Visco)~=3)
                    error('Incorrect format for Prony series parameters.');
                end
                fprintf(file, '*Viscoelastic, Time=Prony\n');
                fprintf(file, '% 12.10E, % 12.10E, % 12.10E\n', Exp.Visco');
            case 'modulus'
                if size(Exp.Visco,1)==5
                    Exp.Visco = Exp.Visco';
                elseif all(size(Exp.Visco)~=5)
                    error('Incorrect format for Prony series parameters.');
                end
                fprintf(file, '*Viscoelastic, Time=Frequency Data, NMax=%i\n',
min([13,ceil(log10(range(Exp.Visco(:,5))))]));
                fprintf(file, '% 8.6E, % 8.6E, % 8.6E, % 8.6E, % 8.6E\n',
sortrows(Exp.Visco,5)');
        end
    else % Elastic coating
        if isnan(Exp.Nu(2)) || Exp.Nu(2)==0.5 % Hyperelastic, D1 = 0, C10 =
Es/6
            fprintf(file, '*Hyperelastic, Neo Hooke, Moduli=Long Term\n');
            fprintf(file, '% 8.6E, % 8.6E\n', Exp.Es(2)/6, 0);
        else
            fprintf(file, '*Elastic, Moduli=Long Term\n');
            fprintf(file, '%10.8E, %0.5f\n', Exp.Es(2), Exp.Nu(2));
        end
    end
end
% Compliant boundary
if ~isnan(Exp.kT)
    fprintf(file,
'**================================================================================
==================\n');
    fprintf(file, '*Rigid Body, Ref Node=RefNode, Pin NSet=OuterEdge\n');
    fprintf(file, '*Element, Type=Spring1, ElSet=TorsionSpring\n');
    fprintf(file, '%i, %i\n', 999999998, 999999998);
    fprintf(file, '*Spring, ElSet=TorsionSpring\n');
```

```
    fprintf(file, '6\n');
    fprintf(file, '% 8.4E\n', Exp.kT*(2*pi*Exp.R));
end
% Contact interaction
switch upper(Exp.ContactModel)
    case {'JKR', 'NONE'}
    case {'HERTZ', 'MD', 'LJ'}
        fprintf(file,
'**=============================================================================
====================\n');
        fprintf(file, '*Contact Pair, Interaction=Contact, Type=Node To
Surface, Tracking=State\n');
        fprintf(file, 'SurfTop, SurfRigid\n');
        fprintf(file, '*Surface Interaction, Name=Contact\n');
        if ~Exp.Frictionless
            if isinf(Exp.FrictionCoefficient)
                fprintf(file, '*Friction, Rough\n');
            else
                fprintf(file, '*Friction\n');
                fprintf(file, '% 8.6E\n', Exp.FrictionCoefficient);
            end
        end
        fprintf(file, '*Surface Behavior, Penalty=Linear\n'); % | No Separation
| Augmented Lagrange |
        fprintf(file, '% 8.6E, % 8.6E, % 8.6E\n', 0, 0, 1);
%         fprintf(file, '*Surface Behavior, Direct\n');
%         fprintf(file, '*Contact Damping, Definition=Damping Coefficient\n');
%         fprintf(file, '% 8.4E, % 8.4E, % 8.4E\n', 0.1, Exp.delta/10, 0);
    otherwise
end
fprintf(file,
'**=============================================================================
====================\n');
% Boundary conditions
BoundaryConditions(file, Exp);
fprintf(file,
'**=============================================================================
====================\n');
% Initial condition
if Exp.sigma_0>0
    fprintf(file, '*Initial Conditions, Type=Stress\n');
    fprintf(file, 'ElPlate, % 8.4E, % 8.4E, % 8.4E, % 8.4E\n', Exp.sigma_0, 0,
Exp.sigma_0, 0);
    fprintf(file, '*Step, Name=PreStress, NlGeom=Yes, inc=1000\n');
    fprintf(file, '*Static\n');
    fprintf(file, '1, 1, 1E-5, 1\n');
    fprintf(file, '*End Step\n');
    fprintf(file,
'**=============================================================================
====================\n');
end
for ii=1:numel(Exp.q)
    fprintf(file, '*Step, Name=Step_%04i, NlGeom=Yes, Inc=%i\n', ii, 100000);
    switch lower(Exp.StepType{ii})
        case 'static'
            fprintf(file, '*Static\n');
            fprintf(file, '% 8.4E, % 8.4E, % 8.4E, % 8.4E\n',
[Exp.StepSize(ii), 1, Exp.StepSize(ii)*1e-8, Exp.StepSize(ii)]*Exp.t(ii));
```

```
        case 'direct'
            fprintf(file, '*Static, Direct=No Stop\n');
            fprintf(file, '% 8.4E, % 8.4E, % 8.4E, % 8.4E\n',
[Exp.StepSize(ii), 1, Exp.StepSize(ii)*1e-8, Exp.StepSize(ii)]*Exp.t(ii));
        case 'stabilize'
            if ii>1 && Exp.StepContinue(ii)
                fprintf(file, '*Static, Stabilize=%g, ALLSDTol=%g,
Continue=Yes\n', Exp.StablizeEnergy, Exp.ALLSDTOL);
            else
                fprintf(file, '*Static, Stabilize=%g, ALLSDTol=%g,
Continue=No\n', Exp.StablizeEnergy, Exp.ALLSDTOL);
            end
            fprintf(file, '% 8.4E, % 8.4E, % 8.4E, % 8.4E\n',
[Exp.StepSize(ii), 1, Exp.StepSize(ii)*1e-8, Exp.StepSize(ii)]*Exp.t(ii));
        case 'visco'
            if ii>1 && Exp.StepContinue(ii)
                fprintf(file, '*Visco, Stabilize=%g, CETOL=1e-1, AllSDTol=%g,
Continue=Yes\n', Exp.StablizeEnergy, Exp.ALLSDTOL);
            else
                fprintf(file, '*Visco, Stabilize=%g, CETOL=1e-1, AllSDTol=%g,
Continue=No\n', Exp.StablizeEnergy, Exp.ALLSDTOL);
            end
            fprintf(file, '% 8.4E, % 8.4E, % 8.4E, % 8.4E\n',
[Exp.StepSize(ii), 1, Exp.StepSize(ii)*1e-5, Exp.StepSize(ii)]*Exp.t(ii));
        case 'riks'
            if ii==numel(Exp.q)
                fprintf(file, '*Static, Riks\n');
                if numel(Exp.q)==1
                    fprintf(file, '% 8.4E, % 8.4E, % 8.4E, % 8.4E, % 8.4E, %
8i, % 8i, % 8.4E\n', ...
                        Exp.StepSize(ii), 1, Exp.StepSize(ii)*1e-8,
Exp.StepSize(ii), ... | Ini. inc. | Total L | Min L | Max L |
                        1, node(end-1,1), 2, Exp.delta*1.01); % | Load factor |
Node num | DoF | Max Disp |
                elseif Exp.q(end)>=Exp.q(end-1)
                    fprintf(file, '% 8.4E, % 8.4E, % 8.4E, % 8.4E, % 8.4E, %
8i, % 8i, % 8.4E\n', ...
                        Exp.StepSize(ii), 1, Exp.StepSize(ii)*1e-8,
Exp.StepSize(ii), ... | Ini. inc. | Total L | Min L | Max L |
                        1, node(end-1,1), 2, Exp.delta*1.01); % | Load factor |
Node num | DoF | Max Disp |
                else
                    fprintf(file, '% 8.4E, % 8.4E, % 8.4E, % 8.4E, % 8.4E, %
8i, % 8i, % 8.4E\n', ...
                        Exp.StepSize(ii), 1, Exp.StepSize(ii)*1e-8,
Exp.StepSize(ii), ... | Ini. inc. | Total L | Min L | Max L |
                        1, node(end-1,1), 2, -Exp.delta*0.01); % | Load factor
| Node num | DoF | Max Disp |
                end
            else
                fprintf(file, '*Static\n');
                fprintf(file, '% 8.4E, % 8.4E, % 8.4E, % 8.4E\n',
[Exp.StepSize(ii), 1, Exp.StepSize(ii)*1e-8, Exp.StepSize(ii)]*Exp.t(ii));
            end
    end
    fprintf(file, '*Controls, Parameters=Time Incrementation\n');
    fprintf(file, '% 8i, , , , % 8i, % 8i, , % 8i\n', Exp.TimeControls);
    fprintf(file, ' , , , , 20, ,24,\n');
```

```
    fprintf(file, '*Controls, Parameters=Field, Field=Displacement\n');
    fprintf(file, '% 8.4E, % 8.4E,\n , , % 8.4E\n', Exp.DispControls);
%     fprintf(file, '*Contact Controls, Master=SurfRigid, Slave=SurfTop,
Stabilize\n');
%     fprintf(file, ' , , \n');
%     fprintf(file, '% 8.4E, % 8.4E, % 8.4E\n',
    fprintf(file, '*Dsload\n'); % Applied pressure
    fprintf(file, 'SurfBottom, P, % 8.4E\n', Exp.q(ii));
    switch upper(Exp.ContactModel) % Adhesion stress
        case {'MD', 'LJ'}
            if Exp.ActiveAdhesion(ii)
                fprintf(file, '*Dsload, Follower=No, Constant Resultant=No\n');
                fprintf(file, 'SurfTop, TRVECNU, % 8.4E, 0, 1\n',
Exp.G/Exp.delta_adh);
            end
        case 'JKR'
            fprintf(file, '*Boundary\n');
            fprintf(file, 'ContactArea, 2, 2, % 8.4E\n', Exp.delta);
        otherwise
    end
    StepOutputs(file, Exp);
    fprintf(file, '*Monitor, DoF=2, Node=%i\n', node(end-1,1));
%     if Exp.AdaptiveMesh
%         fprintf(file, '*Adaptive Mesh, ElSet=ElPlate\n');
%     end
    fprintf(file, '*End Step\n');
    fprintf(file,
'**=============================================================================
====================\n');
end
    function StepOutputs(file, Exp)
        % ALLCD: Energy dissipated by creep, swelling, viscoelasticity, and
energy associated with viscous regularization for cohesive elements.
        % ALLSD: Energy dissipated by automatic stabilization. This includes
both volumetric static stabilization
        %           and automatic approach of contact pairs (the latter part
included only for the whole model).
        % ALLIE: Total strain energy. (ALLIE = ALLSE + ALLPD + ALLCD + ALLAE +
ALLQB + ALLEE + ALLDMD.)
        fprintf(file, '*Output, History\n');
        fprintf(file, '*Energy Output\n');
        fprintf(file, 'ALLCD, ALLIE, ALLSD\n');
        switch upper(Exp.ContactModel)
            case {'JKR', 'NONE'}
            otherwise
                % case {'HERTZ', 'MD', 'LJ'}
                fprintf(file, '*Contact Output\n');
                fprintf(file, 'CAREA\n'); % CSTRESS
        end
        fprintf(file, '*Output, Field, Frequency=%i\n', Exp.WriteFrequency);
        fprintf(file, '*Node output\n');
        fprintf(file, 'U, COORD, RF, CF\n');
        fprintf(file, '*Element Output\n');
        fprintf(file, 'S\n');
        switch upper(Exp.ContactModel)
            case 'JKR'
                fprintf(file, '*Contour Integral, Crack Name=Crack,
Contours=10, Crack Tip Nodes, Type=J, Frequency=99999\n');
```

```
                fprintf(file, 'CrackTip, CrackTip, -1, 0\n');
            case 'NONE'
            otherwise
                % case {'HERTZ', 'MD', 'LJ'}
                % CSTRESS   : Contact pressure (CPRESS) and frictional shear
stresses (CSHEAR).
                % CDISP     : Contact opening (COPEN) and relative tangential
motions (CSLIP).
                % CNAREA    : Contact nodal area.
                % CSTATUS   : Contact status.
                fprintf(file, '*Contact Output\n');
                fprintf(file, 'CSTRESS, CSTATUS\n');
        end
    end
    function BoundaryConditions(file, Exp)
        fprintf(file, '*Boundary, OP=New\n');
        fprintf(file, 'Center, 1\n'); % Radial symmetry at center
        if ~isnan(Exp.kT) % Compliant edge
            fprintf(file, 'RefNode, 1\n');
            fprintf(file, 'RefNode, 2\n');
        else % Clamped edge
            fprintf(file, 'OuterEdge, 1\n');
            fprintf(file, 'OuterEdge, 2\n');
        end
        switch upper(Exp.ContactModel)
            case {'JKR', 'NONE'}
            otherwise % Analytical rigid reference point
                % case {'HERTZ', 'MD', 'LJ'}
                fprintf(file, '999999999, Encastre\n');
        end
    end
end

%% Get_NodeInfo
function [node, Nh, NMult, MidRadNode, MidAxialNode, ContactLength] =
Get_NodeInfo(Exp)
Nh = 1000000;
NMult = Exp.ElementType/4;
% [n, r, z]
node(1,:) = [1,                                                    0,      0];
node(2,:) = [NMult*Exp.R_elements+1,                               Exp.R,  0];
node(3,:) = [Nh*NMult*Exp.h_elements(1)+1,                         0,
Exp.h(1)];
node(4,:) = [Nh*NMult*Exp.h_elements(1)+NMult*Exp.R_elements+1,    Exp.R,
Exp.h(1)];
node(5,:) = [Nh*NMult*sum(Exp.h_elements)+1,                       0,
sum(Exp.h)];
node(6,:) = [Nh*NMult*sum(Exp.h_elements)+NMult*Exp.R_elements+1,  Exp.R,
sum(Exp.h)];

node(:,3) = node(:,3) - sum(Exp.h); % Shift model to align top surface with R-
axis (Z=0)

MidRadNode = [];
MidAxialNode = [];
ContactLength = [];
switch Exp.ContactModel
    case 'JKR'
```

```
        ContactLength = round(Exp.b/Exp.R*Exp.R_elements(1)*NMult);
    otherwise
        % Bi-directional bias along radial direction
        if numel(Exp.NodeBias)>=2
            if ~isnan(Exp.NodeBias(2))
                if node(6,1)>node(4,1) % Coating layer exists
                    MidRadNode = (node(1:2:5,:)+node(2:2:6,:))/2;
                else
                    MidRadNode = (node(1:2:3,:)+node(2:2:4,:))/2;
                end
                MidRadNode(:,1) = round(MidRadNode(:,1));
            end
        else
            MidRadNode = [];
        end
        % Bi-directional bias within film layer
        if numel(Exp.NodeBias)>=3
            MidAxialNode(1,:) = [Nh*NMult*round(Exp.h_elements(1)/2)+1,
0,      Exp.h(1)/2];
            MidAxialNode(2,:) =
[Nh*NMult*round(Exp.h_elements(1)/2)+NMult*Exp.R_elements+1,    Exp.R,
Exp.h(1)/2];
            MidAxialNode(:,3) = MidAxialNode(:,3) - sum(Exp.h); % Shift model
to align top surface with R-axis (Z=0)
        else
            MidAxialNode = [];
        end
end
end
%% Get_NCores
function NCores = Get_NCores
[~,pcname] = system('hostname');
switch lower(strtrim(pcname))
    case 'nathanwork-pc'
        NCores = 2;
    case {'ktgroup-server2', 'ktgroup-server'}
        NCores = 2;
    case {'nathanhome-pc', 'monstra'}
        NCores = 8;
    case 'nsadesktop'
        NCores = 4;
    case 'drip'
        NCores = 4;
    otherwise
        NCores = 2;
end
end

%% Make_UserSubroutine
function Make_UserSubroutine(Exp)
% MD-type
% G = s_adh*d_adh
% ^      _____
% |     |     |
% |     |     |
% ---------------->
%
% LJ-type
```

```
% G = 3/8*s_adh*d_adh
% sigma = s_adh*((d_adh/(d+d_adh))^3 - (d_adh/(d+d_adh))^9)
% ^      __
% |     /  \
% |    |    \____
% ---------------->
% Max sigma: 16*G/(9*sqrt(3)*d_adh)
%   @ delta: (3^(1/6)-1)*d_adh

file = fopen([Exp.FEName, '_userSub.for'], 'w');

fprintf(file, 'c\n');
fprintf(file, 'c     user subroutine for traction load\n');
fprintf(file, 'c     Type: %s\n', Exp.ContactModel);
fprintf(file, 'c     SERR: %f\n', Exp.G);
fprintf(file, 'c     Range: %f\n', Exp.delta_adh);
fprintf(file, 'c\n');
fprintf(file, '      subroutine
utracload(alpha,t_user,kstep,kinc,times,noel,npt,\n');
fprintf(file, '     $     coords,dircos,jltyp,surface_name)\n');
fprintf(file, 'c\n');
fprintf(file, '      include ''aba_param.inc''\n');
fprintf(file, 'c\n');
fprintf(file, '      dimension t_user(3),times(*),coords(*), dircos(3,*)\n');
fprintf(file, '      character*80 surface_name\n');
fprintf(file, '      real VDIST, HDIST, VGAP\n');
fprintf(file, 'c\n');
fprintf(file, '      VGAP = %0.9f-COORDS(2)\n', Exp.delta);
switch upper(Exp.ContactModel)
    case 'MD'
        fprintf(file, '      if (VGAP .le. %0.9f) then\n', Exp.delta_adh); %
.and. VGAP .gt. 0
        fprintf(file, '         alpha = %0.9f\n', Exp.G/Exp.delta_adh);
        fprintf(file, '      else\n');
        fprintf(file, '         alpha = 0.0\n');
        fprintf(file, '      end if\n');
    case 'LJ'
        fprintf(file, '      ZREF = %0.9f/(VGAP+%0.9f)\n', Exp.delta_adh,
Exp.delta_adh);
        fprintf(file, '      alpha = (8*%0.9f)/(3*%0.9f)*(ZREF**3 -
ZREF**9)\n', Exp.G, Exp.delta_adh);
end
fprintf(file, 'c\n');
for ii=2:numel(Exp.q)
    if Exp.sigma_0>0
        kstep = ii+1;
    else
        kstep = ii;
    end
    % Find step that just activated adhesion (excludes 1st step)
    if Exp.ActiveAdhesion(ii) && ~Exp.ActiveAdhesion(ii-1)
        fprintf(file, '      if (kstep .eq. %i) then\n', kstep);
        fprintf(file, '         alpha = alpha*times(1)\n');
        fprintf(file, '      end if\n');
    end
    % Find step that just de-activated adhesion (excludes 1st step)
    if ~Exp.ActiveAdhesion(ii) && Exp.ActiveAdhesion(ii-1)
        switch lower(Exp.StepType{ii})
```

```
            case {'riks', 'manualstabilize'}
                fprintf(file, '      if (kstep .eq. %i) then\n', kstep);
            otherwise
                fprintf(file, '      if (kstep .eq. 1) then\n');
        end
        fprintf(file, '         alpha = alpha*(%g-times(1))\n', Exp.t(ii));
        fprintf(file, '      end if\n');
    end
end
fprintf(file, 'c\n');
fprintf(file, '      t_user(1)=0.0\n');
fprintf(file, '      t_user(2)=1.0\n');
fprintf(file, '      t_user(3)=0.0\n');
fprintf(file, '\n');
fprintf(file, '      return\n');
fprintf(file, '      end\n');
fclose(file);
end
%% BCT_GetOutputs
function [X,dX,b,q,w0,t,J] = BCT_GetOutputs(Exp)
ContactThreshold = 0.9999;

[node, Nh, NMult] = Get_NodeInfo(Exp);
BottomLayer = node(1,1):node(2,1);
MidLayer = BottomLayer + Nh*NMult*round(Exp.h_elements(1)/2);
TopLayer = node(end-1,1):node(end,1);
NodeList = [BottomLayer, MidLayer, TopLayer];
nNodes = node(2,1)-node(1,1)+1;

switch upper(Exp.ContactModel)
    case {'HERTZ', 'MD', 'NONE', 'LJ'}
        if strcmpi(Exp.StepType, 'Riks')
            [U, q] = Read_ODB_data_BCT(Exp.FEName, NodeList, {'Loading',
'RiksLoading'}, {'COORD', 'T'});
            i = find(q==0);
            q(i(2):end) = q(i(2):end)+q(i(2)-1);
            q = q/2;
        else
            [U, t] = Read_ODB_data_BCT(Exp.FEName, NodeList,
cellfun(@(x)sprintf('Step_%04i', x), num2cell(1:numel(Exp.q)), 'UniformOutput',
false), {'COORD', 'T'});
            n = find(t==0);
            if numel(n)>1
                t_step = t(n(2:end)-1);
                for ii=2:numel(n)
                    t(n(ii):end) = t(n(ii):end) + t_step(ii-1);
                end
            end
            if strcmpi(Exp.OutputData, 'Step')
                t = t([1;n(2:end)-1;numel(U)]);
                U = U([1;n(2:end)-1;numel(U)]);
            end
        end
        J = [];
    case 'JKR'
        Exp.OutputData = 'final'; % Only output the last data
        [U, t, J] = Read_ODB_data_BCT(Exp.FEName, NodeList,
sprintf('Step_%04i', numel(Exp.q)), {'COORD', 'T', 'J'});
```

```
end

switch lower(Exp.OutputData)
    case {'all', 'step'}
        % Position data
        U = reshape(cell2mat(U'), size(U{1},1), size(U{1},2), []);
        X.b = squeeze(U(0*nNodes+1:1*nNodes, :, 1));
        X.m = squeeze(U(1*nNodes+1:2*nNodes, :, 1));
        X.t = squeeze(U(2*nNodes+1:3*nNodes, :, 1));
        % Displacement data
        dX.b = U(0*nNodes+1:1*nNodes, :, :) - repmat(X.b,1,1,size(U,3));
        dX.m = U(1*nNodes+1:2*nNodes, :, :) - repmat(X.m,1,1,size(U,3));
        dX.t = U(2*nNodes+1:3*nNodes, :, :) - repmat(X.t,1,1,size(U,3));
        % Single quantities
        w0 = reshape((dX.b(1,2,:) + dX.t(1,2,:))/2, size(t));
        q = interp1(cumsum([0; Exp.t(:)]), [0; Exp.q(:)], t);
        b = zeros(size(t));
        for i=size(U,3):-1:1
            b(i) = find(dX.t(:,2,i)<Exp.delta*ContactThreshold,1,'first');
        end
        b = reshape(X.b(b,1), size(t));
    case 'final'
        % Position data
        X.b = U{1}(0*nNodes+1:1*nNodes, :);
        X.m = U{1}(1*nNodes+1:2*nNodes, :);
        X.t = U{1}(2*nNodes+1:3*nNodes, :);
        % Displacement data
        U = U{end};
        dX.b = U(0*nNodes+1:1*nNodes, :) - X.b;
        dX.m = U(1*nNodes+1:2*nNodes, :) - X.m;
        dX.t = U(2*nNodes+1:3*nNodes, :) - X.t;
        % Single quantities
        b = X.b(find(dX.t(:,2)<Exp.delta*ContactThreshold,1,'first'),1);
        w0 = (dX.b(1,2) + dX.t(1,2))/2;
        q = Exp.q;
        J = J(end);
    otherwise
end

end
%% Convert_Units
function Exp = Convert_Units(Exp, Direction, ConversionType)
switch lower(Direction)
    case 'to'
        Direction = 1;
    case 'from'
        Direction = -1;
end
FNames = fieldnames(Exp);

MassConvert = 1;
LengthConvert = 1;
TimeConvert = 1;
ConversionType = strsplit(ConversionType, '|');
for ii=1:numel(ConversionType)
    switch lower(ConversionType{ii})
        case 'tonne' % 1 tonne = 1e3 kg
            MassConvert = 1e-3;
```

```
        case 'kg'
            MassConvert = 1e0;
        case 'g'
            MassConvert = 1e3;
        case 'mg'
            MassConvert = 1e6;
        case 'ug'
            MassConvert = 1e9;
        case 'ng'
            MassConvert = 1e12;
    end
    switch lower(ConversionType{ii})
        case 'km'
            LengthConvert = 1e-3;
        case 'm'
            LengthConvert = 1e0;
        case 'mm'
            LengthConvert = 1e3;
        case 'um'
            LengthConvert = 1e6;
        case 'nm'
            LengthConvert = 1e9;
        case 'pm'
            LengthConvert = 1e12;
    end
    switch lower(ConversionType{ii})
        case 's'
            TimeConvert = 1;
        case 'ms'
            TimeConvert = 1e3;
        case 'us'
            TimeConvert = 1e6;
    end
end
ForceConvert = MassConvert*LengthConvert/TimeConvert^2;
StressConvert = MassConvert/LengthConvert/TimeConvert^2;
SERRConvert = MassConvert/TimeConvert^2;

for i=1:length(FNames)
    switch FNames{i}
        case {'Es', 'q', 'sigma', 'sigma_0', 'sigma_adh'} % Stress
            Exp.(FNames{i}) = Exp.(FNames{i})*StressConvert^Direction;
        case {'R', 'h', 'delta', 'delta_adh', 'dmax', 'X', 'dX', 'b', 'w0'} %
Length
            Exp.(FNames{i}) = Exp.(FNames{i})*LengthConvert^Direction;
        case {'P'} % Force
            Exp.(FNames{i}) = Exp.(FNames{i})*ForceConvert^Direction;
        case {'G', 'G0', 'J'} % SERR
            Exp.(FNames{i}) = Exp.(FNames{i})*SERRConvert^Direction;
        case {'kT'} % Spring
            Exp.(FNames{i}) = Exp.(FNames{i})*ForceConvert^Direction;
        case {'t'} % Time
            Exp.(FNames{i}) = Exp.(FNames{i})*TimeConvert^Direction;
    end
end
end
%% Read_ODB_data_BCT
function varargout = Read_ODB_data_BCT(FileName, NodeList, StepName, DataList)
```

```
% COORD - [NodeList, 2] - COOR1, COOR2
% U          - [NodeList, 2] - U1, U2
% RF         - [NodeList, 2] - RF1, RF2
% CF         - [NodeList, 2] - CF1, CF2
% T          - [n, 1]
% P          - [n, 1]
% CAREA      - [n, 1]
% J          - [n, 1]
% LPF        - [n, 1] NOT IMPLEMENTED YET
% n is the total number of increments of the step
OutputFile = [FileName, '_Python'];
if ischar(StepName) % Check for cell type
    StepName = {StepName};
end
if ischar(DataList) % Check for cell type
    DataList = {DataList};
end
% Group DataList into different categories
DataClass = zeros(1, numel(DataList));
for i=1:numel(DataList)
    switch upper(DataList{i})
        case {'U', 'COORD', 'RF', 'CF', 'S', 'T', 'P'}
            DataClass(i) = 1;
        case {'LPF', 'CAREA', 'J'}
            DataClass(i) = 2;
    end
end
if any(DataClass==1)
    X1 = ReadFieldOutputData(FileName, NodeList, StepName, OutputFile,
DataList(DataClass==1));
end
if any(DataClass==2)
    X2 = ReadHistoryOutputData(FileName, StepName, OutputFile,
DataList(DataClass==2));
end
X1 = X1(1:size(X1,1)-mod(size(X1,1),numel(NodeList)), :);
varargout = cell(1, length(nargout));
for i=1:length(DataList)
    switch upper(DataList{i})
        case {'U', 'COORD', 'RF', 'CF'} % | [U1, U2] | [COOR1, COOR2] | [RF1,
RF2] | [CF1, CF2] |
            varargout{i} = mat2cell(X1(:,1:2),
ones(1,size(X1,1)/length(NodeList))*length(NodeList), 2);
            X1(:,1:2) = [];
        case {'T', 'P'}
            varargout{i} = X1(1:length(NodeList):end, 1);
            X1(:,1) = [];
        case 'S' % [S11, S12, S22, S33]
            varargout{i} = mat2cell(X1(:,1:4),
ones(1,size(X1,1)/length(NodeList))*length(NodeList), 4);
            X1(:,1:4) = [];
        case {'LPF', 'CAREA', 'J'}
            varargout{i} = X2(:,2);
            X2(:,2) = [];
    end
end
try
    warning('off', 'MATLAB:DELETE:Permission');
```

```
    delete('*.rpy*');
    warning('on', 'MATLAB:DELETE:Permission');
catch
end
end
% ReadFieldOutputData
function X = ReadFieldOutputData(FileName, NodeList, StepName, OutputFile,
DataList)
OutputFile = [OutputFile, '_Field'];
file = fopen([OutputFile, '.py'], 'w');
fprintf(file, 'import odbAccess\n');
fprintf(file, '\n');
fprintf(file, 'names = ''%s''\n', FileName);
fprintf(file, 'nodeNumber = [');
if length(NodeList)>1
    fprintf(file, '%i,', NodeList(1:end-1));
end
fprintf(file, '%i]\n\n', NodeList(end));
fprintf(file, '\n');
fprintf(file, 'NameOfFile = ''%s''+''.txt''\n', OutputFile);
fprintf(file, 'FileResultsX = open(NameOfFile,''w'')\n');
fprintf(file, '\n');
fprintf(file, 'Name = names+''.odb''\n');
fprintf(file, 'myOdb = odbAccess.openOdb(path=Name)\n');
fprintf(file, '\n');
for j=1:length(StepName)
    fprintf(file, 'nameOfStep = ''%s''\n', StepName{j});
    fprintf(file, 'currStep = myOdb.steps[nameOfStep]\n');
    fprintf(file, 'lastFrame = currStep.frames[len(currStep.frames)-1]\n');
    if j==1
        fprintf(file, 'Displacement = lastFrame.fieldOutputs[''U''] \n');
        fprintf(file, 'nLabel = [0 for i in
range(len(Displacement.values))]\n');
        fprintf(file, 'nIndex = [0 for i in range(len(nodeNumber))]\n');
        fprintf(file, 'for z in range(len(Displacement.values)):\n');
        fprintf(file, '    nLabel[z] = Displacement.values[z].nodeLabel\n');
        fprintf(file, 'for z in range(len(nodeNumber)):\n');
        fprintf(file, '    nIndex[z] = nLabel.index(nodeNumber[z])\n');
    end
    fprintf(file, '\n');
    fprintf(file, 'for y in range(0, len(currStep.frames)):\n');
    for i=1:length(DataList)
        switch upper(DataList{i})
            case 'U'
                fprintf(file, '    Displacement =
currStep.frames[y].fieldOutputs[''U'']\n');
            case 'COORD'
                fprintf(file, '    Coordinates =
currStep.frames[y].fieldOutputs[''COORD'']\n');
            case 'RF'
                fprintf(file, '    Force =
currStep.frames[y].fieldOutputs[''RF'']\n');
            case 'CF'
                fprintf(file, '    ConcForce =
currStep.frames[y].fieldOutputs[''CF'']\n');
            case 'S'
                fprintf(file, '    Stress =
currStep.frames[y].fieldOutputs[''S'']\n');
```

```
            case 'T'
                fprintf(file, '   Time = currStep.frames[y].frameValue\n');
            case 'P'
                fprintf(file, '   Pressure =
currStep.frames[y].fieldOutputs[''P''].values[0].data\n');
        end
    end
    fprintf(file, '   for z in [x for x in nIndex]:\n');
    fprintf(file, '      FileResultsX.write(''');
    for i=1:length(DataList)
        switch upper(DataList{i})
            case {'U', 'COORD', 'RF', 'CF'}
                fprintf(file, '%%15.13E\\t %%15.13E\\t ');
            case 'S'
                fprintf(file, '%%15.13E\\t %%15.13E\\t %%15.13E\\t
%%15.13E\\t');
            case {'T', 'P'}
                fprintf(file, '%%15.13E\\t');
        end
    end
    fprintf(file, '\\n'' %% (');
    for i=1:length(DataList)
        switch upper(DataList{i})
            case 'U'
                fprintf(file, 'Displacement.values[z].data[0],
Displacement.values[z].data[1]');
            case 'COORD'
                fprintf(file, 'Coordinates.values[z].data[0],
Coordinates.values[z].data[1]');
            case 'RF'
                fprintf(file, 'Force.values[z].data[0],
Force.values[z].data[1]');
            case 'CF'
                fprintf(file, 'ConcForce.values[z].data[0],
ConcForce.values[z].data[1]');
            case 'S'
                fprintf(file, 'Stress.values[z].data[0],
Stress.values[z].data[1], Stress.values[z].data[2], Stress.values[z].data[3]');
            case 'T'
                fprintf(file, 'Time');
            case 'P'
                fprintf(file, 'Pressure');
        end
        if i<length(DataList)
            fprintf(file, ',');
        end
    end
    fprintf(file, ')) \n');
    fprintf(file, 'FileResultsX.write(''\\n'')\n');
    fprintf(file, '\n');
end
fprintf(file, '\n');
fprintf(file, 'myOdb.close()\n');
fprintf(file, 'FileResultsX.close()\n');
fclose(file);

[~, ~] = system(sprintf('abaqus cae nogui=%s', OutputFile)); % , '-echo'
X = ReadDataFile(OutputFile, DataList);
```

```
end
% ReadHistoryOutputData
function X = ReadHistoryOutputData(FileName, StepName, OutputFile, DataList)
nContour = 'Contour_05';
CheckString = cell(0);
for jj=1:numel(DataList)
    switch DataList{jj}
        case 'J'
            CheckString{end+1} = ' or '; %#ok<AGROW>
            CheckString{end+1} = ['("J at " in OutputKeys[jj] and "', nContour,
'" in OutputKeys[jj])']; %#ok<AGROW>
        case 'CAREA'
            CheckString{end+1} = ' or '; %#ok<AGROW>
            CheckString{end+1} = '("CAREA" in OutputKeys[jj])'; %#ok<AGROW>
    end
end
CheckString(1) = [];
OutputFile = [OutputFile, '_History'];
file = fopen([OutputFile, '.py'], 'w');

fprintf(file, 'import odbAccess\n');
fprintf(file, '\n');
fprintf(file, 'BaseName = ''%s''\n', FileName);
fprintf(file, '\n');
fprintf(file, 'FileName = ''%s''+''.txt''\n', OutputFile);
fprintf(file, 'OutputFile = open(FileName,''w'')\n');
fprintf(file, '\n');
fprintf(file, 'Name = BaseName+''.odb''\n');
fprintf(file, 'currODB = odbAccess.openOdb(path=Name)\n');
for ii=1:numel(StepName)
fprintf(file, 'currStep = currODB.steps[''%s'']\n', StepName{ii});
fprintf(file, 'RegionKeys = currStep.historyRegions.keys()\n');
fprintf(file, 'for ii in range(0, len(RegionKeys)):\n');
fprintf(file, '    currRegion = currStep.historyRegions[RegionKeys[ii]]\n');
fprintf(file, '    OutputKeys = currRegion.historyOutputs.keys()\n');
fprintf(file, '    \n');
fprintf(file, '    for jj in range(0, len(OutputKeys)):\n');
fprintf(file, '        currHistory =
currRegion.historyOutputs[OutputKeys[jj]]\n');
fprintf(file, '        currData = currHistory.data\n');
fprintf(file, '        print len(currData)\n');
fprintf(file, '        print currData\n');
fprintf(file, '        for kk in range(0, len(currData)):\n');
fprintf(file, '            if %s:\n', [CheckString{:}]);
fprintf(file, '                OutputFile.write("%%15.13E\t" %%
currHistory.data[kk][0])\n');
for jj=1:2:numel(CheckString)
    fprintf(file, '            if %s:\n', CheckString{jj});
    fprintf(file, '                OutputFile.write("%%15.13E\t" %%
currHistory.data[kk][1])\n');
end
fprintf(file, '            if %s:\n', [CheckString{:}]);
fprintf(file, '                OutputFile.write("\\n")\n');
fprintf(file, '\n');
end
fprintf(file, 'currODB.close()\n');
fprintf(file, 'OutputFile.close()\n');
```

```
fclose(file);
[~, ~] = system(sprintf('abaqus cae nogui=%s', OutputFile)); % , '-echo'
X = ReadDataFile(OutputFile, ['T', DataList]);
end
% ReadDataFile
function X = ReadDataFile(OutputFile, DataList)
% Returns columns of [U1, U2, U3], [COOR1, COOR2, COOR3], [RF1, RF2, RF3],
[CF1, CF2, CF3], [S11,
% S12, S22, S33], [T], [LPF], [CAREA], [P]
formatSpec = '';
for i=1:length(DataList)
    switch upper(DataList{i})
        case 'S'
            formatSpec = [formatSpec, '%f%f%f%f']; %#ok<AGROW>
        case {'T', 'LPF', 'CAREA', 'P', 'J'}
            formatSpec = [formatSpec, '%f']; %#ok<AGROW>
        otherwise
            formatSpec = [formatSpec, '%f%f']; %#ok<AGROW>
    end
end
formatSpec = [formatSpec, '%[^\n\r]'];
file = fopen([OutputFile, '.txt'], 'r');
finishup = onCleanup(@()fclose(file));
dataArray = textscan(file, formatSpec, 'Delimiter', '\t', 'ReturnOnError',
true);
minLength = min(cellfun(@numel, dataArray));
for ii=1:numel(dataArray)
    dataArray{ii} = dataArray{ii}(1:minLength);
end
X = [dataArray{1:end-1}];
end
%% Dist_Args
function Exp = Dist_Args(Vars)
Exp.Es = [4e9, 1e6]; % Young's modulus
Exp.Nu = [0.3, 0.5]; % Poisson's ratio
Exp.h = [50e-6, 10e-6]; % Thickness
Exp.R = 10e-3; % Radius
Exp.delta = 0.4e-3; % Gap
Exp.kT = nan; % Compliant boundary
Exp.sigma_0 = 0; % Prestress

Exp.ViscoType = 'Prony'; % | Prony | Modulus |
Exp.Visco = []; % Viscoelastic parameters for film | Modulus: [Re(g*), Im(g*),
Re(k*), Im(k*), freq] | Prony: [g, k, tau]

Exp.ContactModel = 'Hertz'; % | JKR | MD | LJ | Hertz | None |
Exp.Frictionless = true;
Exp.FrictionCoefficient = inf; % (Frictionless) 0 < FrictionCoefficient < inf
(No slip)
Exp.G = 0.1;
Exp.delta_adh = 1e-6;

Exp.q = 8000; % Applied pressure
Exp.t = 1; % Time for each pressure step
Exp.ActiveAdhesion = 1;
Exp.StepSize = 0.05; % 1e-5 < t < 1
Exp.StepContinue = false;
```

```
Exp.StepType = 'Static'; % | Static | Riks | Stabilize | Visco | Direct
Exp.FEName = 'BCT_MD_Test';
Exp.OutputData = 'All'; % | All | Final | Step
Exp.AnalysisType = 'SimulationAnalysis'; % | Simulation | Analysis |
SimulationAnalysis |
Exp.ConvertUnits = 'kg|m|s'; % | mg|um|s | g|mm|s | kg|m|s
Exp.WriteFrequency = 1; % Integer, >= 1

% Exp.AdaptiveMesh = false;
Exp.ALLSDTOL = 0.05; % Adaptive automatic stabilization parameter (default:
0.05)
Exp.StablizeEnergy = 2e-4; % Automatic stabilization value for dissipated
energy fraction (default: 2e-4)
Exp.DispControls = [5e-3, 1e-2, 1e-8];
% 1.1. Ratio of the largest residual to the corresponding average flux norm for
convergence
% 1.2. Ratio of the largest solution correction to the largest corresponding
incremental solution value
% 2.3. Criterion for zero displacement increment (and/or zero penetration if
CONVERT SDI=YES)
%      compared to the characteristic element length in the model. (Default:
1e-8)
Exp.TimeControls = [4, 10, 4, 5];
% 1. number of equilibrium iterations (without severe discontinuities) after
%    which the check is made whether the residuals are increasing in two
%    consecutive iterations (Default: 4)
% 5. number of consecutive equilibrium iterations (without severe
discontinuities)
%    above which the size of the next increment will be reduced (Default: 10)
% 6. maximum number of consecutive equilibrium iterations (without severe
discontinuities)
%    allowed in consecutive increments for the time increment to be
%    increased (Default: 4)
% 8. maximum number of cutbacks allowed for an increment. (Default: 5)
Exp.ContactPenalty = [0, 0, 1];
% 1. User-defined linear penalty stiffness. If this field is left blank or
%    is zero, the final linear penalty stiffness has the default value or
%    is multiplied by the scale factor given in the third field of the data
%    line.(Default: 0)
% 2. Clearance at which the contact pressure is zero, c0. (Default: 0)
% 3. Scale factor for the default linear penalty stiffness or for the linear
%    penalty stiffness if specified in the first field of the data line.
%    (Default: 1)

Exp.NodeBias = 1; % <1: skew to left | >1: skew to right | scalar: single skew
| 2-values: skew from mid-plane
Exp.nNodes = 100000;
Exp.ElementType = 4;

% Distribute inputs
for ii=1:numel(Vars)
    if ~isempty(Vars{ii})
        switch ii
            case 1
                fNames = fieldnames(Vars{ii});
                for j=1:numel(fNames)
                    Exp.(fNames{j}) = Vars{ii}.(fNames{j});
                end
```

```
            case 2
                if ~isempty(Vars{ii})
                    Exp.R_elements  = Vars{ii}(1);
                    Exp.h_elements  = Vars{ii}(2);
                    Exp.ElementType = Vars{ii}(3);
                end
            case 3
                Exp.FEName = Vars{ii};
        end
    end
end
if ~(isfield(Exp, 'R_elements') && isfield(Exp, 'h_elements'))
    Exp.nNodes = ceil(nansum(Exp.h)/sqrt(Exp.R*nansum(Exp.h)/Exp.nNodes));
    if Exp.nNodes<5
        Exp.nNodes = 5;
    end
    Exp.h_elements = ceil(Exp.h/nansum(Exp.h)*Exp.nNodes);
    Exp.R_elements = ceil(Exp.R/nansum(Exp.h)*Exp.nNodes);
    Exp.nNodes = sum(Exp.h_elements*Exp.R_elements);
else
    Exp.nNodes = sum(Exp.h_elements*Exp.R_elements);
end

% Fix parameters
if ~isempty(Exp.Visco) % Force viscoelastic simulation
    Exp.StepType = 'Visco';
end
if ischar(Exp.StepType) % Change to cell array
    Exp.StepType = {Exp.StepType};
end
if numel(Exp.t)<numel(Exp.q) % Expand t to same size as q
    Exp.t(end+1:numel(Exp.q)) = Exp.t(end);
end
if numel(Exp.StepSize)<numel(Exp.q) % Expand the StepSize to same size as q
    Exp.StepSize(end+1:numel(Exp.q)) = Exp.StepSize(end);
end
if numel(Exp.StepType)<numel(Exp.q) % Expand the StepType to same size as q
    Exp.StepType(end+1:numel(Exp.q)) = Exp.StepType(end);
end
if numel(Exp.ActiveAdhesion)<numel(Exp.q)
    Exp.ActiveAdhesion(end+1:numel(Exp.q)) = Exp.ActiveAdhesion(end);
end
if numel(Exp.StepContinue)<numel(Exp.q)
    Exp.StepContinue(end+1:numel(Exp.q)) = Exp.StepContinue(end);
end
end
```

BIBLIOGRAPHY

[1] C. Creton, "Pressure-Sensitive Adhesives: An Introductory Course," *MRS Bulletin*, vol. 28, pp. 434–439, 2003.

[2] A. Kowalski and Z. Czech, "The effects of substrate surface properties on tack performance of acrylic Pressure-Sensitive Adhesives (PSAs)," *International Journal of Adhesion and Adhesives*, vol. 60, pp. 9–15, Jul. 2015.

[3] P. Tordjeman, E. Papon, and J.-J. Villenave, "Tack Properties of Pressure-Sensitive Adhesives," *Journal of Polymer Science Part B-Polymer Physics*, vol. 38, pp. 1201–1208, 2000.

[4] M. A. Meitl *et al.*, "Transfer printing by kinetic control of adhesion to an elastomeric stamp," *Nature Materials*, vol. 5, no. 1, pp. 33–38, Jan. 2006.

[5] X. Feng, M. A. Meitl, A. M. Bowen, Y. Huang, R. G. Nuzzo, and J. A. Rogers, "Competing Fracture in Kinetically Controlled Transfer Printing," *Langmuir*, vol. 23, pp. 12555–12560, 2007.

[6] N. Canas, M. Kamperman, B. Volker, E. Kroner, R. M. McMeeking, and E. Arzt, "Effect of Nano- and Micro-roughness on Adhesion of Bioinspired Micropatterned Surfaces," *Acta Biomaterialia*, vol. 8, pp. 282–288, 2012.

[7] M. Kamperman, E. Kroner, A. del Campo, R. M. McMeeking, and E. Arzt, "Functional Adhesive Surfaces with 'Gecko' Effect: The Concept of Contact Splitting," *Advanced Engineering Materials*, vol. 12, no. 5, pp. 335–348, May 2010.

[8] K. Jin, Y. Tian, J. S. Erickson, J. Puthoff, K. Autumn, and N. S. Pesika, "Design and Fabrication of Gecko-Inspired Adhesives," *Langmuir*, vol. 28, pp. 5737–5742, 2012.

[9] S. Y. Yang *et al.*, "Elastomer surfaces with directionally dependent adhesion strength and their use in transfer printing with continuous roll-to-roll applications.," *Advanced materials*, vol. 24, no. 16, pp. 2117–22, Apr. 2012.

[10] S. Kim *et al.*, "Microstructured Elastomeric Surfaces with Reversible Ahdesion and Examples of Their Use in Deterministic Assembly by Transfer Printing," *Proceedings of the National Academy of Sciences of the United States of America*, vol. 107, pp. 17095–17100, 2010.

[11] H. K. Minsky and K. T. Turner, "Achieving enhanced and tunable adhesion via composite posts," *Applied Physics Letters*, vol. 106, no. 20, p. 201604, May 2015.

[12] T.-H. Kim *et al.*, "Kinetically controlled, adhesiveless transfer printing using

microstructured stamps," *Applied Physics Letters*, vol. 94, p. 113502, 2009.

[13] H. Chen, X. Feng, Y. Huang, Y. Huang, and J. A. Rogers, "Experiments and viscoelastic analysis of peel test with patterned strips for applications to transfer printing ," *Journal of the Mechanics and Physics of Solids* , vol. 61, no. 0, pp. 1737–1752, 2013.

[14] E. Charrault, C. Gauthier, P. Marie, and R. Schirrer, "Experimental and Theoretical Analysis of a Dynamic JKR Contact," *Langmuir*, vol. 25, pp. 5847–5854, 2009.

[15] M. D. Thouless and Q. D. Yang, "A Parametric Study of the Peel Test," *International Journal of Adhesion and Adhesives*, vol. 28, pp. 176–184, 2008.

[16] D. Sowa, Z. Czech, and Ł. Byczyński, "Peel adhesion of acrylic pressure-sensitive adhesives on selected substrates versus their surface energies," *International Journal of Adhesion and Adhesives*, vol. 49, pp. 38–43, Mar. 2014.

[17] D. S. Grierson, E. E. Flater, and R. W. Carpick, "Accounting for the JKR–DMT transition in adhesion and friction measurements with atomic force microscopy," *Journal of Adhesion Science and Technology*, vol. 19, no. 3–5, pp. 291–311, Jan. 2005.

[18] P. Silberzan, S. Perutz, E. J. Kramer, and M. K. Chaudhury, "Study of the Self-Adhesion Hysteresis of a Siloxane Elastomer Using the JKR Method," *Langmuir*, vol. 10, pp. 2466–2470, 1994.

[19] B. Lorenz *et al.*, "Adhesion: role of bulk viscoelasticity and surface roughness.," *Journal of physics. Condensed matter : an Institute of Physics journal*, vol. 25, no. 22, p. 225004, Jun. 2013.

[20] K. Kendall, "Peel Adhesion of Solid Films-The Surface and Bulk Effects," *The Journal of Adhesion*, vol. 5, no. 3, pp. 179–202, Aug. 1972.

[21] C. Y. Hui and R. Long, "Direct extraction of work of adhesion from contact experiments: Generalization of JKR Theory to flexible structures and large deformation," *Journal of Adhesion*, vol. 88, pp. 70–85, 2012.

[22] Y. Y. Lin, C. Y. Hui, and Y. C. Wang, "Modeling the Failure of an Adhesive Layer in a Peel Test," *Journal of Polymer Science Part B-Polymer Physics*, vol. 40, pp. 2277–2291, 2002.

[23] M. Deruelle, L. Leger, and M. Tirrell, "Adhesion at the Solid-Elastomer Interface: Influence of the Interfacial Chains," *Macromolecules*, vol. 28, pp. 7419–7428, 1995.

[24] K. Kendall, "Thin-Film Peeling - The Elastic Term," *Journal of Physics D: Applied Physics*, vol. 8, pp. 1449–1452, 1975.

[25] R. Villey *et al.*, "Rate-dependent elastic hysteresis during the peeling of pressure sensitive adhesives," *Soft Matter*, vol. 11, no. 17, pp. 3480–3491, 2015.

[26] L. Zhang and J. Wang, "A Generalized Cohesive Zone Model of the Peel Test for Pressure-Sensitive Adhesives," *International Journal of Adhesion and Adhesives*, vol. 29, pp. 217–224, 2009.

[27] M. J. Wald, J. M. Considine, and K. T. Turner, "Determining the Elastic Modulus of Compliant Thin Films Supported on Substrates from Flat Punch Indentation Measurements," *Experimental Mechanics*, vol. 53, no. 6, pp. 931–941, Jan. 2013.

[28] D. Xu and K. M. Liechti, "Analytical and experimental study of a circular membrane in adhesive contact with a rigid substrate," *International Journal of Solids and Structures*, vol. 48, no. 20, pp. 2965–2976, Oct. 2011.

[29] D. Xu and K. M. Liechti, "Bulge Testing Transparent Thin Films with Moire Deflectometry," *Experimental Mechanics*, vol. 50, pp. 217–225, 2010.

[30] D. Xu and K. M. Liechti, "Analytical and experimental study of a circular membrane in Hertzian contact with a rigid substrate," *International Journal of Solids and Structures*, vol. 47, no. 7–8, pp. 969–977, Apr. 2010.

[31] R. H. Plaut, "Linearly Elastic Annular and Circular Membranes Under Radial, Transverse, and Torsional Loading. Part I: Large Unwrinkled Axisymmetric Deformations," *Acta Mechanica*, vol. 202, pp. 79–99, 2009.

[32] R. H. Plaut, S. A. White, and D. A. Dillard, "Effect of work of adhesion on contact of a pressurized blister with a flat surface," *International Journal of Adhesion and Adhesives*, vol. 23, no. 3, pp. 207–214, Jan. 2003.

[33] F. M. Fowkes, "Attractive Forces at Interfaces," *Industrial & Engineering Chemistry*, vol. 56, no. 12, pp. 40–52, Dec. 1964.

[34] F. W. DelRio, M. L. Dunn, L. M. Phinney, C. J. Bourdon, and M. P. de Boer, "Rough Surface Adhesion in the Presence of Capillary Condensation," *Applied Physics Letters*, vol. 90, pp. 1–3, 2007.

[35] A. Biel, K. S. Alfredsson, and T. Carlberger, "Adhesive Tapes; Cohesive Laws for a Soft Layer," *Procedia Materials Science*, vol. 3, pp. 1389–1393, 2014.

[36] J. E. Lennard-Jones, "On the Determination of Molecular Fields. II. From the Equations of State of a Gas," *Proceedings of the Royal Society of London. Series A*, vol. 106, pp. 377–463, 1924.

[37] F. Tokumura, T. Homma, T. Tomiya, Y. Kobayashi, and T. Matsuda, "Properties of pressure-sensitive adhesive tapes with soft adhesives to human skin and their

mechanism," *Skin Research and Technology*, vol. 13, no. 2, pp. 211–216, May 2007.

[38] A. Pizzi and K. L. Mittal, *Handbook of Adhesive Technology, Revised and Expanded*. CRC Press, 2003.

[39] C. Creton and M. Ciccotti, "Fracture and adhesion of soft materials: a review," *Reports on Progress in Physics*, vol. 79, no. 4, p. 46601, Apr. 2016.

[40] F. M. Fowkes, D. W. Dwight, D. A. Cole, and T. C. Huang, "Acid-base properties of glass surfaces," *Journal of Non-Crystalline Solids*, vol. 120, no. 1–3, pp. 47–60, Apr. 1990.

[41] E. McCafferty and J. P. Wightman, "Determination of the acid-base properties of metal oxide films and of polymers by contact angle measurements," *Journal of Adhesion Science and Technology*, vol. 13, no. 12, pp. 1415–1436, Jan. 1999.

[42] L. Li, M. Tirrell, G. A. Korba, and A. V. Pocius, "Surface Energy and Adhesion Studies on Acrylic Pressure Sensitive Adhesives," *The Journal of Adhesion*, vol. 76, no. 4, pp. 307–334, Aug. 2001.

[43] H. Hertz, "On the Contact of Elastic Solids," *Journal für die reine und angewandte Mathematik*, vol. 92, pp. 156–171, 1881.

[44] K. L. Johnson, K. Kendall, and A. D. Roberts, "Surface Energy and the Contact of Elastic Solids," *Proceedings of the Royal Society A*, vol. 324, pp. 301–313, 1971.

[45] B. V Derjaguin, V. M. Muller, and Y. P. Toporov, "Effect of Contact Deformations on the Adhesion of Particles," *Journal of Colloid and Interface Science*, vol. 53, pp. 314–326, 1975.

[46] D. Maugis, "Adhesion of Spheres: The JKR-DMT Transition Using a Dugdale Model," *Journal of Colloid and Interface Science*, vol. 150, pp. 243–269, 1992.

[47] D. Tabor, "Surface Forces and Surface Interactions," *Journal of Colloid and Interface Science*, vol. 58, pp. 2–13, 1977.

[48] Y. L. Chen, C. A. Helm, and J. N. Israelachvili, "Molecular Mechanisms Associated with Adhesion and Contact Angle Hysteresis of Monolayer Surfaces," *Journal of Physcial Chemistry*, vol. 95, pp. 10736–10747, 1991.

[49] J. A. Greenwood, "Viscoelastic crack propagation and closing with Lennard-Jones surface forces," *Journal of Physics D: Applied Physics*, vol. 40, no. 6, pp. 1769–1777, 2007.

[50] J. A. Greenwood and K. L. Johnson, "The mechanics of adhesion of viscoelastic solids," *Philosophical Magazine A*, vol. 43, no. 3, pp. 697–711, 1981.

[51] K. R. Shull, “Contact Mechanics and the Adhesion of Soft Solids,” *Materials Science and Engineering R-Reports*, vol. 36, pp. 1–45, 2002.

[52] A. N. Gent, G. R. Hamed, and W. J. Hung, “Adhesion of elastomers: Dwell time effects,” *The Journal of Adhesion*, vol. 79, no. 4, pp. 315–325, Apr. 2003.

[53] C. S. Davis, F. Lemoine, T. Darnige, D. Martina, C. Creton, and A. Lindner, “Debonding mechanisms of soft materials at short contact times.,” *Langmuir : the ACS journal of surfaces and colloids*, vol. 30, no. 35, pp. 10626–36, Sep. 2014.

[54] E. Barthel and C. Frétigny, “Adhesive contact of elastomers: effective adhesion energy and creep function,” *Journal of Physics D: Applied Physics*, vol. 42, no. 19, p. 195302, Oct. 2009.

[55] J. A. Greenwood, “The theory of viscoelastic crack propagation and healing,” *Journal of Physics D: Applied Physics*, vol. 37, no. 18, pp. 2557–2569, Sep. 2004.

[56] M. K. Chaudhury, “Interfacial interaction between low-energy surfaces,” *Materials Science and Engineering R-Reports*, vol. 16, pp. 97–159, 1995.

[57] A. N. Gent and J. Schultz, “Effect of Wetting Liquids on the Strength of Adhesion of Viscoelastic Material,” *The Journal of Adhesion*, vol. 3, no. 4, pp. 281–294, Dec. 1972.

[58] W. C. Oliver and G. M. Pharr, “Measurement of hardness and elastic modulus by instrumented indentation: Advances in understanding and refinements to methodology,” *Journal of Materials Research*, vol. 19, no. 1, pp. 3–20, Jan. 2004.

[59] B. Cotterell, K. Hbaieb, J. G. Williams, H. Hadavinia, and V. Tropsa, “The root rotation in double cantilever beam and peel tests ,” *Mechanics of Materials* , vol. 38, pp. 571–584, 2006.

[60] P. A. Gustafson and A. M. Waas, “The influence of adhesive constitutive parameters in cohesive zone finite element models of adhesively bonded joints,” *International Journal of Solids and Structures*, vol. 46, no. 10, pp. 2201–2215, May 2009.

[61] R. Saha and W. D. Nix, “Effects of the substrate on the determination of thin film mechanical properties by nanoindentation,” *Acta Materialia*, vol. 50, no. 1, pp. 23–38, 2002.

[62] A. . Volinsky, N. . Moody, and W. . Gerberich, “Interfacial toughness measurements for thin films on substrates,” *Acta Materialia*, vol. 50, no. 3, pp. 441–466, Feb. 2002.

[63] W. Chen, X. Tang, J. Considine, and K. T. Turner, “Effect of Inorganic Fillers in Paper on the Adhesion of Pressure-Sensitive Adhesives,” *Journal of Adhesion Science and Technology*, vol. 25, no. 6–7, pp. 581–596, Jan. 2011.

[64] A. N. Gent and L. H. Lewandowski, “Blow-off pressures for adhering layers,” *Journal of Applied Polymer Science*, vol. 33, pp. 1567–1577, 1987.

[65] A. Sofla, E. Seker, J. P. Landers, and M. R. Begley, “PDMS-Glass Interface Adhesion Energy Determined Via Comprehensive Solutions for Thin Film Bulge/Blister Tests,” *Journal of Applied Mechanics*, vol. 77, no. 3, p. 31007, 2010.

[66] J. G. Williams, “Energy Release Rates for the Peeling of Flexible Membranes and the Analysis of Blister Tests,” *International Journal of Fracture*, vol. 87, pp. 265–288, 1997.

[67] M. E. R. Shanahan, “A Novel Test for the Appraisal of Solid/Solid Interfacial Interactions,” *Journal of Adhesion*, vol. 63, pp. 15–29, 1997.

[68] B. Cotterell and Z. Chen, “The blister test - Transition from plate to membrane behaviour for an elastic material,” *International Journal of Fracture*, vol. 86, pp. 191–198, 1997.

[69] H. M. Jensen, “The Blister Test for Interface Toughness Measurement,” *Engineering Fracture Mechanics*, vol. 40, pp. 475–486, 1991.

[70] H. M. Jensen, “Analysis of mode mixity in blister tests,” *International Journal of Fracture*, vol. 94, no. 1, pp. 79–88, Oct. 1998.

[71] Z. Cao *et al.*, “A blister test for interfacial adhesion of large-scale transferred graphene,” *Carbon*, vol. 69, pp. 390–400, Apr. 2014.

[72] K.-T. Wan and Y.-W. Mai, “Fracture mechanics of a new blister test with stable crack growth,” *Acta Metallurgica et Materialia*, vol. 43, no. 11, pp. 4109–4115, Nov. 1995.

[73] N. G. Boddeti, X. Liu, R. Long, J. Xiao, J. S. Bunch, and M. L. Dunn, “Graphene blisters with switchable shapes controlled by pressure and adhesion,” *Nano Letters*, vol. 13, no. 12, pp. 6216–6221, Jan. 2013.

[74] N. G. Boddeti, S. P. Koenig, R. Long, J. Xiao, J. S. Bunch, and M. L. Dunn, “Mechanics of Adhered, Pressurized Graphene Blisters,” *Journal of Applied Mechanics*, vol. 80, no. 4, p. 40909, Apr. 2013.

[75] S. A. White and R. H. Plaut, “The Effect of Work of Adhesion on Contact of a Pressurized Blister With a Flat Surface,” Virginia Polytechnic Institute and State University, 2001.

[76] T. Tsakalakos, “The Bulge Test: A Comparison of Theory and Experiment For Isotropic and Anisotropic Films,” *Thin Solid Films*, vol. 75, pp. 293–305, 1981.

[77] A. L. Thangawng, R. S. Ruoff, M. A. Swartz, and M. R. Glucksberg, "An ultra-thin PDMS membrane as a bio/micro–nano interface: fabrication and characterization," *Biomedical Microdevices*, vol. 9, no. 4, pp. 587–595, May 2007.

[78] K. R. Shull, D. Ahn, W.-L. Chen, C. M. Flanigan, and A. J. Crosby, "Axisymmetric adhesion tests of soft materials," *Macromolecular Chemistry and Physics*, vol. 199, no. 4, pp. 489–511, Apr. 1998.

[79] K. M. Liechti and Y. S. Chai, "Biaxial Loading Experiments for Determining Interfacial Fracture Toughness," *Journal of Applied Mechanics*, vol. 58, pp. 680–687, 1991.

[80] B. Han, D. Post, and P. Ifju, "Moire Interferometry For Engineering Mechanics: Current Practices and Future Developments," *Journal of Strain Analysis*, vol. 36, pp. 101–117, 2001.

[81] I. Kassamakov *et al.*, "Nondestructive Inspection of Buried Channels and Cavities in Silicon," *Journal of Microelectromechanical Systems*, vol. 22, no. 2, pp. 438–442, Apr. 2013.

[82] K. Hanhij *et al.*, "Through-Silicon Stroboscopic Characterization of an Oscillating MEMS Thermal Actuator Using Supercontinuum Interferometry," *IEEE/ASME Transactions on Mechatronics*, vol. 18, no. 4, pp. 1418–1420, Aug. 2013.

[83] S. Gowrishankar, H. Mei, K. M. Liechti, and R. Huang, "A comparison of direct and iterative methods for determining traction-separation relations," *International Journal of Fracture*, vol. 177, no. 2, pp. 109–128, Aug. 2012.

[84] B. Pan, "Reliability-guided digital image correlation for image deformation measurement.," *Applied optics*, vol. 48, no. 8, pp. 1535–1542, Mar. 2009.

[85] C. Sun, Y. Zhou, J. Chen, and H. Miao, "Measurement of Deformation Close to Contact Interface Using Digital Image Correlation and Image Segmentation," *Experimental Mechanics*, vol. 55, no. 8, pp. 1525–1536, Oct. 2015.

[86] B. Pan, Z. Wang, and Z. Lu, "Genuine full-field deformation measurement of an object with complex shape using reliability-guided digital image correlation.," *Optics express*, vol. 18, no. 2, pp. 1011–1023, Jan. 2010.

[87] C. Liu, J. D. Yeager, and K. J. Ramos, "Bonding energy of Sylgard on fused quartz: an experimental investigation," *Philosophical Magazine*, vol. 95, no. 4, pp. 346–366, Feb. 2015.

[88] M. A. Sutton, J. H. Yan, V. Tiwari, H. W. Schreier, and J. J. Orteu, "The effect of out-of-plane motion on 2D and 3D digital image correlation measurements," *Optics*

and Lasers in Engineering, vol. 46, no. 10, pp. 746–757, 2008.

[89] S. Xia, A. Gdoutou, and G. Ravichandran, "Diffraction Assisted Image Correlation: A Novel Method for Measuring Three-Dimensional Deformation using Two-Dimensional Digital Image Correlation," *Experimental Mechanics*, vol. 53, no. 5, pp. 755–765, Oct. 2012.

[90] Z. Pan, S. Xia, A. Gdoutou, and G. Ravichandran, "Diffraction-Assisted Image Correlation for Three-Dimensional Surface Profiling," *Experimental Mechanics*, vol. 55, no. 1, pp. 155–165, Aug. 2014.

[91] B. Pan and Q. Wang, "Single-camera microscopic stereo digital image correlation using a diffraction grating," *Optics Express*, vol. 21, no. 21, p. 25056, Oct. 2013.

[92] L. Wu, J. Zhu, and H. Xie, "Single-lens 3D digital image correlation system based on a bilateral telecentric lens and a bi-prism: validation and application.," *Applied optics*, vol. 54, no. 26, pp. 7842–50, Sep. 2015.

[93] "MATLAB." The MathWorks Inc., Natick, Massachusetts, 2016.

[94] S. Timoshenko and S. Woinowsky-Krieger, *Theory of plates and shells*. McGraw-Hill, 1959.

[95] M. Sheplak and J. Dugundji, "Large Deflections of Clamped Circular Plates Under Initial Tension and Transitions to Membrane Behavior," *Journal of Applied Mechanics*, vol. 65, no. 1, p. 107, Mar. 1998.

[96] S. Guo, K.-T. Wan, and D. a. Dillard, "A bending-to-stretching analysis of the blister test in the presence of tensile residual stress," *International Journal of Solids and Structures*, vol. 42, no. 9, pp. 2771–2784, May 2005.

[97] M. Salehi and H. Aghaei, "Dynamic relaxation large deflection analysis of non-axisymmetric circular viscoelastic plates," *Computers & Structures*, vol. 83, no. 23–24, pp. 1878–1890, Sep. 2005.

[98] A. Kelkar, W. Elber, and I. S. Raju, "Large Deflections of Circular Isotropic Membranes Subjected to Arbitrary Axisymmetric Loading," *Computers and Structures*, vol. 21, pp. 413–421, 1985.

[99] "ABAQUS." Dassault Systèmes, Providence, RI, 2013.

[100] J. N. Reddy and C. M. Wang, "Relationships Between Classical and Shear Deformation Theories of Axisymmetric Circular Plates," *AIAA Journal*, vol. 35, no. 12, pp. 1862–1868, Dec. 1997.

[101] C. Majidi and G. G. Adams, "Adhesion and delamination boundary conditions for

elastic plates with arbitrary contact shape," *Mechanics Research Communications*, vol. 37, no. 2, pp. 214–218, Mar. 2010.

[102] R. Krueger, "Virtual crack closure technique: History, approach, and applications," *Applied Mechanics Reviews*, vol. 57, no. 2, p. 109, 2004.

[103] Y.-H. Lai and D. A. Dillard, "An Elementary Plate Theory Prediction for Strain Energy Release Rate of the Constrained Blister Test," *Journal of Adhesion*, vol. 31, pp. 177–189, 1990.

[104] Y.-H. Lai and D. A. Dillard, "Numerical Analysis of the Constrained Blister Test," *Journal of Adhesion*, vol. 33, pp. 63–74, 1990.

[105] H. M. Jensen and B. Cochelin, "Fracture Analysis of the Constrained Blister Test," *Journal of Adhesion*, vol. 47, pp. 231–243, 1994.

[106] M. R. Begley and T. J. Mackin, "Spherical indentation of freestanding circular thin films in the membrane regime," *Journal of the Mechanics and Physics of Solids*, vol. 52, no. 9, pp. 2005–2023, 2004.

[107] W. N. Sharpe Jr., Ed., *Springer Handbook of Experimental Solid Mechanics*, 2008th ed. Springer, 2008.

[108] B. Pan, K. Qian, H. Xie, and A. Asundi, "Two-Dimensional Digital Image Correlation for In-plane Displacement and Strain Measurement: A Review," *Measurement Science and Technology*, vol. 20, pp. 1–17, 2009.

[109] C. Eberl, R. Thompson, D. Gianola, and S. Bundschuh, "Digital image correlation and tracking with Matlab." 2010.

[110] E. Navarro *et al.*, "Direct silicon bonding dynamics: A coupled fluid/structure analysis," *Applied Physics Letters*, vol. 103, no. 3, p. 34104, Jul. 2013.

[111] B. N. J. Persson, O. Albohr, U. Tartaglino, a I. Volokitin, and E. Tosatti, "On the nature of surface roughness with application to contact mechanics, sealing, rubber friction and adhesion.," *Journal of Physics: Condensed Matter*, vol. 17, no. 1, pp. R1–R62, Jan. 2005.

[112] J. Nase, O. Ramos, C. Creton, and A. Lindner, "Debonding energy of PDMS," *The European Physical Journal E*, vol. 36, no. 9, p. 103, Sep. 2013.

[113] E. Kroner, R. Maboudian, and E. Arzt, "Adhesion Characteristics of PDMS Surfaces During Repeated Pull-Off Force Measurements," *Advanced Engineering Materials*, vol. 12, no. 5, pp. 398–404, May 2010.

[114] S. CHEN and H. GAO, "Non-slipping adhesive contact between mismatched elastic

spheres: A model of adhesion mediated deformation sensor," *Journal of the Mechanics and Physics of Solids*, vol. 54, no. 8, pp. 1548–1567, Aug. 2006.

[115] J. F. Waters, J. Kalow, H. Gao, and P. R. Guduru, "Axisymmetric Adhesive Contact Under Equibiaxial Stretching," *Journal of Adhesion*, vol. 88, pp. 134–144, 2012.

[116] J. H. Ryoo, G. S. Jeong, E. Kang, and S. H. Lee, "Ultrathin, hyperelastic PDMS nano membrane," Dec. 2011.

[117] Y. Yu, D. Sanchez, and N. Lu, "Work of adhesion/separation between soft elastomers of different mixing ratios," *Journal of Materials Research*, vol. 30, no. 18, pp. 1–11, Sep. 2015.

[118] G. Jekabsons, "ARESLab: Adaptive Regression Splines toolbox for Matlab/Octave." 2015.

[119] I. D. Johnston, D. K. McCluskey, C. K. L. Tan, and M. C. Tracey, "Mechanical characterization of bulk Sylgard 184 for microfluidics and microengineering," *Journal of Micromechanics and Microengineering*, vol. 24, no. 3, p. 35017, Mar. 2014.

[120] D. Martina, C. Creton, P. Damman, M. Jeusette, and A. Lindner, "Adhesion of soft viscoelastic adhesives on periodic rough surfaces," *Soft Matter*, vol. 8, no. 19, p. 5350, 2012.

[121] A. Srivastava and C.-Y. Hui, "Large deformation contact mechanics of a pressurized long rectangular membrane. II. Adhesive contact.," *Proceedings. Mathematical, physical, and engineering sciences / the Royal Society*, vol. 469, no. 2160, p. 20130425, Dec. 2013.

[122] A. Srivastava and C.-Y. Hui, "Large deformation contact mechanics of long rectangular membranes. I. Adhesionless contact.," *Proceedings. Mathematical, physical, and engineering sciences / the Royal Society*, vol. 469, no. 2160, p. 20130424, Dec. 2013.

[123] E. J. Laprade *et al.*, "Large Deformation and Adhesive Contact Studies of Axisymmetric Membranes," *Langmuir*, vol. 29, pp. 1407–1419, 2013.

[124] C. J. Van Oss, R. J. Good, and M. K. Chaudhury, "Additive and nonadditive surface tension components and the interpretation of contact angles," *Langmuir*, vol. 4, no. 4, pp. 884–891, Jul. 1988.

[125] A. Kowalski, Z. Czech, and Ł. Byczyński, "How does the surface free energy influence the tack of acrylic pressure-sensitive adhesives (PSAs)?," *Journal of Coatings Technology and Research*, vol. 10, no. 6, pp. 879–885, Aug. 2013.

[126] B. N. J. Persson and E. Tosatti, “The effect of surface roughness on the adhesion of elastic solids,” *The Journal of Chemical Physics*, vol. 115, no. 12, p. 5597, 2001.

[127] J. Canny, “A Computational Approach to Edge Detection,” *IEEE Transactions on Pattern Analysis and Machine Intelligence*, vol. PAMI-8, no. 6, pp. 679–698, Nov. 1986.

[128] J. Dealy and D. Plazek, “Time-temperature superposition - a users guide,” *Rheology Bulletin*, vol. 78, no. 2, pp. 16–31, 2009.

[129] B. Mukherjee, D. A. Dillard, R. B. Moore, and R. C. Batra, “Debonding of confined elastomeric layer using cohesive zone model,” *International Journal of Adhesion and Adhesives*, vol. 66, pp. 114–127, Apr. 2016.

[130] A. Ghatak and M. K. Chaudhury, “Adhesion-Induced Instability Patterns in Thin Confined Elastic Film,” *Langmuir*, vol. 19, no. 7, pp. 2621–2631, Apr. 2003.

[131] A. Falsafi, M. Tirrell, and A. V Pocius, “Compositional Effects on the Adhesion of Acrylic Pressure Sensitive Adhesives,” *Langmuir*, vol. 16, pp. 1816–1824, 2000.

[132] C. Creton, J. Hooker, and K. R. Shull, “Bulk and Interfacial Contributions to the Debonding Mechanisms of Soft Adhesives: Extension to Large Strains,” *Langmuir*, vol. 17, no. 16, pp. 4948–4954, Aug. 2001.

[133] R. N. Palchesko, L. Zhang, Y. Sun, and A. W. Feinberg, “Development of Polydimethylsiloxane Substrates with Tunable Elastic Modulus to Study Cell Mechanobiology in Muscle and Nerve,” *PLoS ONE*, vol. 7, no. 12, p. e51499, Dec. 2012.

[134] C. Majidi, R. Kramer, and R. J. Wood, “A non-differential elastomer curvature sensor for softer-than-skin electronics,” *Smart Materials and Structures*, vol. 20, no. 10, p. 105017, Oct. 2011.

[135] R. D. Mindlin, “Influence of rotatory inertia and shear on flexural motions of isotropic elastic plates,” *Journal of Applied Mechanics*, vol. 18, pp. 31–38, 1951.